FERROMAGNETICALLY TAGGED MICRO-PARTICLE DETECTION: SIMULATION AND ESTIMATION

by

Kevin Giroux
B.A.Sc., Simon Fraser University 2008

THESIS SUBMITTED IN PARTIAL FULFILLMENT OF
THE REQUIREMENTS FOR THE DEGREE OF

MASTER OF APPLIED SCIENCE

In the
School of Engineering Science

SIMON FRASER UNIVERSITY

Fall 2010

APPROVAL

Name:	**Kevin Giroux**
Degree:	**Master of Applied Science**
Title of Thesis:	**Ferromagnetically tagged micro-particle detection: Simulation and estimation**

Examining Committee:

Chair: **Michael Sjoerdsma, Lecturer**
School of Engineering Science

Dr. Ash M. Parameswaran, P. Eng.
Senior Supervisor
Professor, School of Engineering Science

Dr. Marek J. Syrzycki
Supervisor
Professor, School of Engineering Science

Dr. Carlo Menon, P. Eng.
Internal Examiner
Assistant Professor, School of Engineering Science

Date Defended/Approved: December 15, 2010

SFU SIMON FRASER UNIVERSITY
LIBRARY

Declaration of Partial Copyright Licence

The author, whose copyright is declared on the title page of this work, has granted to Simon Fraser University the right to lend this thesis, project or extended essay to users of the Simon Fraser University Library, and to make partial or single copies only for such users or in response to a request from the library of any other university, or other educational institution, on its own behalf or for one of its users.

The author has further granted permission to Simon Fraser University to keep or make a digital copy for use in its circulating collection (currently available to the public at the "Institutional Repository" link of the SFU Library website <www.lib.sfu.ca> at: <http://ir.lib.sfu.ca/handle/1892/112>) and, without changing the content, to translate the thesis/project or extended essays, if technically possible, to any medium or format for the purpose of preservation of the digital work.

The author has further agreed that permission for multiple copying of this work for scholarly purposes may be granted by either the author or the Dean of Graduate Studies.

It is understood that copying or publication of this work for financial gain shall not be allowed without the author's written permission.

Permission for public performance, or limited permission for private scholarly use, of any multimedia materials forming part of this work, may have been granted by the author. This information may be found on the separately catalogued multimedia material and in the signed Partial Copyright Licence.

While licensing SFU to permit the above uses, the author retains copyright in the thesis, project or extended essays, including the right to change the work for subsequent purposes, including editing and publishing the work in whole or in part, and licensing other parties, as the author may desire.

The original Partial Copyright Licence attesting to these terms, and signed by this author, may be found in the original bound copy of this work, retained in the Simon Fraser University Archive.

Simon Fraser University Library
Burnaby, BC, Canada

Last revision: Spring 09

ABSTRACT

This thesis examines the possibility of using an inductance-based method of detecting ferromagnetically tagged bio-molecules. A proof-of-concept experiment was conducted using a coil wrapped around a glass capillary in conjunction with a simple oscillator circuit. Simulations were conducted comparing the inductance value of various coil designs and how they change when an iron sphere was introduced inside the coil. A suitable coil design was determined, and a fabrication process is developed to build a micro-scale coil with a microfluidic channel running through it. This thesis explores the design optimization using computer simulations along with a set of preliminary feasibility results. With the optimum coil design, the simulation results indicate that a ferromagnetic sphere with a radius of 0.5 μm could be detected.

Keywords: Inductance; Bio-molecule detection; Coil; Micro channel; SU-8; Simulation

DEDICATION

I would like to dedicate this thesis to my wife-to-be, Rebecca. I couldn't have done it without all her love and support.

ACKNOWLEDGEMENTS

I would like to thank my senior supervisor, Dr. Ash M. Parameswaran for his guidance and direction throughout my studies, and in particular, on this thesis. I would also like to thank my supervisor Dr. Marek J. Syrzycki for all of his support and feedback. I also thank Dr. Carlo Menon for graciously accepting to be the examiner for my thesis defence. Thank you to Mike Sjoerdsma for his valuable feedback on my thesis, and for accepting the role of chair for my defence. I would also like to acknowledge the contribution made by Sae Won Lee, who was instrumental in designing the fabrication process and showing me how to do all of the steps involved. I thank everyone in the lab for their ideas, feedback, and support over the years, and last but not lease, my family for all of their support and encouragement.

TABLE OF CONTENTS

LIST OF FIGURES

LIST OF TABLES

1: INTRODUCTION

Detecting the presence of pathogens is a key factor in diagnosing and treating many communicable diseases. If a person gets sick in a remote location, correctly diagnosing their illness so that the proper treatment can be given could be a lengthy process of sending a sample off to a lab and waiting for a result. Fluorescent techniques [1] are the current preferred method of bio-molecule detection due to their effectiveness, but they require large, expensive optical equipment that does not lend itself to portability. Our goal is to develop a device that can overcome these problems of cost and logistics by providing a solution that is inexpensive, portable, and can be used without requiring the expertise of a trained specialist. A direct electrical detection technique could fill the need for a more economical and portable method of bio-molecule detection.

There are biochemical techniques available that allow bio-molecules to be tagged with ferromagnetic nano-particles [2]. By linking the bio-molecule to a ferromagnetic nano-particle, we can focus on the detection of the ferromagnetic particle electrically to indicate the presence or absence of the target bio-molecule. A classical approach to detecting ferromagnetic particles is a frequency-based method of detection. This method is entirely within the electrical domain, and can be used to build a small, portable detection device. To use a frequency-based detection method, we need an oscillator that will change frequency when a ferromagnetic particle is introduced. In such an oscillator, the most important component is the coil, as it will change inductance when ferromagnetic material is introduced inside of it, and will thus cause the frequency of the oscillator to change. The ferromagnetically tagged particles will be carried in a fluid, and passed through the coil via a channel. We need to optimize the coil dimensions to make it sensitive to the smallest tagged ferromagnetic particle. We want to be able to detect on the order of 10^3 particles with a diameter of 15 nm, as this number is what the fluorescent techniques are capable of. Therefore, we used the simulation technique to find the most suitable coil design.

In our earlier work, we explored the possibility of this technique using a pulse resonance method [3], consisting of a pair of coils wound around a chamber that served as the sensor. A pulse was sent to one coil and the second coil picked up a resonant waveform. By measuring the frequency of the resonance, it could be determined whether iron was in the test chamber. Although this idea worked in concept, it was not nearly sensitive enough to be used to detect a reasonable number of nano particles, requiring in the order of 10^{14} particles to signal detection [3]. The biggest limiting factor seemed to be the coil dimensions. The coil volume of 50.3 mm^3 was simply too large compared to the 1.77×10^3 nm^3 volume of the nano-particles.

In order to build a device that could detect such small particles, a much smaller coil was necessary. The two coil system was also re-examined, and we decided that a simpler single coil method would be more appropriate. A new coil was built by winding copper wire around a 1.2 mm glass capillary. This coil was smaller than the 3 mm diameter coil used in the previous device. The circuit used was also much simpler, consisting of just an oscillator and no frequency detection component. Instead, an oscilloscope was used to track the frequency. Chapter 2 describes this device in more detail.

After seeing some promising results from the reduction in coil size, we decided that even smaller coil designs needed to be examined. We used the simulation method to examine the effectiveness of many different coil designs. The results of the simulations of varying coil dimensions are outlined in Chapter 3. The software physics simulator Comsol was used to find the inductance of the various coil designs, and then an iron particle was placed inside of the coil to determine the minimum size iron particle that the particular coil could detect.

We used the results of the simulation to examine the possibility of building one of these coils. Because we could not use the technique of winding a wire around a tube to make a micro-coil, some modifications to the coil design were required. A cylindrical coil, like the ones used before would not be possible. After designing a coil that could be fabricated, more simulations were computed on the new design. The simulation results indicated that this new design could detect iron particles with a 2 μm radius, so we came up with a method to fabricate a coil on the micro scale. In Chapter 4, the design, simulation, and potential fabrication technique of this new coil are detailed.

2: PROOF-OF-CONCEPT EXPERIMENT

In earlier work, we built a device to detect iron particles that used a pulse resonance based method [3]. This system used a pair of coils, where one received a square wave signal, and the other produced a resonant response. However, after examining the results of this device, we determined that we could use a simpler, single coil design that could potentially offer better detection capabilities.

2.1 Experimental setup

For this experiment, we built an oscillator circuit that required an inductor. For the inductor, we wound a wire around a glass capillary. We were then able to monitor the frequency of oscillation while passing fluids containing iron particles through the tube.

2.1.1 Oscillator Design

When selecting the oscillator design to use, we wanted to pick one that used only a single inductor, as that would allow us to build a single component as our sensor, and use off-the-shelf components for the rest of the circuit. Out of the two basic LC oscillator types, this desire for a single-inductor oscillator led us to choose the Colpits oscillator over the Hartley [4]. The following figure shows the schematic for the oscillator circuit we built, along with an inverter and pull-up resistor at the output.

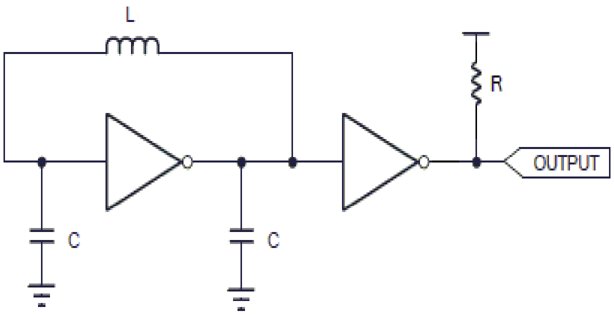

Figure 1: Schematic of Colpits oscillator

The centre frequency for the oscillator is given by [4]

$$f = \frac{1}{2\pi\sqrt{LC_{tot}}}, \tag{1}$$

where C_{tot} is the total capacitance of the oscillator circuit and L is the effective inductance of the coil.

When taking into account the input capacitance of the inverter and the capacitive component of the inductor, C_{tot} becomes $C/2 + C_{Inv} + C_L$, and we derive the following formula for the frequency:

$$f = \frac{1}{2\pi\sqrt{L\left(C_L + C_{Inv} + {}^{C}\!/_{2}\right)}}, \tag{2}$$

where C_{Inv} is the inverter capacitance, which is found in [5] and C_L is the inductor capacitance, which we assume is zero when the coil is empty.

The inductance of a circular loop of wire can be estimated as [6].

$$L_{Circle} \approx N^2 R \mu_0 \mu_r \left[\ln\left(\frac{8R}{a} \right) - 2 \right], \tag{3}$$

where N is the number of turns, R is the radius of the coil, μ_0 is the permeability of free space, μ_r is the relative permeability, and a is the radius of the wire. For our inductor, we wound 20 turns of AWG 40 copper wire around a 1.2 mm diameter glass capillary. Using Equation 3, we calculated the inductance of this coil to be 0.632 μH.

For our capacitors, we selected 10 pF. By substituting this value into Equation 1, along with the calculated inductance value, we calculated a frequency of 91.8 MHz. For the inverter, we chose a 74HCU04, which has a capacitance of 7 pF [5]. Using Equation 2 along with these values, we calculated a frequency of 57.8 MHz.

2.1.2 Samples

To test our device, we needed to suspend iron particles in a fluid and pass it through the capillary. We used iron nano-particles that ranged in size from 35 nm to 50 nm. For the fluid, we selected acetone because it has a lower dielectric constant than water (20.7 vs. 80.0 [7]), and we noticed a frequency shift in our oscillator when a fluid containing no iron passed through the tube. This frequency change is due to the fluid acting as a dielectric and changing the capacitance of the coil. Acetone had a lower impact on the oscillator frequency than water did. With pure acetone in the tube, we observed a frequency shift of

58 kHz, and, using Equation 2, we estimated that the acetone inside the coil acts like adding a 0.024 pF capacitor in parallel with the inductor.

We prepared the samples by weight percentage. The concentrations we used for this experiment, by estimated weight percentage, were 0% (pure acetone), 0.0001%, 0.0010%, 0.1500%, and 0.3000%.

2.1.3 Procedure

We powered the circuit, and observed the frequency shift for the introduced sample. We aligned the capillary vertically and inserted samples using a syringe pump.

We recorded the frequency output of the circuit, starting 15 seconds before the sample was introduced, and continuing until the sample had completely passed through the coil. After each sample, we thoroughly cleansed the capillary, so as not to contaminate subsequent tests.

We mixed the sample with an ultrasonic probe in an effort to keep the suspension as uniform as possible. We then loaded the sample into a syringe pump, and shook it continuously until inserting it into the capillary and pushing the suspension through. However, we still observed a significant quantity of particles dropping out of suspension, which made it impossible to know the exact concentration that we were measuring.

2.2 Hspice Simulation

We simulated the circuit from Figure 1 using Hspice, and we found the frequency to be 54.2 MHz. This simulated value is 6% smaller than the theoretical value calculated in Section 2.1.1 of 57.8 MHz. Table 1 shows the theoretical and simulated predictions for the oscillator frequency when the inductance and capacitance of the coil are changed. In the first row, we see the initial state, followed by the estimated change in capacitance due to the acetone. In the last row, we see the estimated changes in capacitance and inductance due to the 0.0001% sample.

Table 1: Frequency results for capacitance and inductance changes

C_L (pF)	L(µH)	Theoretical		Simulated	
		Frequency (MHz)	Frequency drop (kHz)	Frequency (MHz)	Frequency drop (kHz)
0.0000	0.6320	57.792	-	54.236	-
0.0240	0.6320	57.735	57.000	53.912	324.00
0.0240	0.6325	57.712	80.000	54.012	224.00

We see a significant discrepancy between the theoretical results and the simulated results for the frequency drop. This disagreement suggests that we need to make refinements to our simulation model, which will be considered in future work.

2.3 Results

In the following five figures, we show the results of the frequency change for each sample as it passed through the coil. The solid line represents the raw data collected from the oscilloscope, while the dashed line represents the average value, calculated separately for when the coil is empty and when the sample is passing through it. The second drop, seen in Figure 2, is due to pushing a second batch of acetone through during the same run, which we were able to do since we did not have to worry about the tube being contaminated with iron.

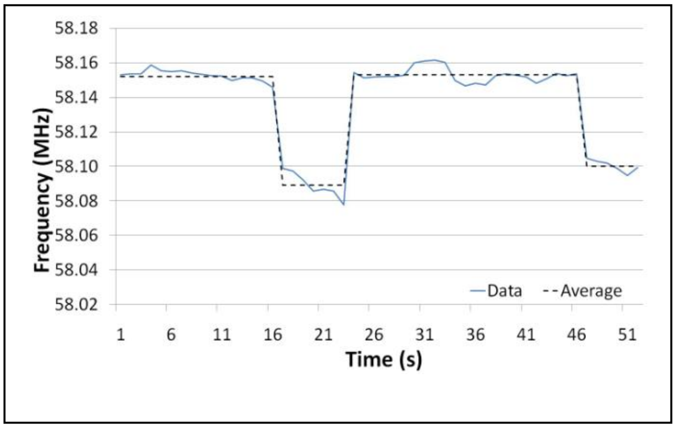

Figure 2: Frequency vs Time for pure acetone

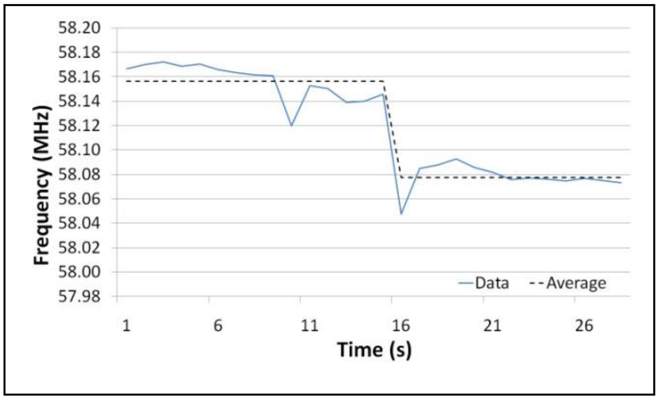

Figure 3: Frequency vs Time for 0.0001% sample

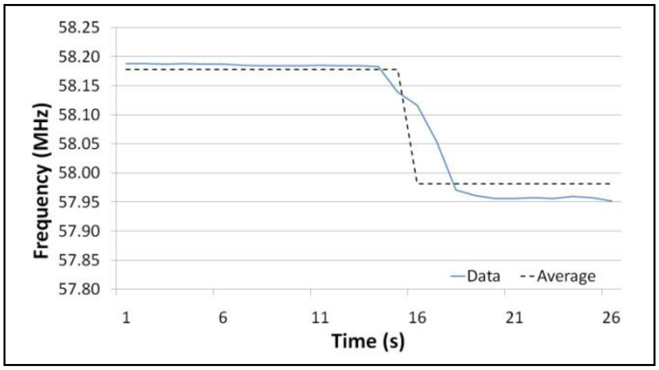

Figure 4: Frequency vs Time for 0.0010% sample

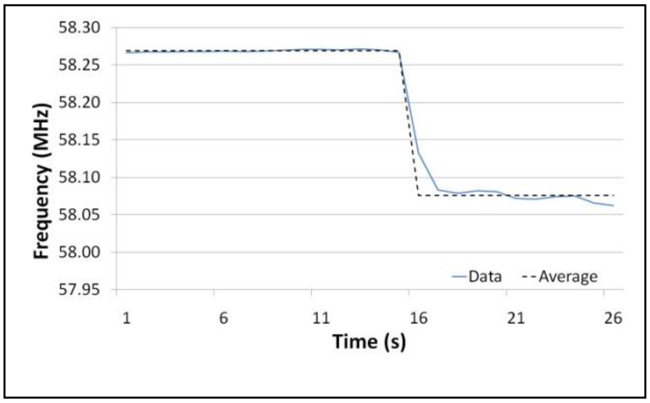

Figure 5: Frequency vs Time for 0.1500% sample

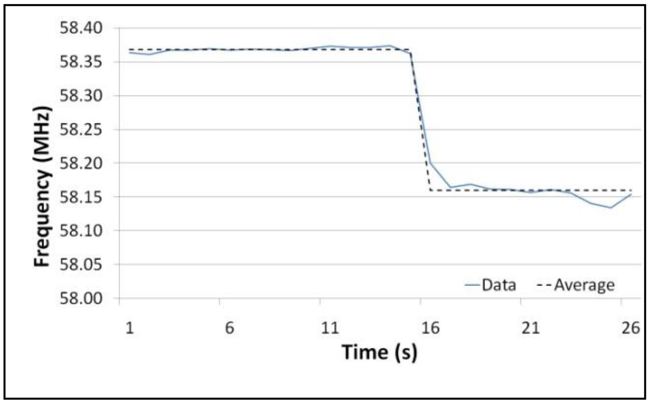

Figure 6: Frequency vs Time for 0.3000% sample

The Figure 7 shows a summary of the frequency change for each sample. Once the concentration reaches 0.0010%, the iron concentration through the coil has saturated and no further significant frequency change can be observed. This saturation occurs because the iron particles clogged the end of the syringe, and higher concentrations could not be pushed into the coil. This problem is a limit of our experimental setup, and future experiments will need to keep this scenario in mind, although the focus will be on detecting smaller concentrations, as opposed to larger ones.

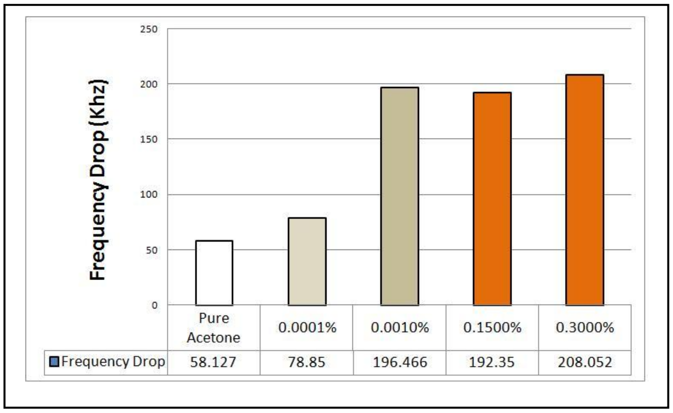

	Pure Acetone	0.0001%	0.0010%	0.1500%	0.3000%
■ Frequency Drop	58.127	78.85	196.466	192.35	208.052

Figure 7: Frequency drop for each sample

3: SIMULATIONS AND RESULTS

In the pursuit of a ferromagnetic bio-molecule detection scheme, it is necessary to find a coil design that has the optimal sensitivity to iron nano particles. This chapter details the design of different coils and simulation results for how their inductance changes when a small quantity of iron was placed inside the coil. We designed the coils in SolidWorks, and then Comsol was used to simulate their electromagnetic properties and determine their inductance. At first, coils are examined with different sized iron particles placed in the centre. Later on in this chapter, coils are investigated in more detail, with the iron particles being moved through various positions inside the coils.

The goal was to come up with an ideal coil design that can later be used in an LC oscillator circuit as part of a bio-molecule detection scheme.

3.1 Methodology

SolidWorks was used to design three dimensional coils with varying properties. The simulations could have been simplified by using a two dimensional axial symmetry approach, but, because the coil is the key component in the ferromagnetic particle detection scheme, three dimensional analysis was used to keep the simulation as close to the real physical system as possible.

Once the 3D models were created in SolidWorks, they were imported into Comsol and then the “quasi-statics of electromagnetic systems for conducting, magnetic, and dielectric materials” option of the AC/DC Module was used for analysis. A box was constructed around the coil such that the only parts of the coil exposed to the outside of the box were the two ends. One end of the coil was configured as an input port and the other end was set to ground. The rest of the coil and the surrounding box were set to magnetic and electrical insulation. The coil was loaded with the copper material properties.

We started out by simulating a coil with similar dimensions to the one used in Chapter 2, and then smaller and smaller ones were looked at. At first, the wires were modelled as round, but this increased the complexity of the model, and the importation of the model from SolidWorks into Comsol would not complete. Instead, wires with a square cross-sectional area were used to form the coils. The properties of the first set of coils simulated are summarized in the Table 2.

The inductance value was obtained using the following formula,

$$L = \frac{\mathrm{Im}(z)}{\omega}, \tag{4}$$

where *Im(Z)* is the imaginary part of the impedence, and ω is the angular frequency.

Table 2: Coil Properties

Coil	Diameter (mm)	Length (mm)	Turns	Wire cross-sectional area (μm^2)	Inductance (nH)
1	1.00	1.00	5	400	13.12717
2	1.00	1.00	10	400	39.71393
3	1.00	1.00	15	400	82.20001
4	1.00	0.50	10	400	57.45802
5	1.00	0.25	10	400	67.74763
6	0.20	0.25	10	25	5.379566
7	0.10	0.25	10	25	2.938481
8	0.10	0.10	10	25	4.384126
9	0.10	0.10	5	25	1.297896
10	0.10	0.05	5	25	2.302124

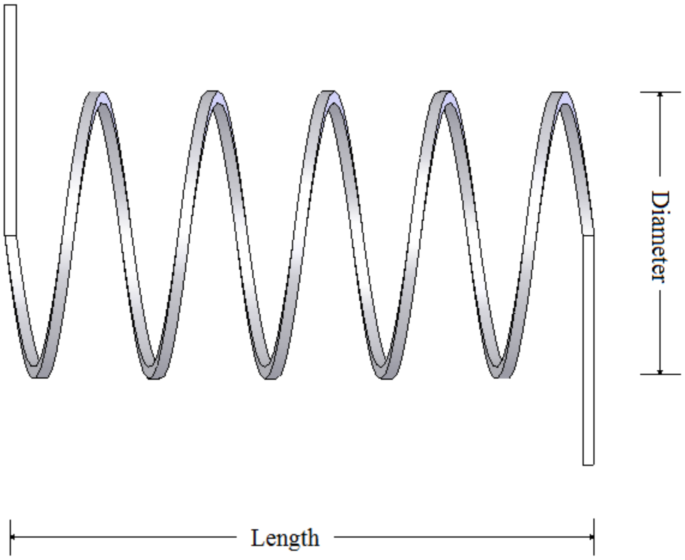

Figure 8: Length and diameter measurements of a coil

Figure 8 shows where the length and diameter are measured for a typical coil.

3.2 Simulations

The first set of simulations shows how the inductance of some of the coils changes with frequency, and the second compares how the inductance of each coil changes when iron spheres of different sizes are placed in the centre of the coil. We then compute some more detailed simulations examining how the inductance of the coils are effected by placing iron spheres in different positions inside of the coils.

3.2.1 Frequency response

The frequency response of each of the first three coils are shown in Figures 9 through 11.

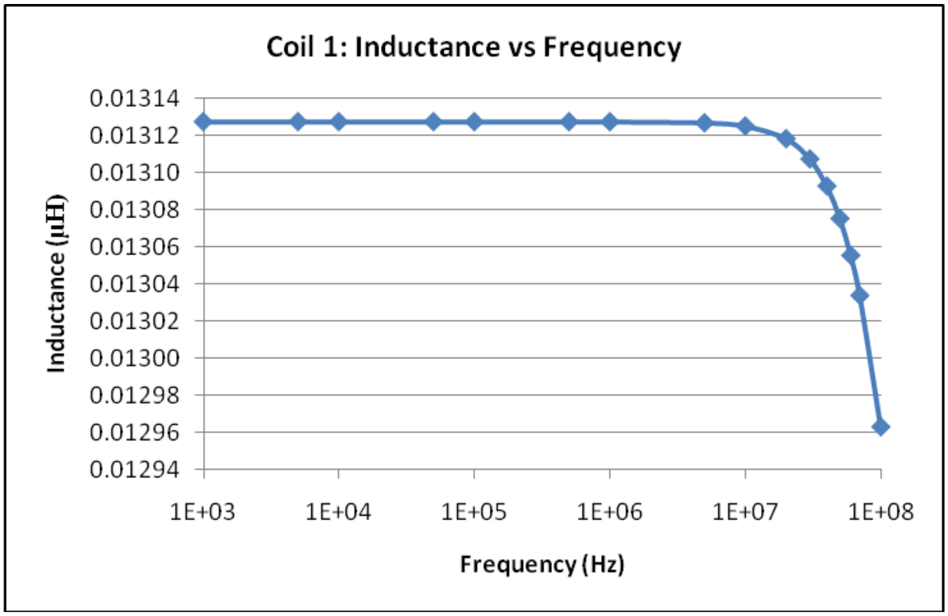

Figure 9: Coil 1 frequency response

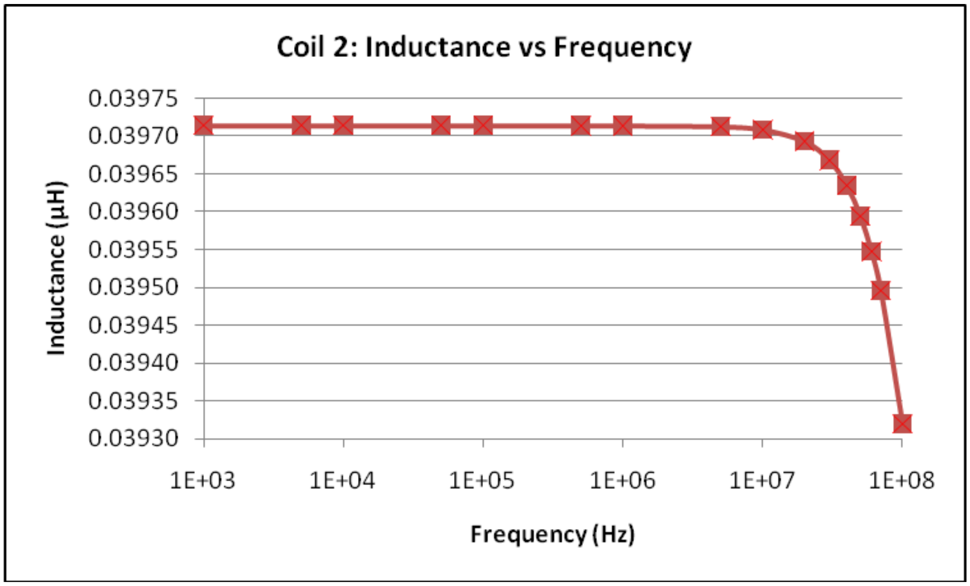

Figure 10: Coil 2 frequency response

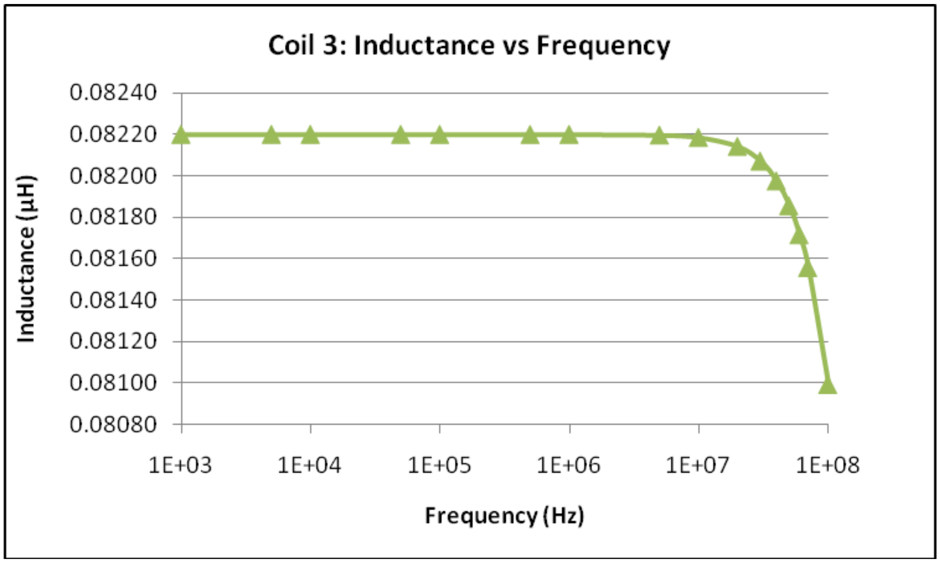

Figure 11: Coil 3 frequency response

From the above figures, all three of the coils behave in the same manor, with the inductance dropping off as the frequency exceeds 10 MHz. Due to the similarities between the first three coils, we omitted coils 4 through 9 and looked at the frequency response for Coil 10.

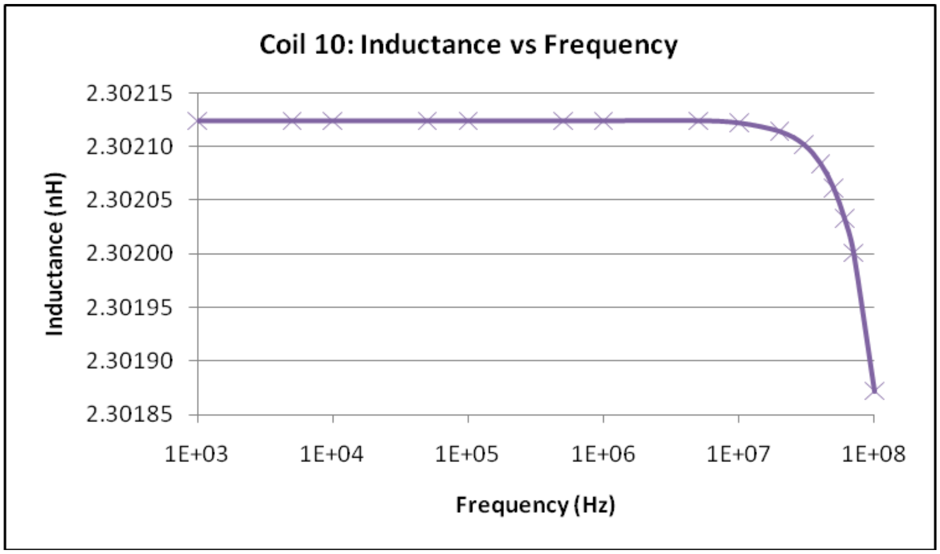

Figure 12: Coil 10 frequency response

Even a coil with vastly different properties from the first three still shows the same trend as the frequency increases. However, while the trend is the same, the inductance values are in nH for Coil 10, as opposed to μH for Coils 1-3, and the percentage change in the inductance is much less for Coil 10. The following graph shows the percentage change in inductance for each of the four tested coils.

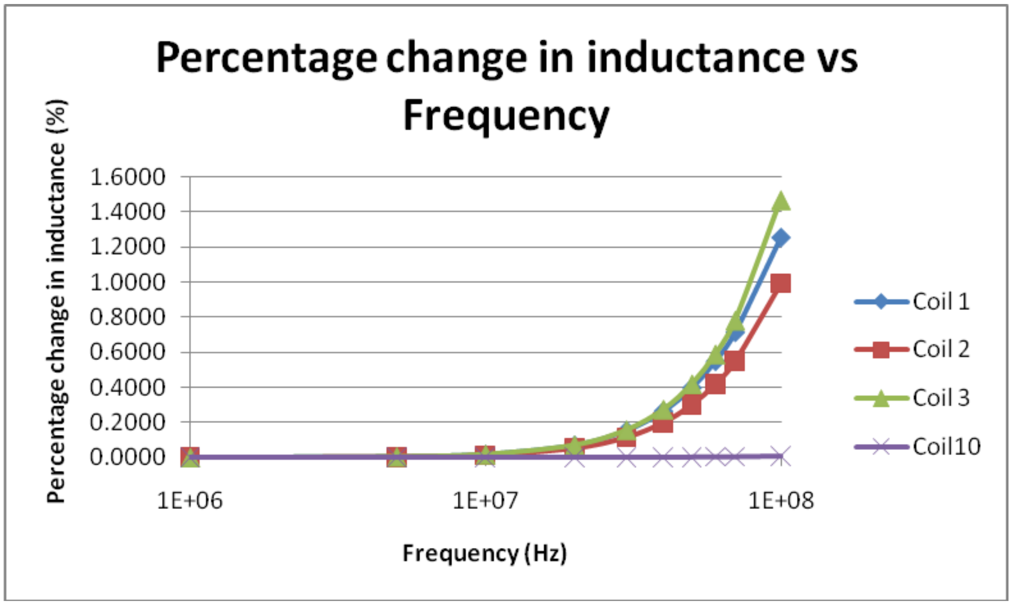

Figure 13: Inductance change comparison of coils 1, 2, 3, and 10

When compared to the larger coils, the inductance for Coil 10 barely changes at all with increasing frequency. In light of these results, a frequency of 1 kHz was used for the remainder of the experiment, as it reduced the simulation time compared to the higher frequencies.

3.2.2 Single point detection limit

To find the detection limit for each coil, a sphere was added inside the centre of the coil. The sphere's material properties were set to iron and then the inductance was measured for spheres of different radii. If the inductance was greater than the inductance for when the coil was empty, the sphere was considered detectable.

3.2.2.1 Coil 1

Coil 1 was similar in diameter to the one used in Chapter 2, with a diameter of 1.0 mm, although it had only 5 turns. We started with an iron sphere radius of 200 μm, and then reduced the sphere radius to 100 μm.

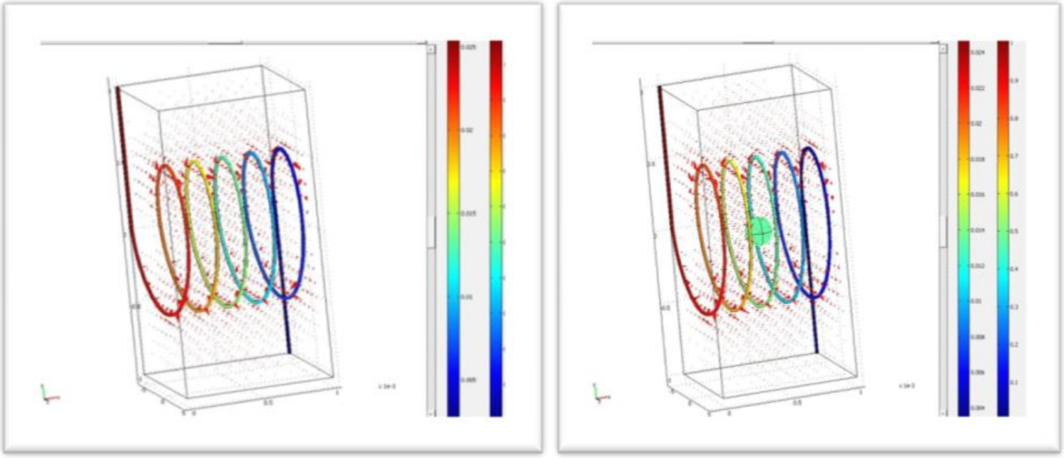

Figure 14: Magnetic flux density and electric potential for Coil 1 empty (left) and with iron (right)[1]

Table 3 shows the inductance of Coil 1 for the two spheres that were simulated. These inductance values were then compared with the inductance

---

[1] Full size versions of these figures are available in Appendix C.

value in Table 2 for Coil 1. If it was greater, as with the 200 μm radius sphere, we placed a ‘Y’ in the Detectable column. If it was smaller, we entered an ‘N’.

Table 3: Coil 1 iron sphere detection

Radius (μm)	Inductance (nH)	Detectable (Y/N)
200	13.41162	Y
100	13.05768	N

The first coil design exhibited poor results, as it was unable to detect a sphere with a radius of 100 μm. A new design was considered without running any further simulations on Coil 1.

3.2.2.2 Coil 2

Coil 2 maintained the same properties as Coil 1, except increased the number of turns to 10. We first attempted the 100 μm radius sphere again, and discovered that it was detectable. The next sphere size we tried was 50 μm, as we wanted to find the smallest sphere size the coil could detect.

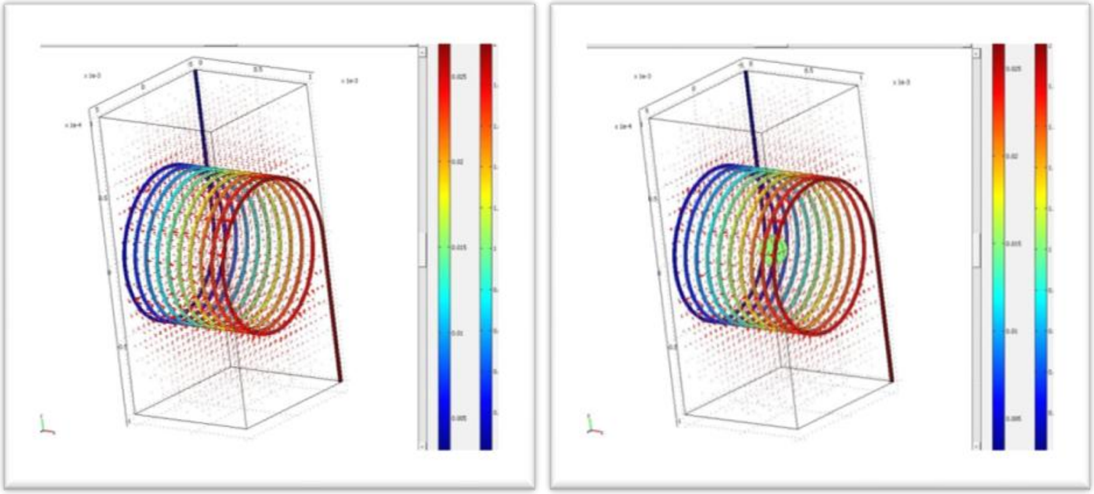

Figure 15: Magnetic flux density and electric potential for Coil 2 empty (left) and with iron (right)[2]

Figure 15 shows the inductance results for the iron spheres simulated in Coil 2. More data points between the 50 μm and 100 μm radius spheres would have produced a more useful trend line, but once the 50 μm radius sphere was determined to be detectable, we wanted to focus our efforts on simulating smaller sphere sizes. Table 4 shows the inductance results for the different sphere sizes tested in Coil 2.

Table 4: Coil 2 iron sphere detection

Radius (μm)	Inductance (nH)	Detectable (Y/N)
100	39.92003	Y
50	39.73173	Y
40	39.73200	Y
30	39.71885	Y
20	39.71283	N
10	39.71311	N

---

[2] Full size versions of these figures are available in Appendix C.

Adding more turns showed a definite improvement over Coil 1, with Coil 2 being able to detect a sphere with a radius of 30 μm compared to the 200 μm radius sphere that Coil 1 was able to detect.

3.2.2.3 Coil 3

With Coil 3, we further increased the number of turns resulting in a 15 turn coil with a diameter of 1.0 mm. We used the same sphere sizes that we used with Coil 2.

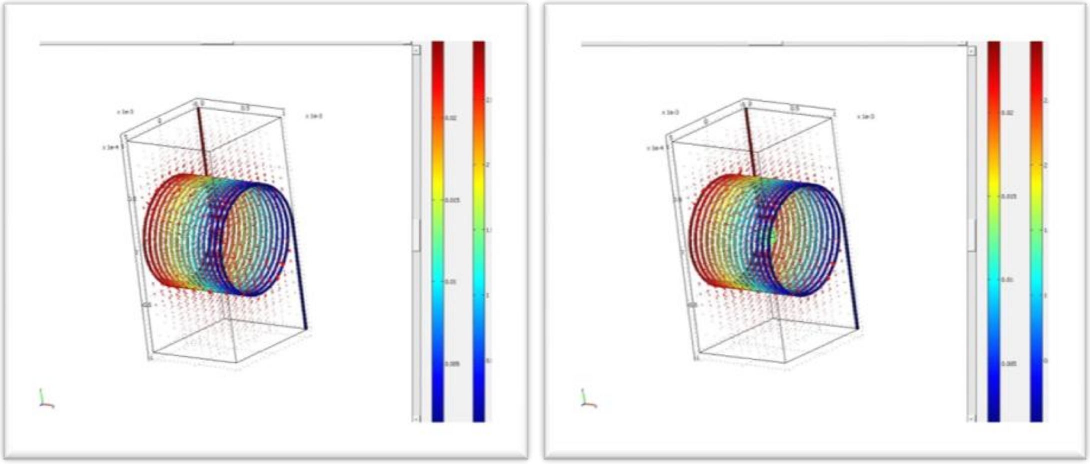

Figure 16: Magnetic flux density and electric potential for Coil 3 empty (left) and with iron (right)[3]

Table 5 lists the inductance values for the sphere sizes simulated in Coil 3, and indicates whether or not they were detectable.

---

[3] Full size versions of these figures are available in Appendix C.

Table 5: Coil 3 iron sphere detection

Radius (µm)	Inductance (nH)	Detectable (Y/N)
100	82.66429	Y
50	82.25239	Y
30	82.20701	Y
20	82.19316	N
10	82.18836	N

Additional turns did not offer any further improvement, as Coil 3 was unable to detect any spheres smaller than 30 µm in radius.

3.2.2.4 Coil 4

For Coil 4, we reduced the length of the coil from 1.0 mm to 0.5 mm, while reducing the number of turns back to 10.

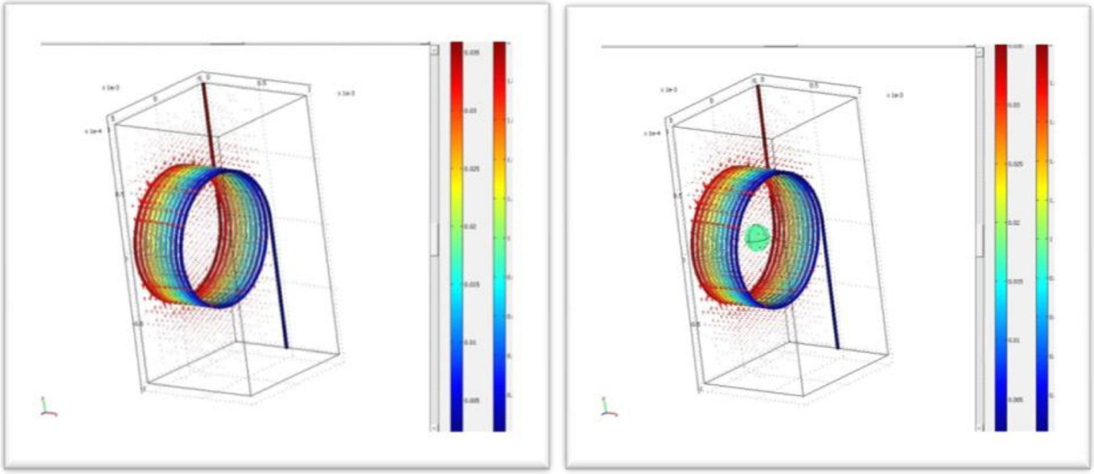

Figure 17: Magnetic flux density and electric potential for Coil 4 empty (left) and with iron (right)[4]

---

[4] Full size versions of these figures are available in Appendix C.

Table 6 shows that once again, there is no problem with detecting the 100 μm radius sphere, and without simulating any sphere sizes in between, we reduced the sphere radius to 20 μm to see if this coil design is an improvement over the previous coils. From Table 6, we see that Coil 4 is capable of detecting a sphere with a radius of 10 μm.

Table 6: Coil 4 iron sphere detection

Radius (μm)	Inductance (nH)	Detectable (Y/N)
100	57.70529	Y
20	57.46587	Y
10	57.45934	Y
9	57.46230	N
8	57.45461	N

3.2.2.5 Coil 5

In our design for Coil 5, we wanted to determine if further reducing the length would offer an additional improvement in sphere detection. We again started with the 100 μm radius sphere, and then simulated a 10 μm radius sphere.

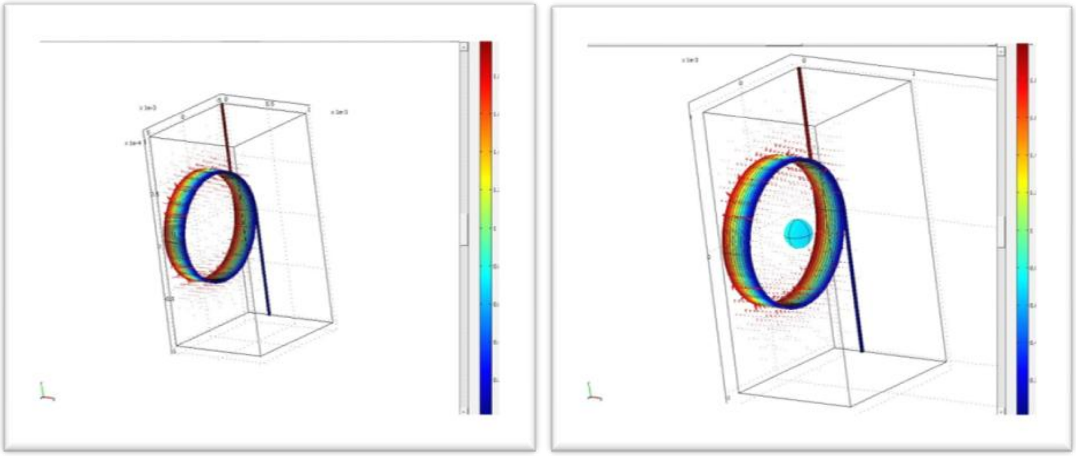

Figure 18: Magnetic flux density and electric potential for Coil 5 empty (left) and with iron (right)[5]

From Table 7, the 10 µm radius sphere was not detectable with this coil design.

Table 7: Coil 5 iron sphere detection

Radius (µm)	Inductance (nH)	Detectable (Y/N)
100	67.79670	Y
10	67.74617	N
5	67.74762	N

A lack of improvement over Coil 4 was surprising, as this design had a larger inductance with a smaller volume. The coil diameter was too large to detect any smaller sized particles, so it was reduced for the next coil design.

---

[5] Full size versions of these figures are available in Appendix C.

3.2.2.6 Coil 6

Coil 6 is the first coil with a smaller diameter. It had a diameter of 0.2 mm, compared to the 1.0 mm diameters of the previous coils. The length and number of turns remained the same as Coil 5 at 0.25 mm and 10, respectively. The other property that changed for Coil 6 was the wire size. The cross-sectional area of the wires was reduced from 400 μm^2 to 25 μm^2. Because the coil diameter was reduced to 0.2 mm, we no longer simulated a 100 μm radius sphere, as the diameter of such a sphere was equal to the coil diameter.

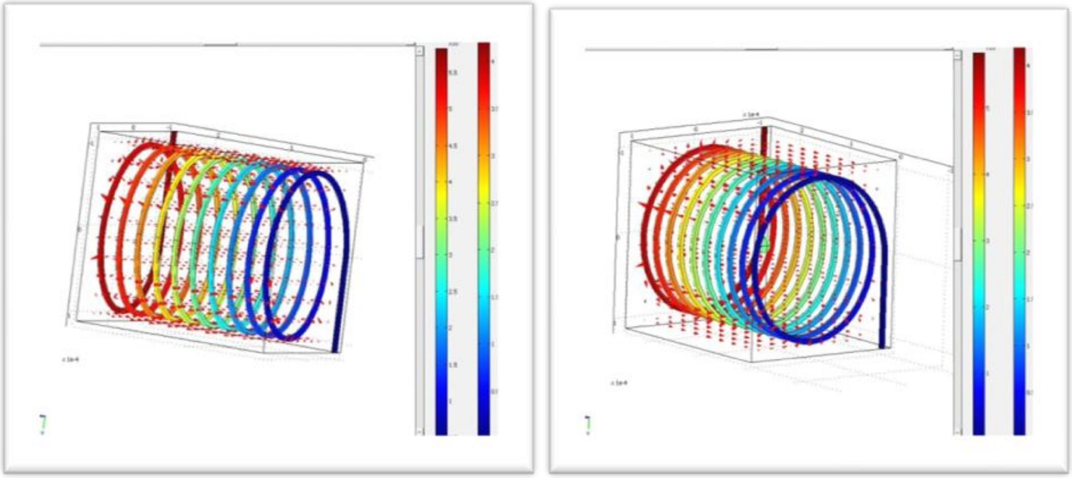

Figure 19: Magnetic flux density and electric potential for Coil 6 empty (left) and with iron (right)[6]

The design of Coil 6 can be seen in Figure 19, and although it is the same length as Coil 5, shown in Figure 18, it looks longer due to the reductions in diameter and wire size.

---

[6] Full size versions of these figures are available in Appendix C.

Table 8: Coil 6 iron sphere detection

Radius (µm)	Inductance (nH)	Detectable (Y/N)
10	5.38118	Y
8	5.380405	Y
7	5.380066	Y
6	5.379382	N
5	5.379538	N
1	5.378847	N

The reduction in coil diameter resulted in an improvement in the coil's detection ability, with Coil 6 being able to detect a sphere with a radius of 7 µm, as can be seen in Table 8.

3.2.2.7 Coil 7

For the next coil, we reduced the diameter again, this time to 0.1 mm. All other properties remained the same as Coil 6.

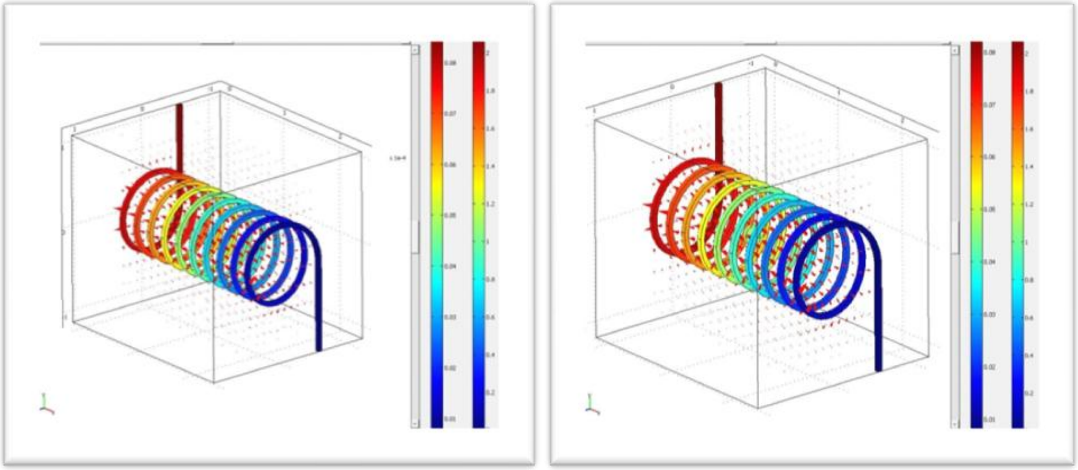

Figure 20: Magnetic flux density and electric potential for Coil 7 empty (left) and with iron (right)[7]

---

[7] Full size versions of these figures are available in Appendix C.

Figure 21 shows the inductance of Coil 7 for the different sizes of iron sphere.

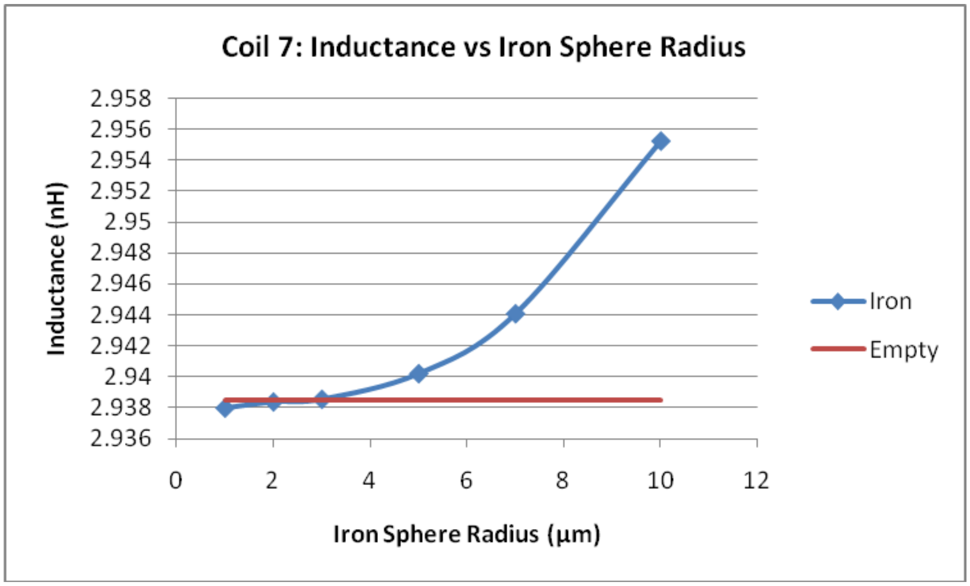

Figure 21: Coil 7 iron sphere detection

Table 9 shows the different sizes of spheres that were simulated and their corresponding inductance values, along with whether or not that sphere was detectable.

Table 9: Coil 7 iron sphere detection

Radius (µm)	Inductance (nH)	Detectable (Y/N)
10	2.955207	Y
7	2.944090	Y
5	2.940236	Y
3	2.938586	Y
2	2.938416	N
1	2.938021	N

Another decrease in coil diameter yielded an improvement in detection ability, with Coil 7 being able to detect a sphere with a radius of 3 µm.

3.2.2.8 Coil 8

Coil 8 used the same diameter, number of turns, and wire size as Coil 7, but reduced the length of the coil to 0.1 mm. The design of Coil 8 can be seen in the following figure:

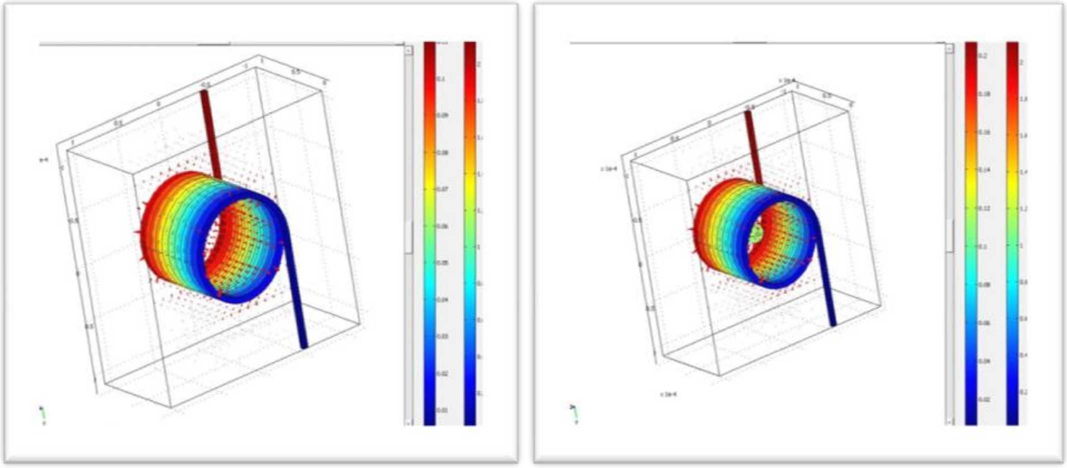

Figure 22: Magnetic flux density and electric potential for Coil 8 empty (left) and with iron (right)[8]

In figure 23, the inductance of Coil 8 is plotted against the iron sphere size, and in Table 10, the inductance values for each sphere that was simulated are listed. Coil 8 was able to detect a sphere with a radius of 1 µm.

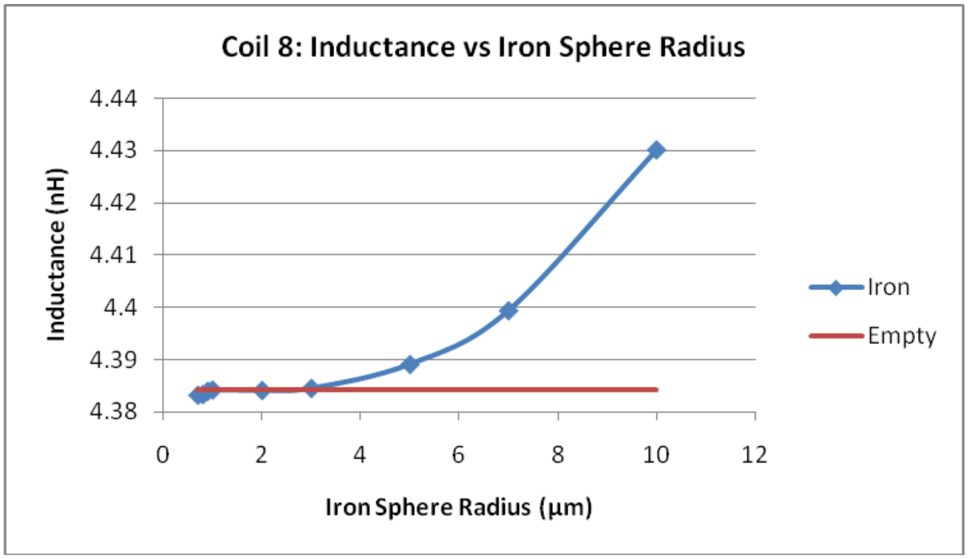

Figure 23: Coil 8 iron sphere detection

Table 10: Coil 8 iron sphere detection

Radius (µm)	Inductance (nH)	Detectable (Y/N)
10	4.430082	Y
7	4.399386	Y
5	4.389133	Y
3	4.384547	Y
2	4.384150	Y
1	4.384255	Y
0.9	4.384016	N

---

[8] Full size versions of these figures are available in Appendix C.

0.8	4.383378	N
0.7	4.383258	N

3.2.2.9 Coil 9

Coil 9 was a step backwards from Coil 8, in that we reduced the number of turns to 5 from 10. This was done to test if the extra turns were still necessary at a smaller diameter size, or if they did not help as with going from 10 turns with Coil 2 to 15 turns with Coil 3.

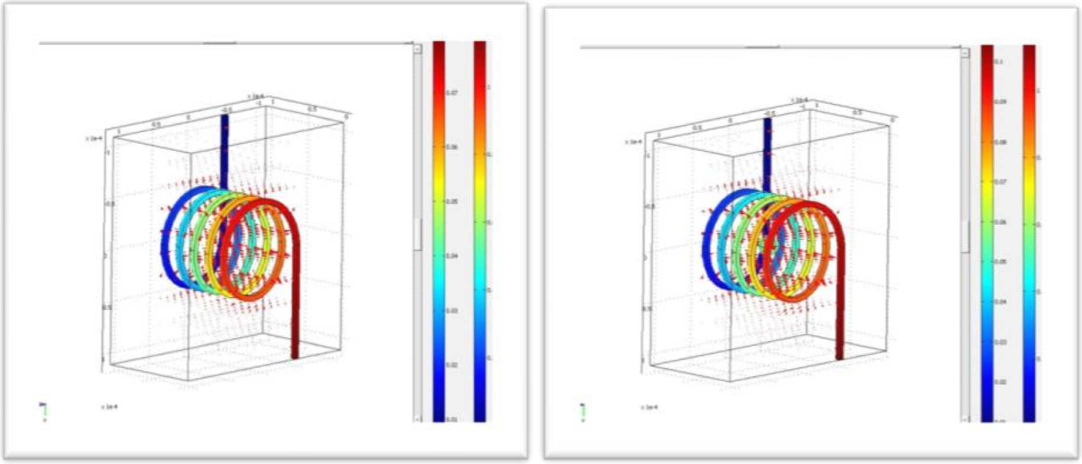

Figure 24: Magnetic flux density and electric potential for Coil 9 empty (left) and with iron (right)[9]

Figure 25 shows how the inductance of Coil 9 changes with the iron sphere radius. Radii from 10 μm down to 1 μm were simulated.

---

[9] Full size versions of these figures are available in Appendix C.

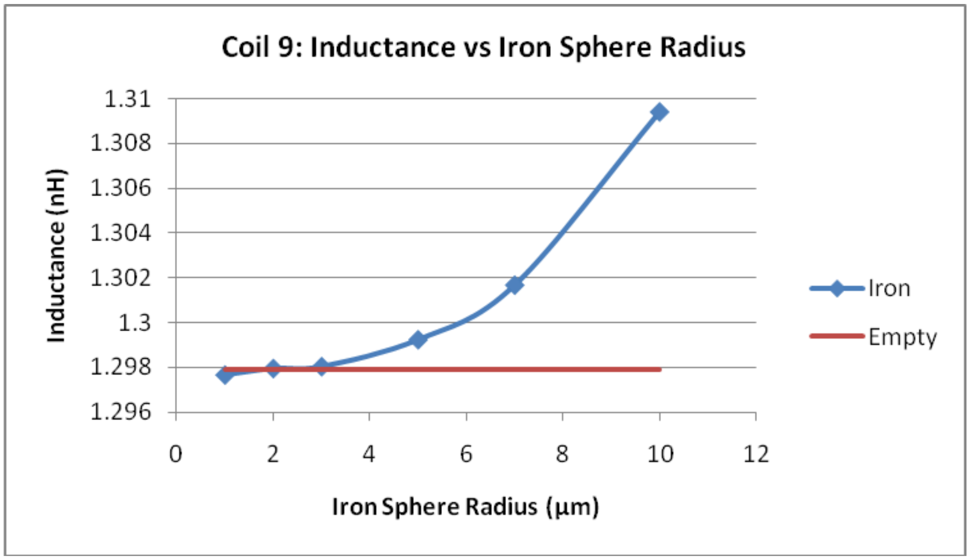

Figure 25: Coil 9 iron sphere detection

Results for the inductance value of the coil with each of the simulated spheres are listed in Table 11. While Coil 8 was able to detect a 1 µm radius sphere, Coil 9 could not, with a 2 µm sphere being the smallest size that it could detect.

Table 11: Coil 9 iron sphere detection

Radius (µm)	Inductance (nH)	Detectable (Y/N)
10	1.309412	Y
7	1.301681	Y
5	1.299244	Y
3	1.298042	Y
2	1.297957	Y
1	1.297670	N

3.2.2.10 Coil 10

For Coil 10, we reduced the length to 0.05 mm, but kept all other properties the same as Coil 9. We simulated sphere sizes from 10 µm down to 0.1 µm.

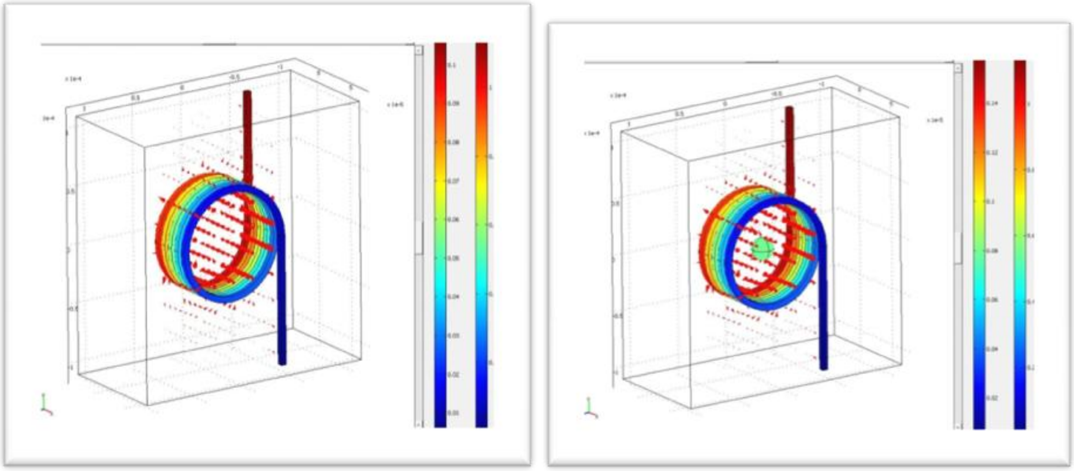

Figure 26: Magnetic flux density and electric potential for Coil 10 empty (left) and with iron (right)[10]

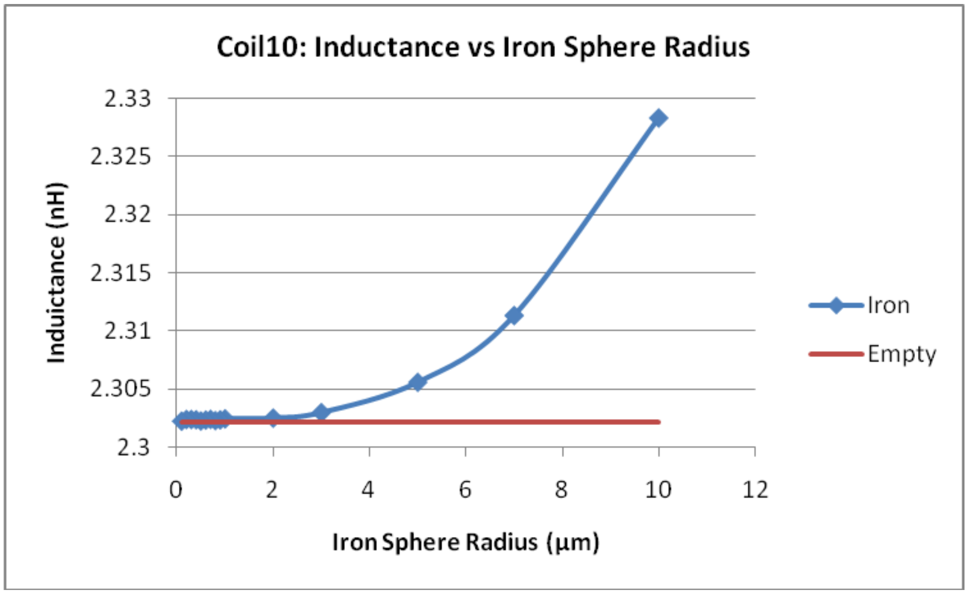

Figure 27: Coil 10 iron sphere detection

---

[10] Full size versions of these figures are available in Appendix C.

In Figure 27, the inductance value for each of the simulated sphere sizes is shown. Table 12 lists the inductance values for each of these sphere sizes, as well as whether or not the sphere was detectable.

Table 12: Coil 10 iron sphere detection

Radius (µm)	Inductance (nH)	Detectable (Y/N)
10	2.328272	Y
7	2.311312	Y
5	2.305578	Y
3	2.302972	Y
2	2.302502	Y
1	2.302440	Y
0.9	2.302357	Y
0.8	2.302287	Y
0.7	2.302399	Y
0.6	2.302334	Y
0.5	2.302261	Y
0.4	2.302366	Y
0.3	2.302384	Y
0.2	2.302381	Y
0.1	2.302242	Y

Coil 10 showed the best results of any. Simulations of smaller iron spheres were unsuccessful, as Comsol could not calculate a solution with the large geometry difference between the coil and sphere.

From the simulation results, smaller coils result in better sensitivity. However, there is a trade off here; smaller coils also have smaller inductance values, making the inductance change harder to pick up in a circuit with real world noise. Out of the ten coils simulated, Coil 10 had the best sensitivity, and it was capable of detecting an iron sphere with a radius of 0.1 µm.

However, looking closer at Figure 27, there is some instability in the inductance value as the iron sphere size becomes less than 1 µm. This behaviour is shown in Figure 28. These results suggest that there is some noise in the simulation results, and the condition we used for determining whether a particle was detectable may not be valid when only a single point is considered.

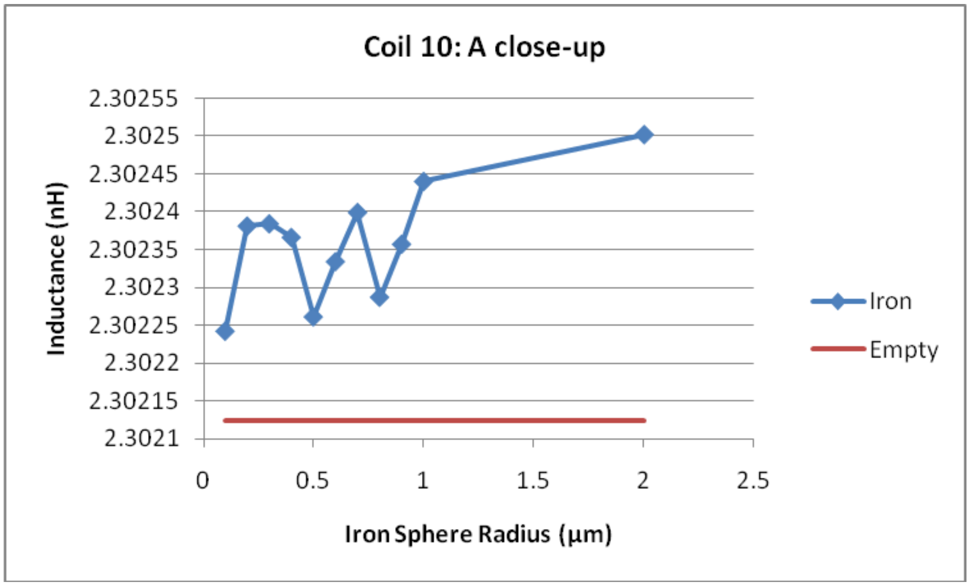

Figure 28: Close-up of Coil 10 iron sphere detection

The noise in the simulation results could be due to the large difference in size between the coil and the sphere, and the size of the mesh for each object. Figure 29 shows the mesh for Coil 10 with a 10 µm radius sphere, and Figure 30 shows the mesh for Coil 10 with a 1 µm radius sphere.

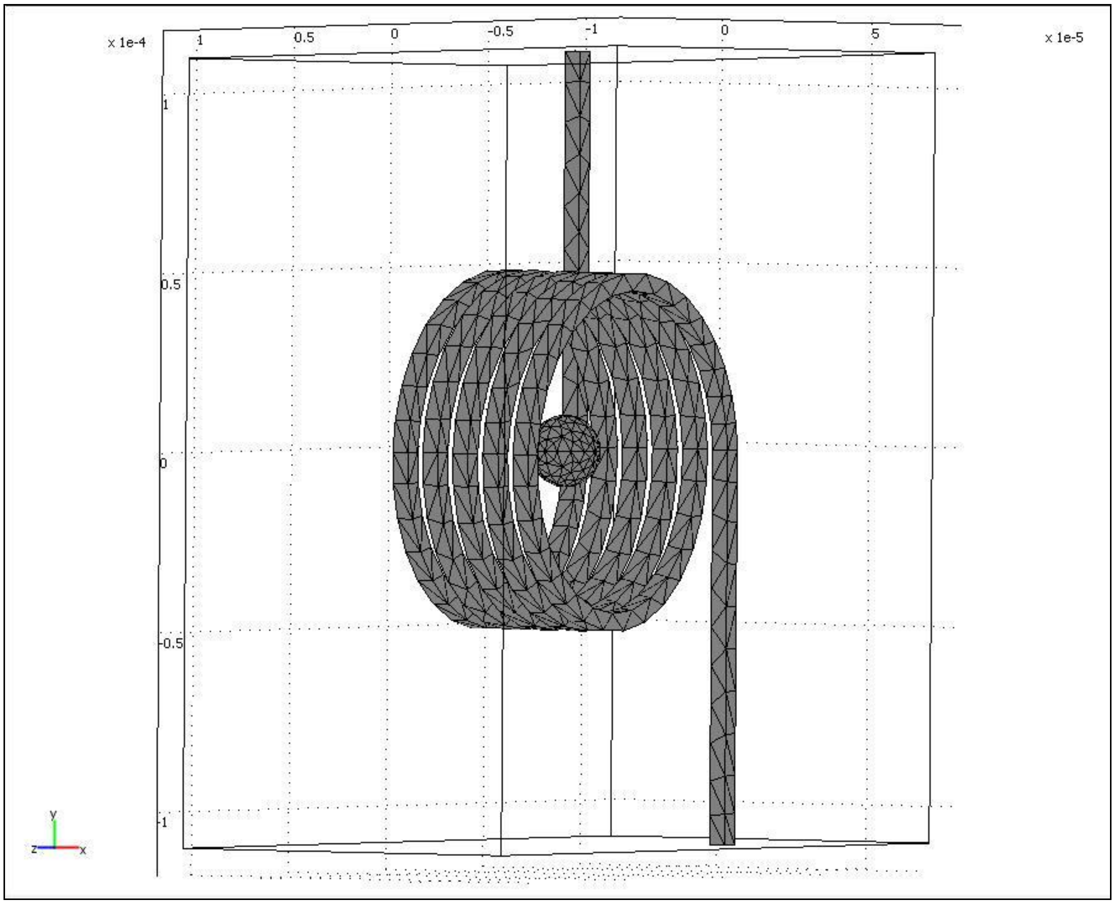

Figure 29: Mesh for Coil 10 with 10 µm sphere

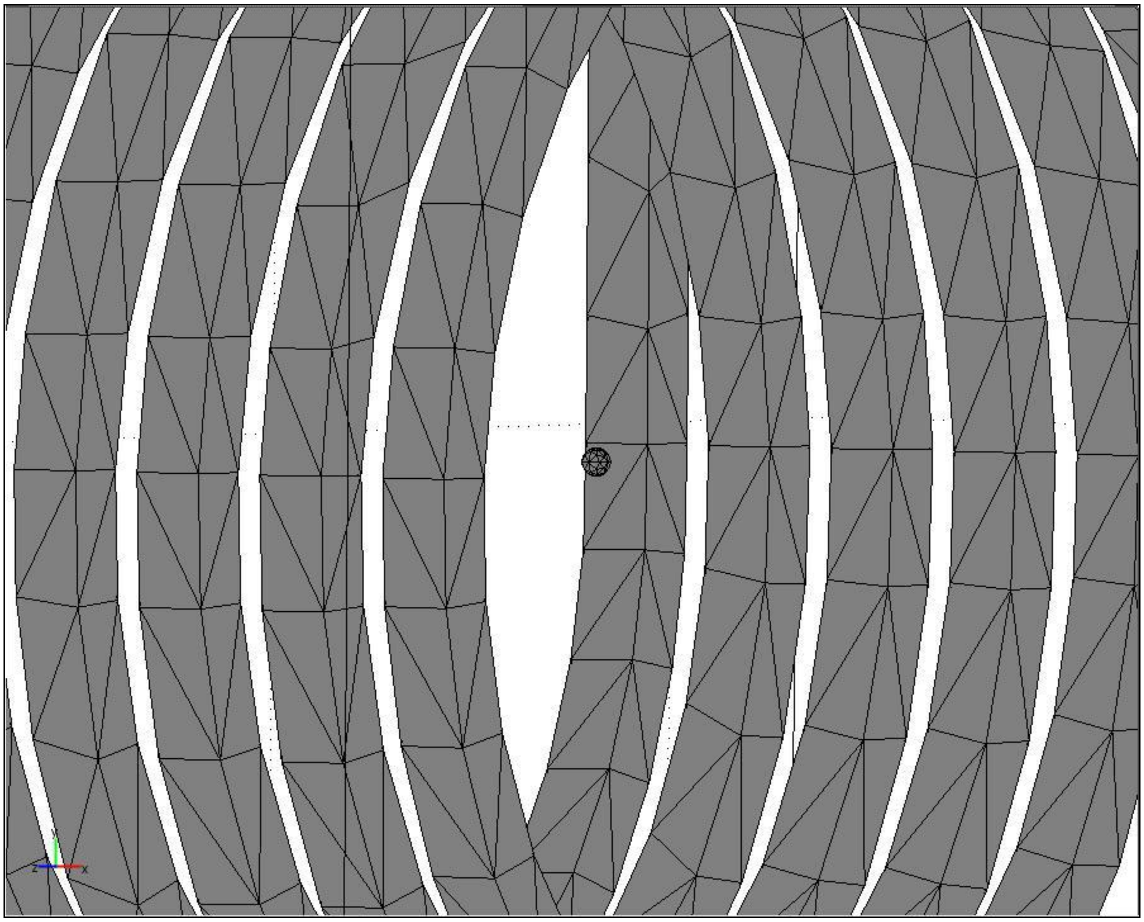

Figure 30: Mesh for Coil 10 with 1 μm sphere

The size of the mesh on the 1 μm radius sphere is much smaller than the mesh on the coil, and this size difference could be the reason for the abnormal results for Coil 10.

3.2.3 Multipoint detection limit

In order to compensate for the noise in the simulation results for iron sphere sizes that approached a coil's detectability limit, we collected more data to better understand the inductance of the coil. The position of the sphere was moved through a series of points along the X-axis of the coil, as shown in Figure 31, and the inductance value was simulated for each position.

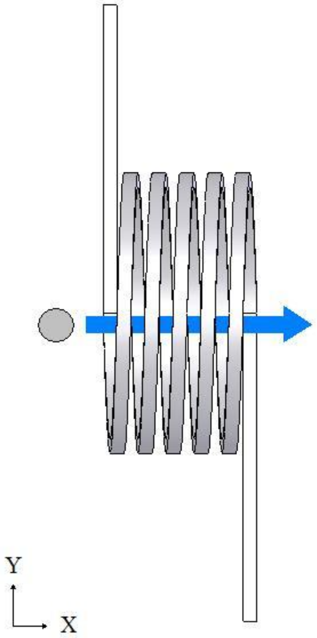

Figure 31: The inductance of the coil was simulated with an iron sphere at different points along the X-axis.

Our expectation was that the inductance will be highest when the sphere is in the middle of the coil and lowest when it is outside of the coil due to the magnetic field being strongest in the centre of the coil. Figure 32 shows Coil 10 with the resulting inductance values for several different sized iron spheres plotted against the position of the centre of the sphere. The sinusoid represents the position of the coil.

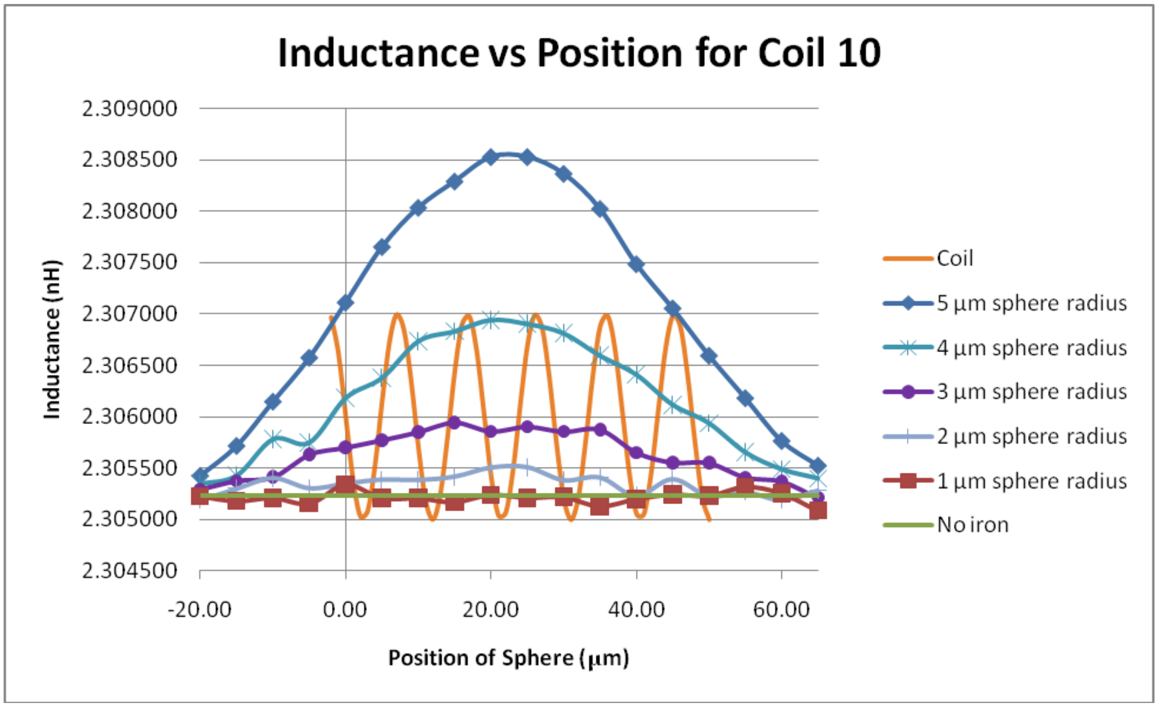

Figure 32: Results of simulations for Coil 10. The sinusoid shows the relative position of the coil.

For 3 µm and larger radius spheres, the inductance behaves as expected. It is smaller when the sphere is outside of the coil and increases as the sphere moves towards the coil centre. However, for the 1 µm and 2 µm radius spheres, the inductance remains mostly flat. Although the inductance is higher than the inductance of the empty coil, this deviation from the expected behavior suggests that a coil of this design would not be able to reliably detect particle smaller than a 3 µm radius sphere. This result is 30 times larger than the sphere that the previous set of simulations deemed detectable. A new set of coils was simulated using this method of sweeping the sphere from one side to the other and their properties are summarized in the following table:

Table 13: Properties of additional coils

Coil	Diameter (mm)	Length (mm)	Turns	Wire cross-sectional area (μm^2)	Inductance (nH)
10	0.100	0.05	5	25	2.302124
11	0.050	0.05	5	25	0.7940190
12	0.025	0.05	5	25	0.2903874
13	0.025	0.05	5	1.0	0.3646860
14	0.025	0.01	5	1.0	0.7203552
15	0.025	0.02	10	1.0	1.669687

Decreasing the diameter of the coil allows for smaller spheres to be detected, as can be seen in the following figure:

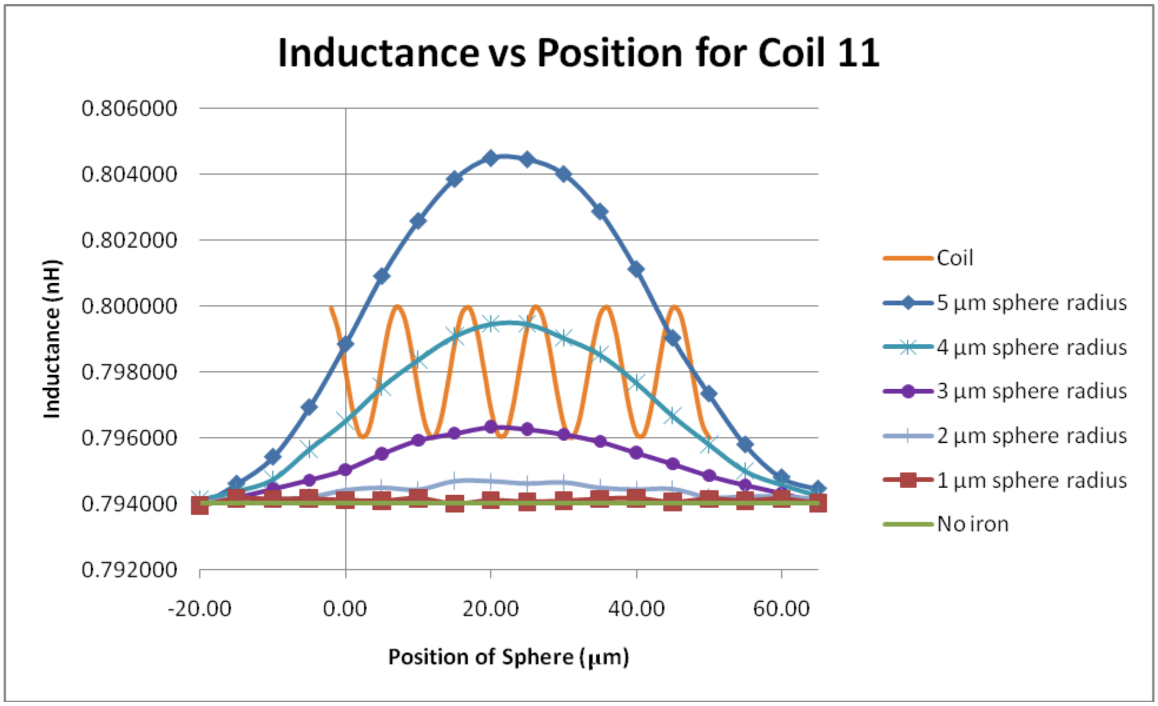

Figure 33: Results of simulations for Coil 11. The sinusoid shows the relative position of the coil.

Figure 34 focuses on only the 1 μm and 2 μm radius spheres, and we see that the 2 μm sphere now displays the expected shape. The 1 μm sphere is still not detectable, however.

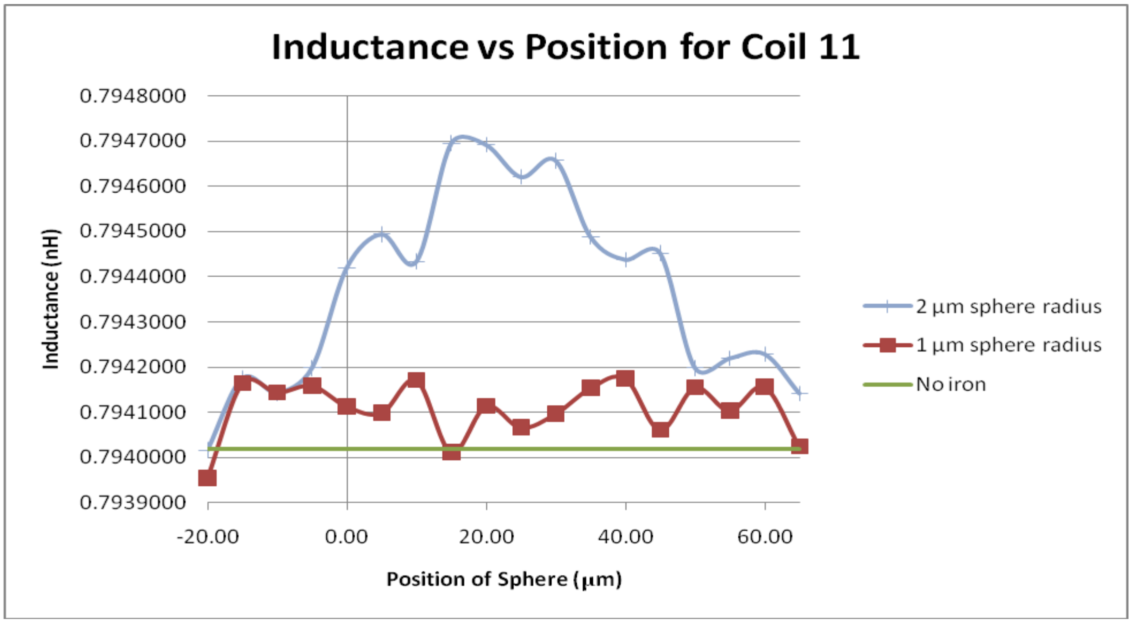

Figure 34: Simulation results for Coil 11, showing just the 1 μm and 2 μm spheres

Further decreasing the coil diameter improves the inductance curve even more.

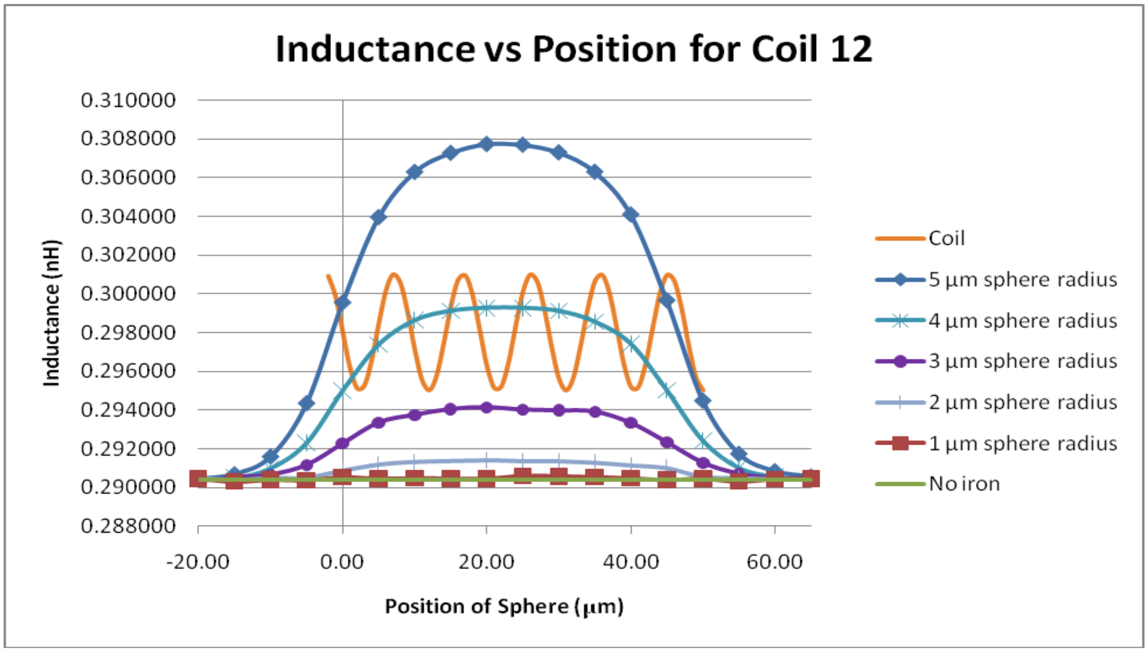

Figure 35: Results of simulations for Coil 12. The sinusoid shows the relative position of the coil.

Looking again at just the 1 µm and 2 µm spheres shows that the 2 µm inductance curve is much cleaner than for the previous coil, and even the 1 µm sphere is starting to look more like the expected curve.

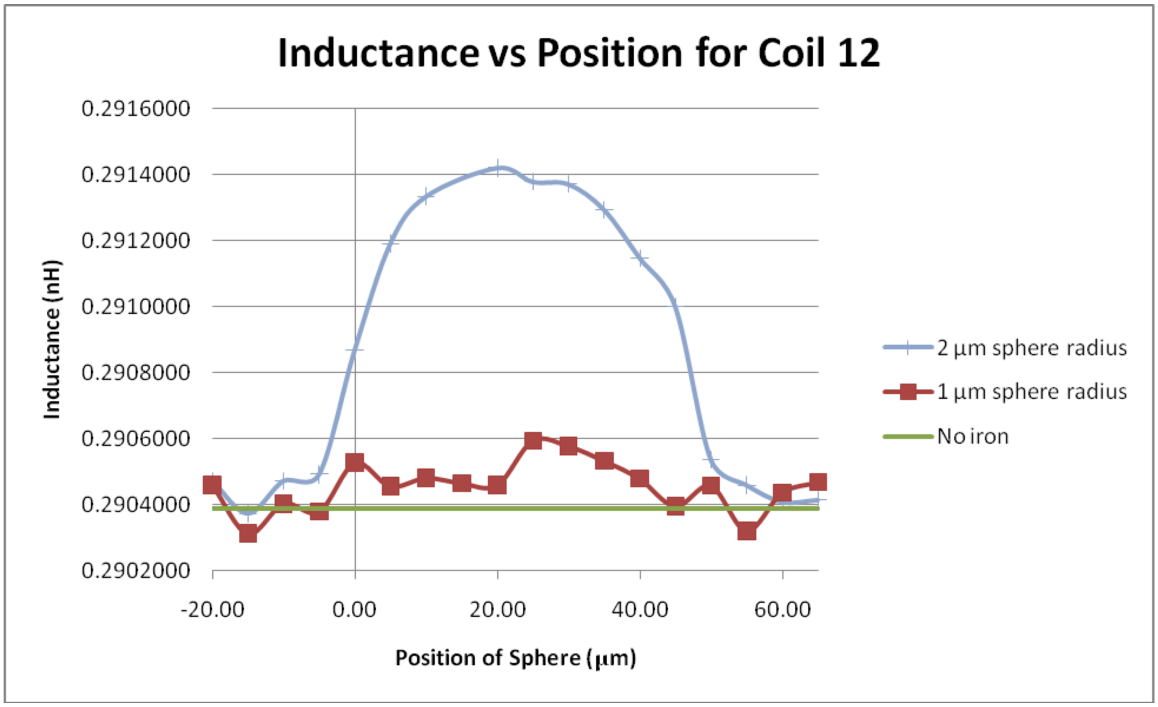

Figure 36: Simulation results for Coil 12, showing just the 1 μm and 2 μm spheres

In the last three coils, the only dimension that has been changed is the diameter. As can be seen in the following figure, the size of the coil wires is becoming more significant when compared with the coil diameter.

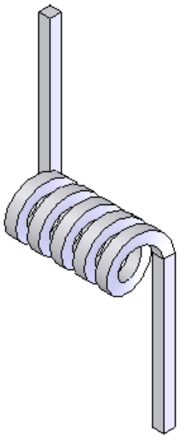

Figure 37: 3D model used for Coil 12. Coil diameter is 25 μm and wire cross-sectional area is 25 μm^2.

The next coil design reduces the wire size from 25 μm^2 to 1.0 μm^2, as can be seen in the following figure. The coil diameter and length are the same in both of these figures.

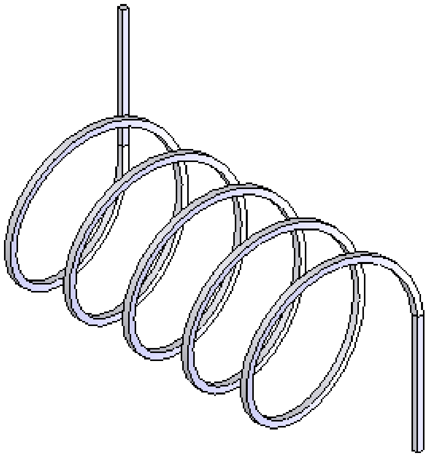

Figure 38: 3D model used for coil 13. Coil diameter is 25 μm and wire cross-sectional area is 1.0 μm2.

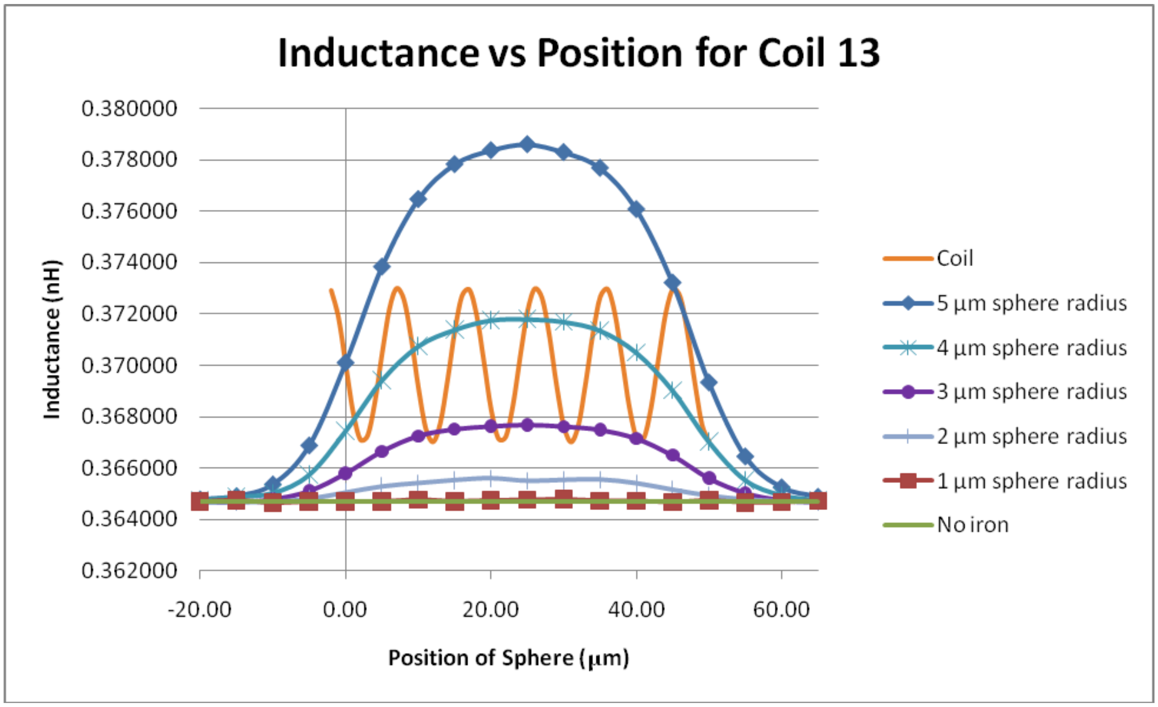

Figure 39: Results of simulations for Coil 13. The sinusoid shows the relative position of the coil.

Reducing the wire size yields a very similar looking graph. However, when comparing the percentage change in inductance from the empty coil for each of the two 25 μm diameter coils, we see that Coil 12 yields a 2% higher percentage change for the 5 μm radius sphere than Coil 13. Figure 40 shows a side-by-side comparison of the percentage change in inductance for Coils 12 and 13.

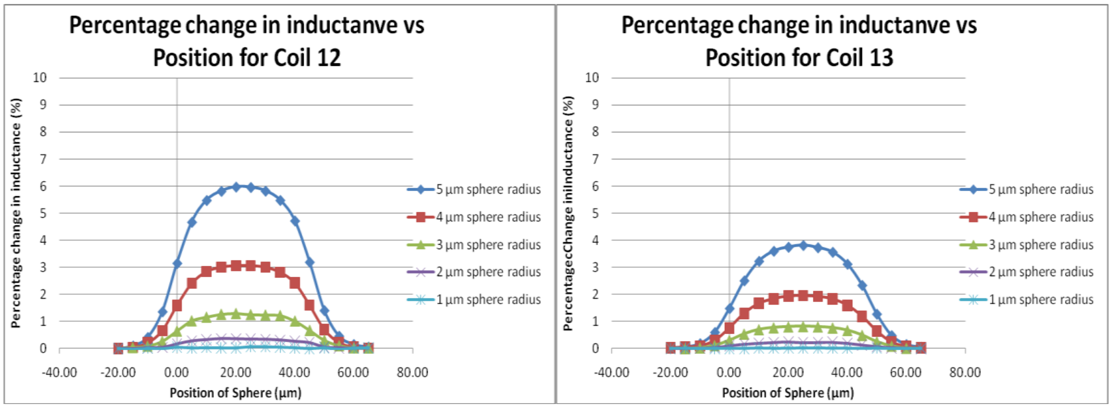

Figure 40: Comparison of how inductance changes percentagewise for Coils 12 and 13

A side effect of reducing the wire size is that the gap between each loop increases from 3.33 μm to 7.33 μm. In the next coil, we reduce the coil length so that the gaps between the loops are 0.67 μm.

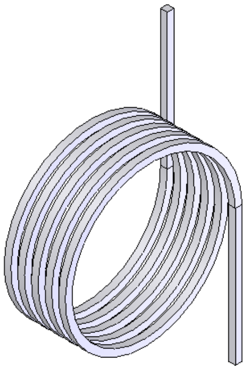

Figure 41: 3D model used for Coil 14. Coil diameter is 25 μm and wire cross-sectional area is 1.0 μm2. The coil length is 0.01 mm.

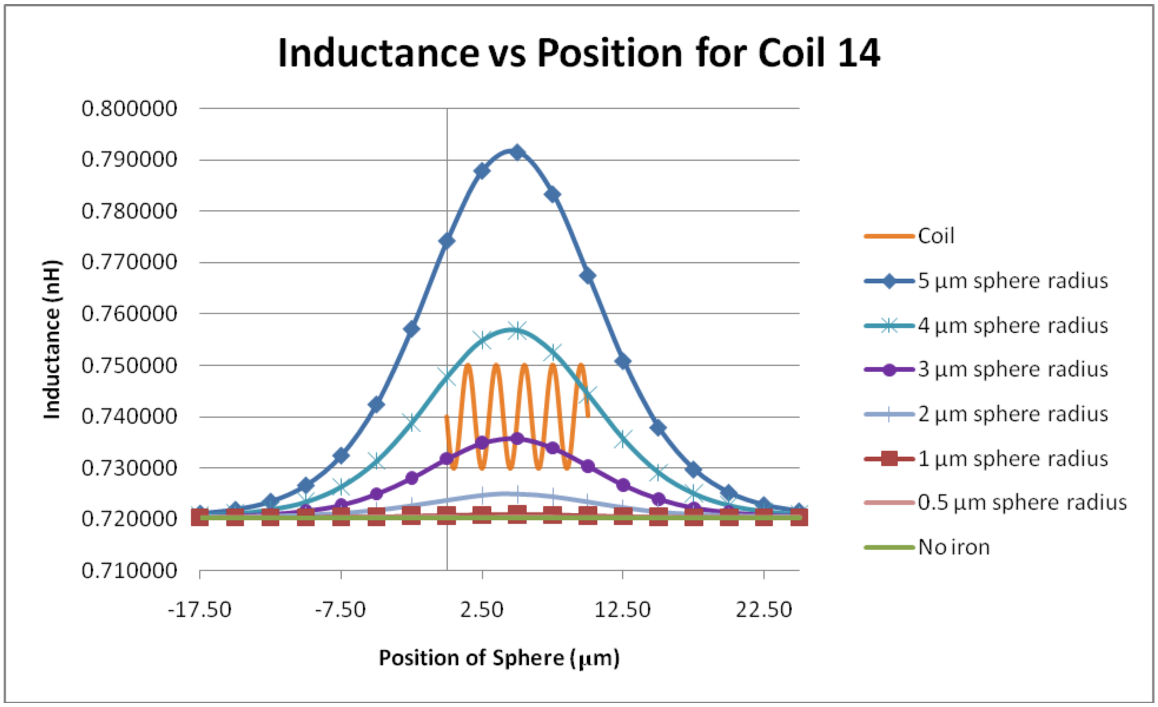

Figure 42: Results of simulations for Coil 14. The sinusoid shows the relative position of the coil.

Immediately, we notice that the width of the 5 μm sphere radius curve, at the inductance level that is 50% of the peak increase in inductance value, is 15 μm compared to 46 μm for Coil 13. Also of note is that we have now included simulation results for a 0.5 μm radius sphere. With Coil 14, the 1 μm radius sphere is now detectable, although the 0.5 μm radius sphere is not.

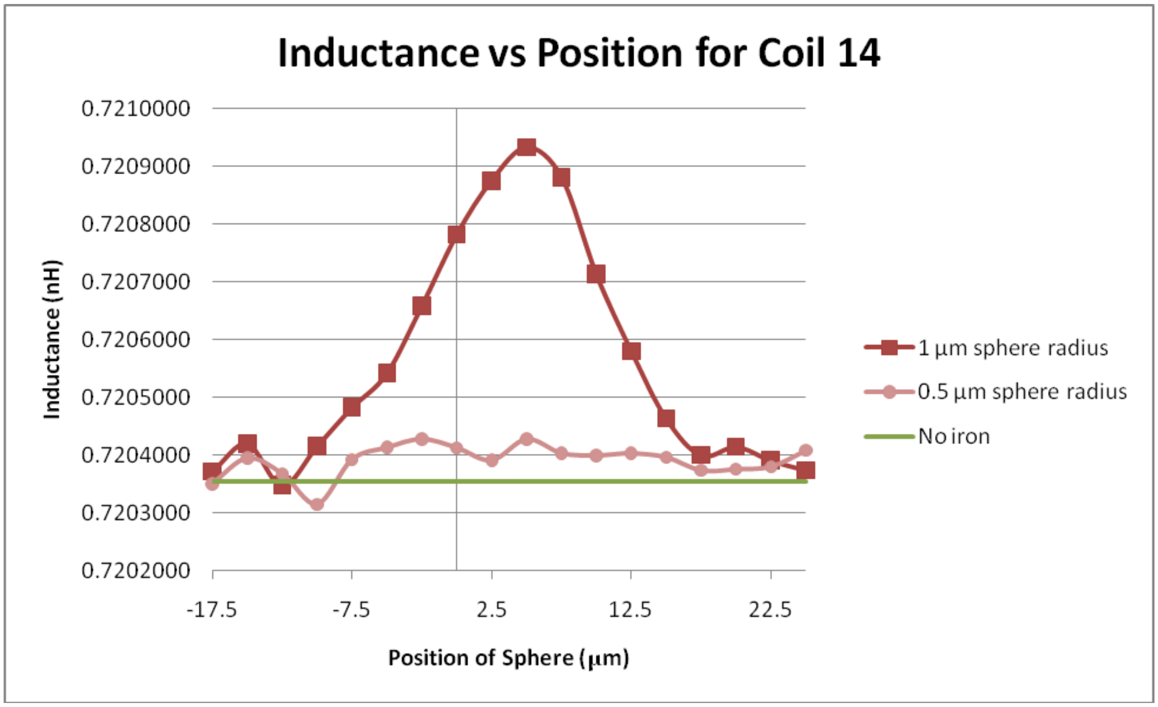

Figure 43: Simulation results for Coil 14, showing just the 0.5 and 1 µm spheres

Figure 44 shows the percentage change in inductance for Coil 14, where we see improvements of 4% and 6% over the peak percentage change in inductance for Coil 12 and Coil 13, respectively.

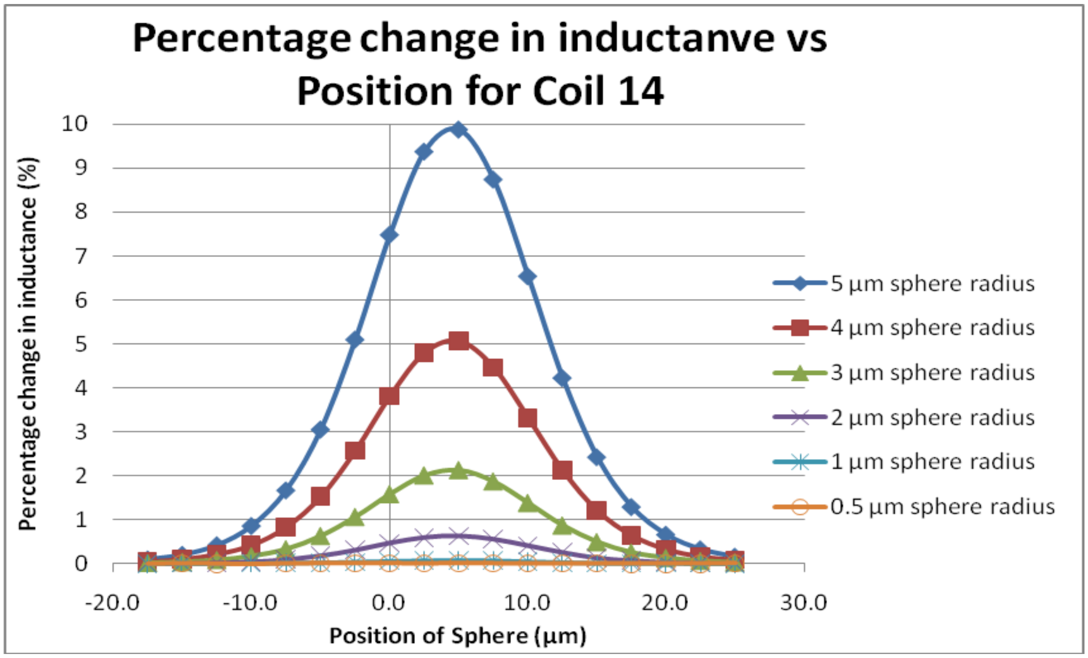

Figure 44: Change in inductance for Coil 14 shown in a percentage scale.

Doubling the number of turns in Coil 14, as well as the length, we obtain the following graph:

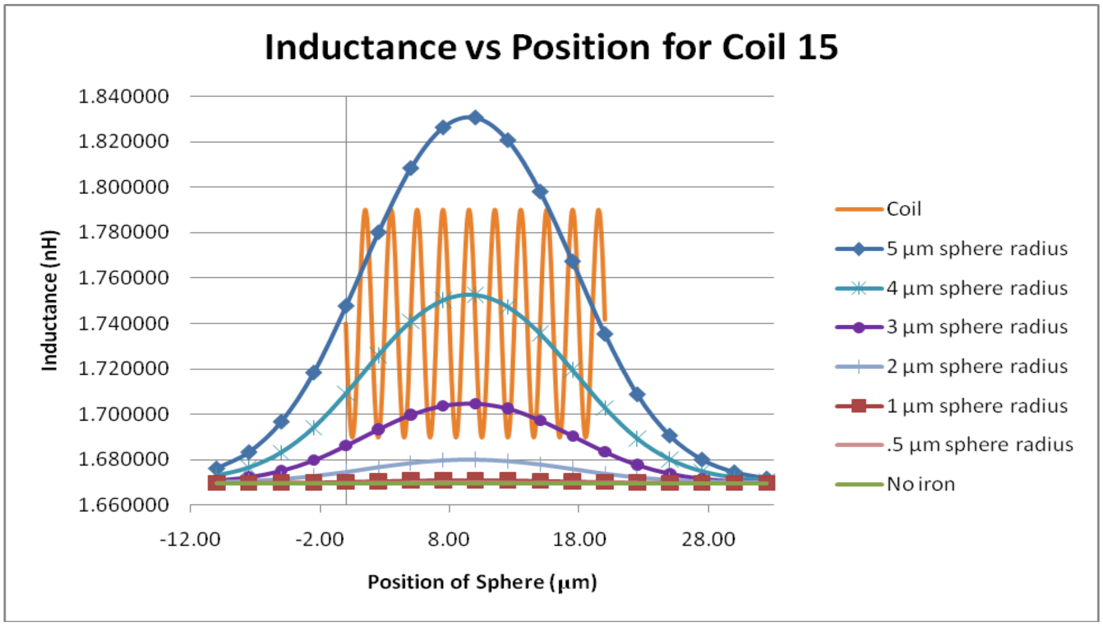

Figure 45: Results of simulations for Coil 15. The sinusoid shows the relative position of the coil.

The main differences from the results of Coil 14 are that the width of the curves at the 50% peak point has increased to 19 µm, and the overall inductance has gone up from a base level of 0.7203552 nH to 1.669687 nH, which is to be expected considering that the number of turns has doubled. The close up view of just the 1 µm and 0.5 µm radius spheres shows a cleaner curve for the 1 µm, and even the 0.5 µm radius sphere shows the increase in inductance we expect when the sphere is inside the coil, indicating that it is detectable.

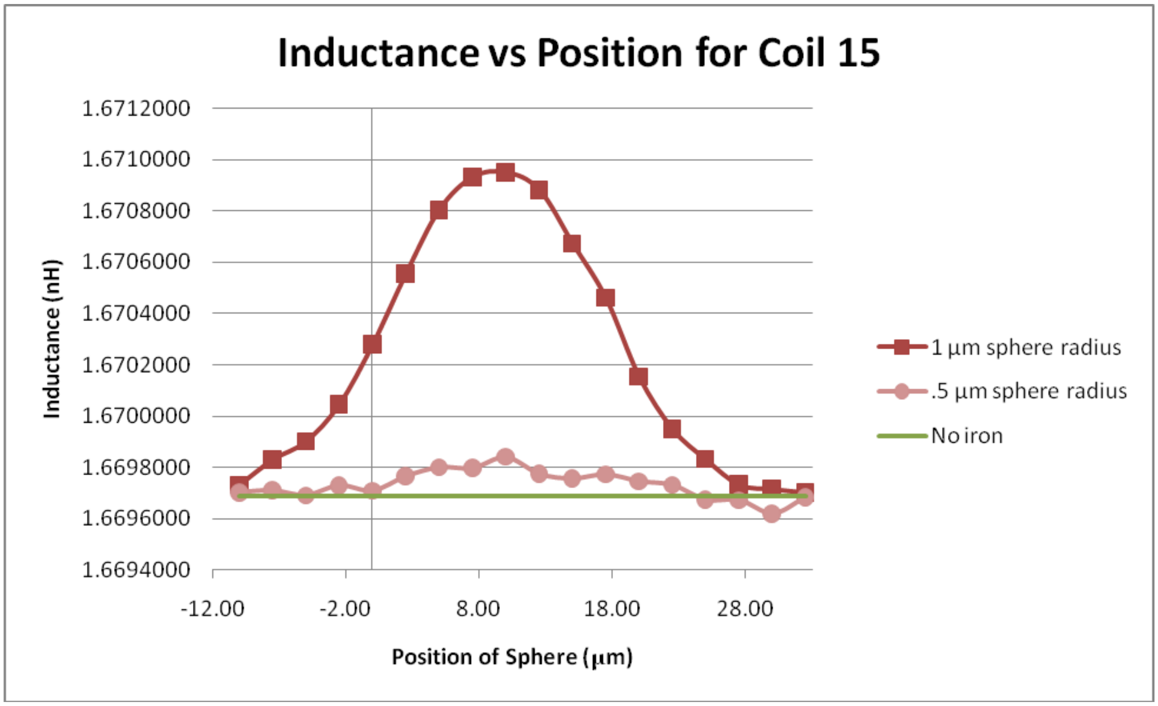

Figure 46: Simulation results for Coil 15, showing just the 0.5 and 1 µm spheres

The trade-off for this slightly improved sensitivity, however, is that the percentage change in inductance is slightly lower.

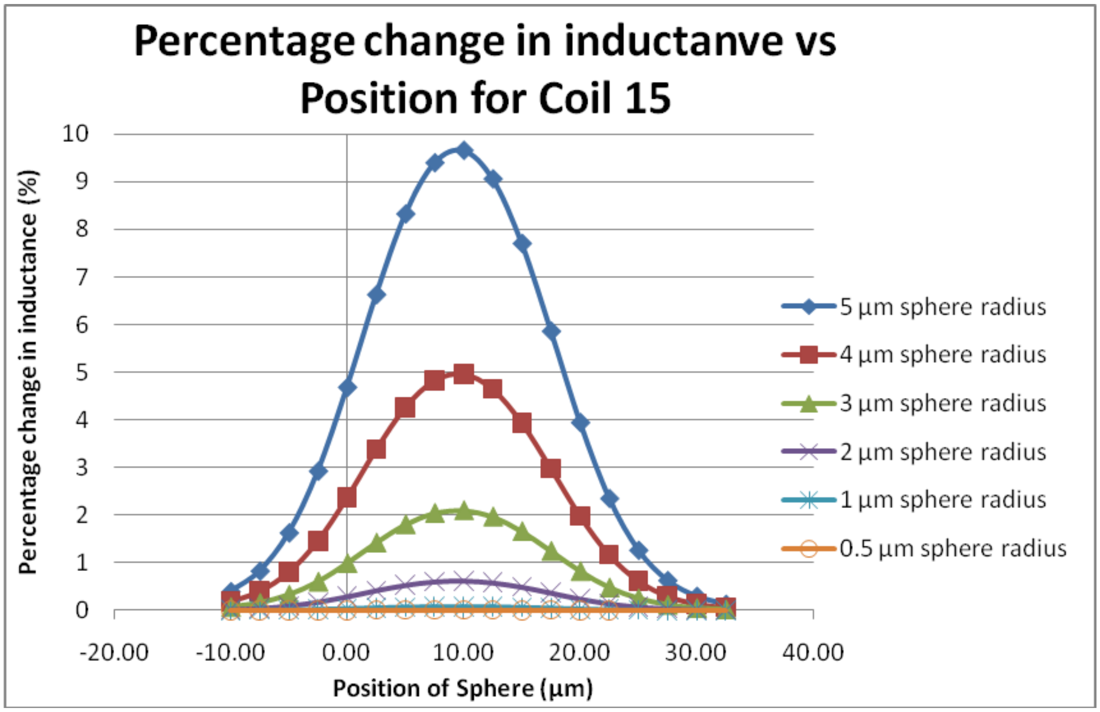

Figure 47: Change in inductance for Coil 15 shown in a percentage scale.

3.2.4 Additional considerations

After thoroughly examining the behaviour of the coils as spheres of different sizes were moved through the coils along the X-axis, we wanted to simulate other scenarios to better characterize the coils.

The first scenario we wanted to consider was the effect of changing the distribution of the iron inside the coil. In order to find out, we used a cube that had the same volume as the 5 μm radius sphere (see Appendix A for volume and dimension calculations). The cube was moved through the coil in the same manner as the spheres, and the inductance was simulated at each position along the X-axis. The inductance values for the cube are shown in the following figure along with the inductance values for the sphere of the same volume:

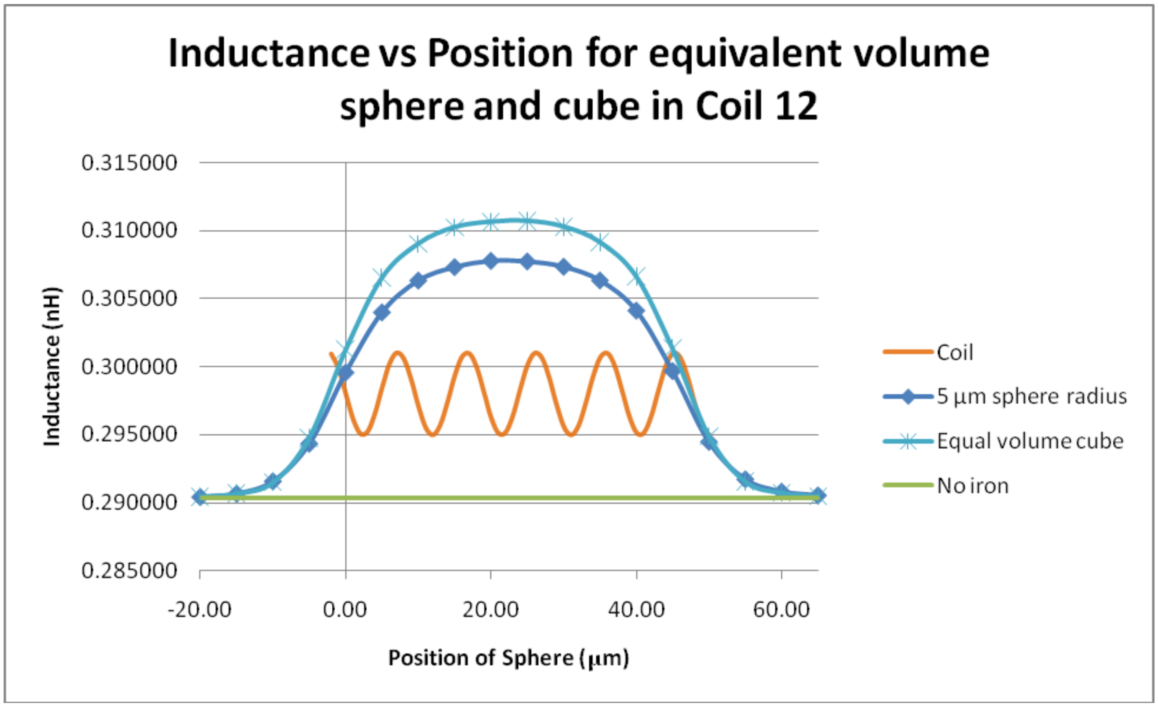

Figure 48: Simulation results comparing equivalent volume sphere and cube. The sinusoid represents the relative coil position.

For the same volume, the cube inductance change is greater for a cube than a sphere. To understand why this result occurs, we need to consider how the volume of each shape is distributed along the X-axis. Consider when each object is in the centre of the coil. Because the side length of the cube is smaller than the diameter of the sphere, there is more iron concentrated towards the centre of the coil. We know that the inductance change is largest when the object is in the centre of the coil, so the shape that has more of its volume concentrated centrally will have a larger change in inductance. This phenomenon shows us that for the final device, we will have an easier time detecting the iron if it can be concentrated in the centre of the coil as opposed to spread out throughout it.

An assumption that has been made in this thesis is that we can use a single sphere of iron to represent a number of smaller particles. In order to validate this assumption, we took an iron cube and then split it up into eight smaller cubes, and moved this group of cubes through the coil. We then increased the spacing between the cubes and repeated the simulation. The single cube used for this series of simulations had a side length of 8 μm, while the side length of the eight smaller cubes was 4 μm.

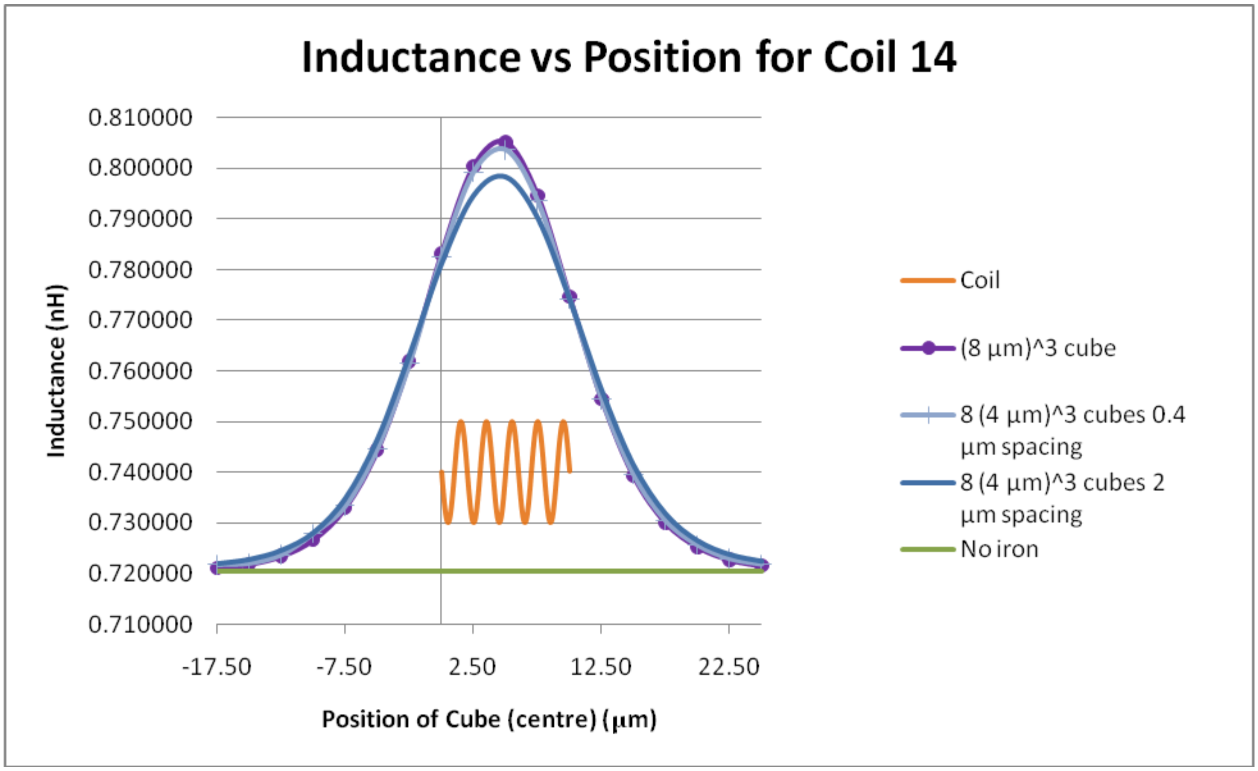

Figure 49: Simulation results comparing single cube with side length of 8 μm to 8 cubes with side length of 4 μm. The sinusoid represents the relative position of the coil.

Splitting the cube into eight smaller pieces causes the inductance to drop by only 0.2%. After increasing the space between cubes, the peak inductance value drops by 0.8%. This finding supports the idea of using a single iron sphere to represent a collection of iron nano-particles, as long as the particles are kept close together.

Throughout all of the simulations that have been presented so far, the iron object has always been centred with respect to both the Y-axis and Z-axis. The expectation is that we will see symmetry when moving the object along the Y-axis and Z-axis. To confirm this assumption, we simulated this scenario in both Coil 13 and Coil 14 using a 3 µm radius iron sphere.

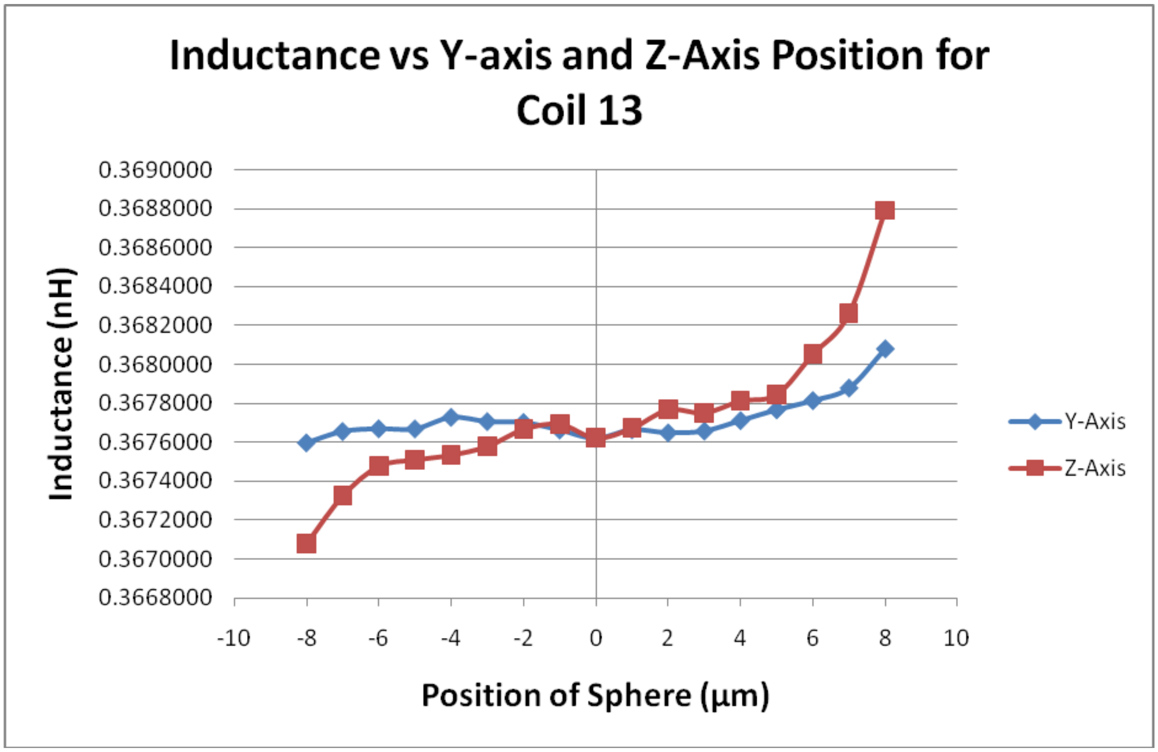

Figure 50: Simulation results for moving a 3 µm sphere along the Y-axis and Z-axis.

The results for Coil 13 were surprising. Upon examining the model in closer detail, the reason for the asymmetrical behaviour became apparent. The 3 µm radius sphere was smaller than the gap between the loops of the coil, so when the sphere was on one side, it was right next to a wire and the inductance was higher. However, when it was moved to the other side, the sphere was sitting in the space between two wires, so it had a lower impact on the coil's inductance. Coil 14 has a gap of 3.33 μm between the coil loops, which is smaller than the diameter of the sphere, so we see the symmetrical behaviour that we expected.

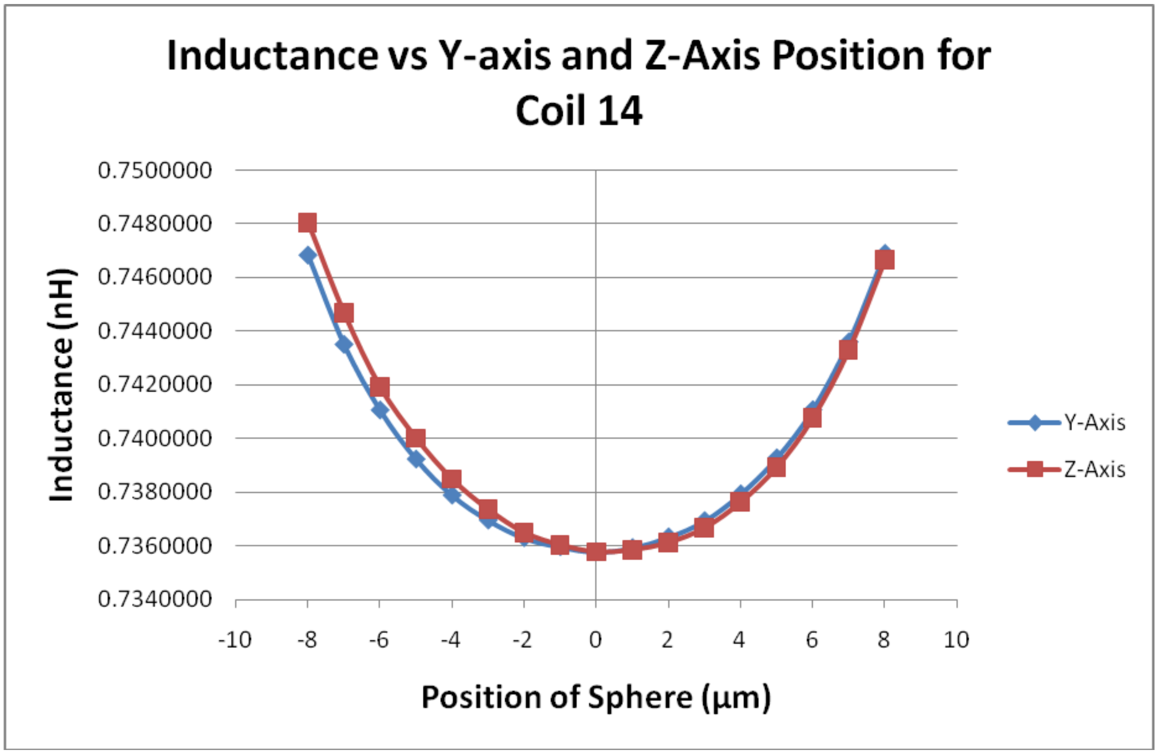

Figure 51: Simulation results for moving a 3 μm sphere along the Y-axis and Z-axis.

Finally, because the coil needs a channel running through it in order to pass a test fluid through it, we wanted to see what impact inserting a glass tube into the coil would have on the inductance values.

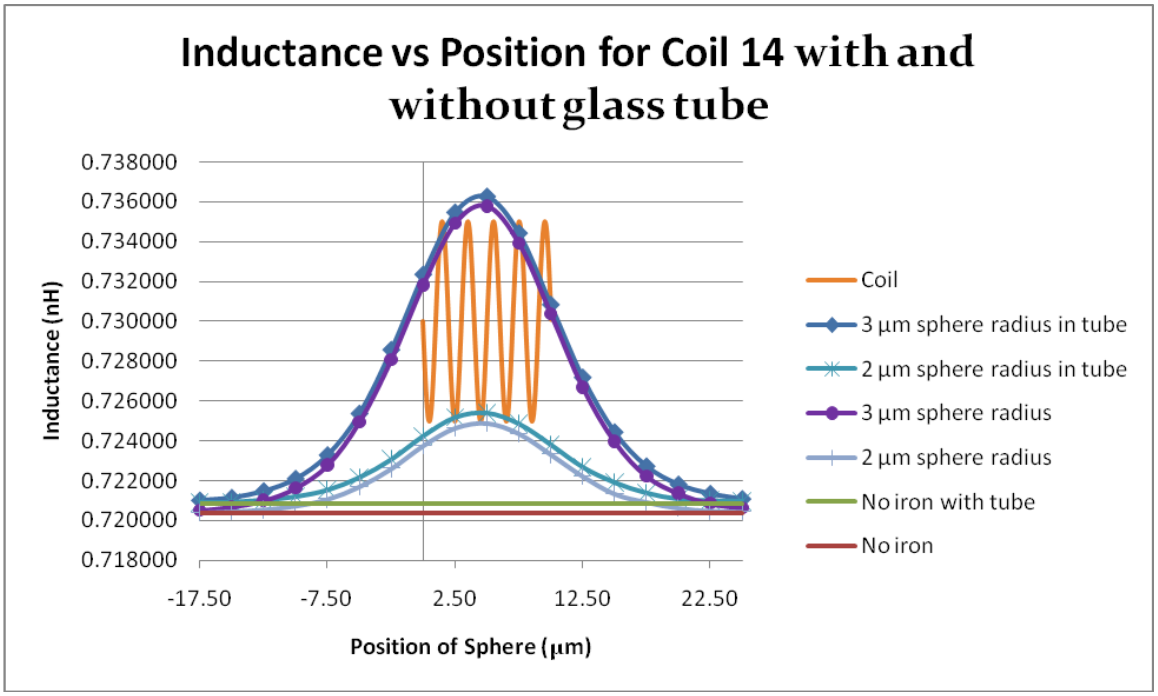

Figure 52: Simulation results for coil with glass tube inside. The sinusoid represents the relative position of the coil.

As expected, the glass tube had no significant impact on the inductance values. The values for all simulations did experience a slight increase when the tube was present. By looking at the percentage change in inductance when the glass tube is introduced, we see that there is an overall shift of about 0.07%

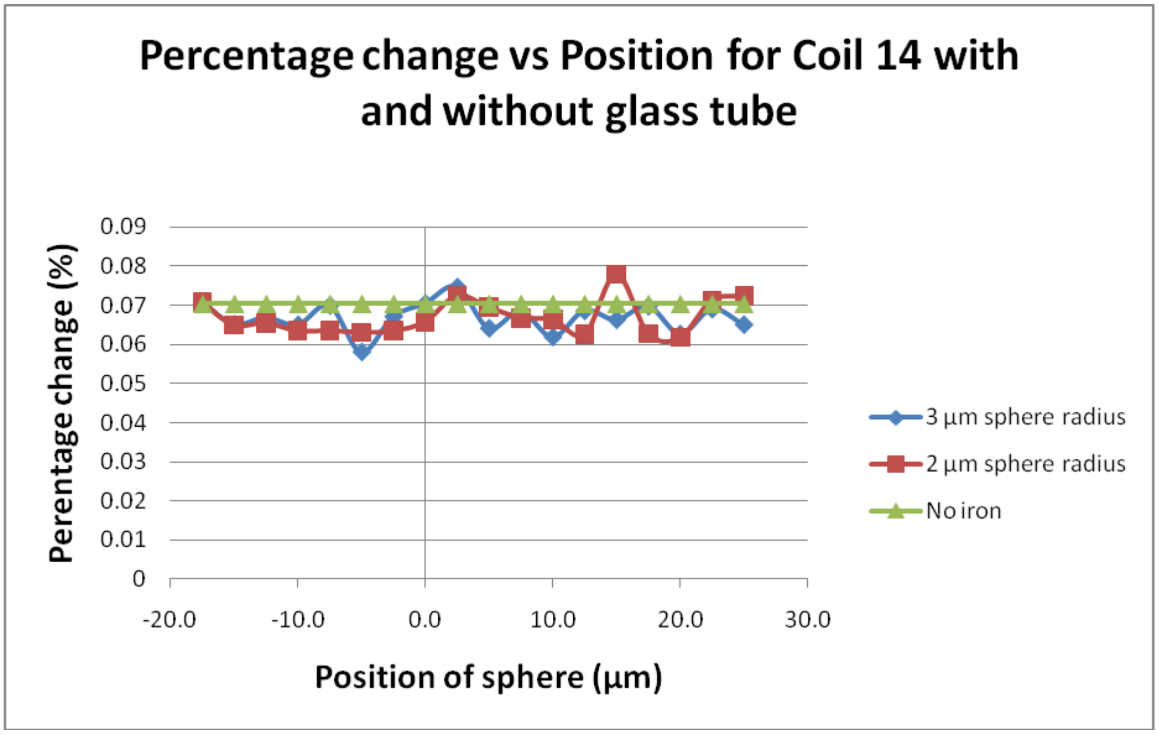

Figure 53: Comparison of the inductance change when a glass tube is inserted inside the coil.

Because this shift in inductance is minimal and relatively uniform for all simulations when the tube is present, we can safely conclude that the presence of a glass tube inside of the coil will not negatively affect the coil's detection capability.

3.3 Minimum detectable number of particles

If we could construct a coil like Coil 15, and operate it under ideal conditions, we could detect a spherical particle with a radius of 0.5 µm. The iron nano-particles that are used for tagging can be in the range of 5-65 nm in diameter [8,9]. In order to make a direct comparison to earlier work, we will assume the iron nano-particle diameter size to be 15 nm. To determine how many 15 nm iron particles this represents, we must divide the volume of the sphere by the volume of an iron nano particle.

$$particles = \frac{V_{sphere}}{V_{nano\ particle}} \tag{5}$$

For a 0.5 µm radius sphere, the volume is 5.24×10^{8} nm^{3}, and the volume for a 15 nm diameter nano particle is 1.77×10^{3} nm^{3}. The resulting number of particles is 2.96×10^{5}.

4: COIL FABRICATION FEASIBILITY STUDY

There are two primary concerns with fabricating a test coil. The first is building the coil itself at such a small scale. The second is creating a microfluidic channel that passes through the coil. We considered two different techniques for constructing a coil.

Building a coil at this scale is far more complex than winding wire around a tube. Consequently, we had to consider a coil design that was no longer cylindrical. With an idea of fabricating a coil using surface micromachining, we created a new coil model, shown in figure 54.

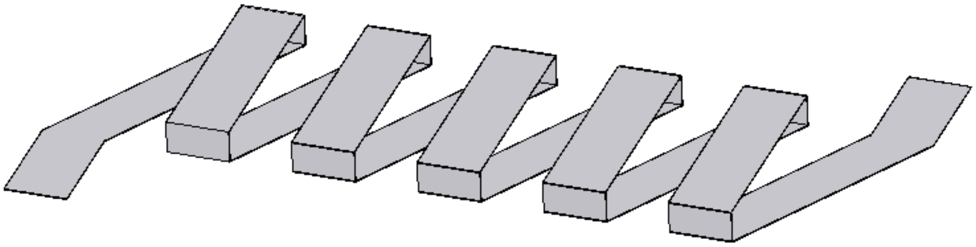

Figure 54: 3D model used for possible fabricated coil design

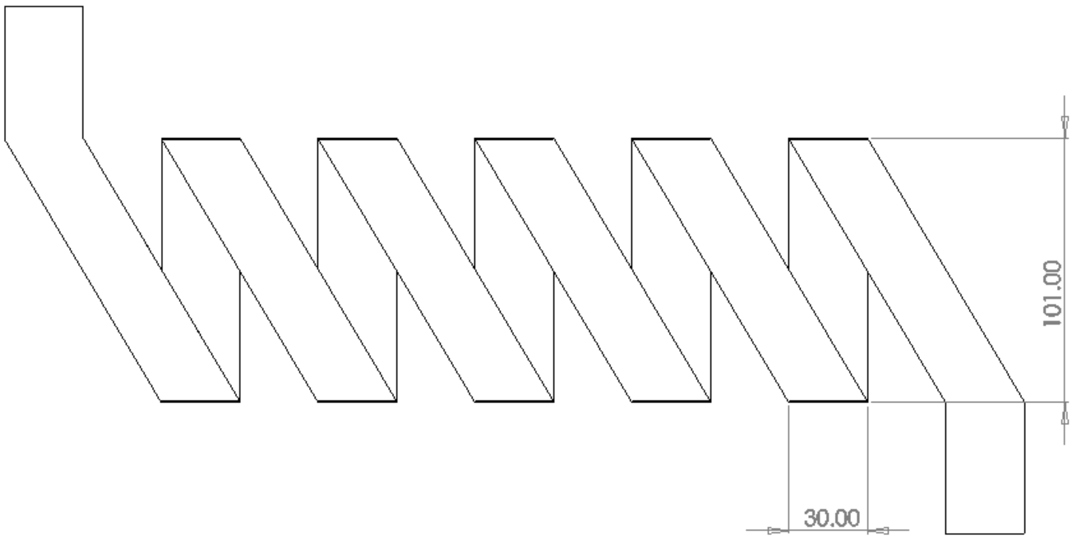

Figure 55: Top view of coil, showing dimensions. Dimensions are in μm. The height of the coil is 15 μm.

This model was simulated like the previous coils to determine if this new design would be plausible. The results of the simulations are shown in the following figure:

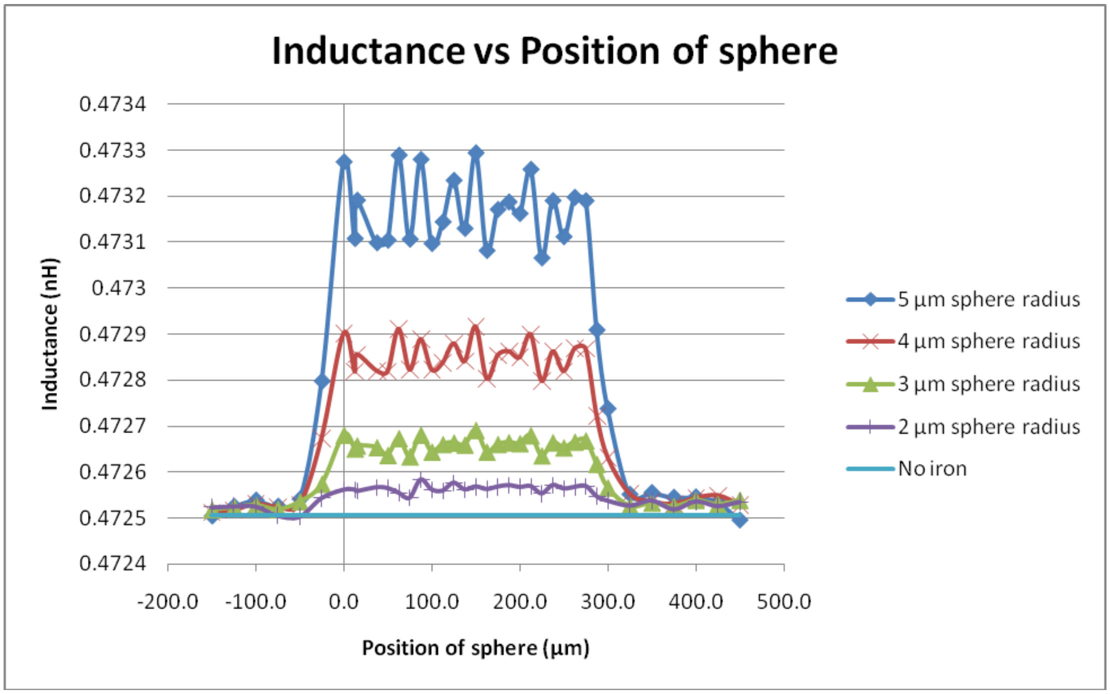

Figure 56: Simulation results for possible fabricated coil design.

Contrary to the cylindrical coils, there is an immediate jump in inductance when the iron sphere enters this new coil design, and then the inductance stays within 0.1% of this increased value until the sphere leaves the coil, at which point it immediately drops down.

The first technique we examined, to build such a coil, was to etch a channel in poly(methyl methacrylate) (PMMA), then add aluminium for the bottom part of the coil, and then bond another piece of PMMA with the rest of the coil attached to it. The aluminium would then be anodized to provide electrical isolation from any fluid passing through the coil. The problem with this method is that the bonding process would require precise alignment in order to complete the coil. Using standard bonding techniques would not allow for anything but alignment by eye, which does not provide the necessary precision. In order to solve this problem, the idea of extending the coil out to larger pads was considered, so that the pads could be aligned by eye and ensuring connectivity between the two layers of the coil. However, this idea still left the high possibility that the two halves of the coil would not be on top of each other, and thus there would be no actual coil for the liquid to pass through. Instead, we considered a different idea.

The second idea was to build a coil using SU-8 with a section of insulated channel with gold around it. SU-8 is a negative photoresist that provides near vertical sidewalls, and is widely used in microelectromechanical systems (MEMS) [10]. A piece of plastic would then be bonded on top to cover the channel. The advantage of this method over the previous one was that the coil design no longer depended on the bonding alignment. For this reason, the second method of coil design was pursued. Aluminum could be used instead of gold, but there was the possibility that the photoresist developer could attack the aluminium; therefore, to avoid this possibility, gold was used.

4.1 Fabrication steps

This section provides a brief outline of the process used for fabricating the coil, including an overview of each fabrication technique employed. A detailed recipe of the process is included in Appendix B.

4.1.1 Sputtering

Sputtering is a method of depositing a thin layer of metal on a wafer. Materials such as gold, aluminium, titanium, or chromium can be placed on a wafer in this way. According to [11], if the materials are conductive, a DC power source can be used, whereas, if the materials are dielectrics, an RF power source must be used. The power source energizes ions that collide with atoms at the target surface, which frees them up. The target acts like a cathode, and the wafers are placed on an anode so that the metal atoms are transported to the wafer.

4.1.2 Spin coating

Spin coating is used to coat our wafer in a layer of photoresist for patterning the metal, as well as coating the wafer in SU-8. The procedure for spin coating is to centre a wafer on a chuck, and then pour a liquid onto the middle of the wafer. The spin speed and spin time are then chosen to obtain the desired thickness for the particular material being used. Spin coating works best when the surface of the wafer is planar.

4.1.3 Exposure and development

The exposure step is where we determine which part of our photoresist we want to keep, and which part we want to develop away. For a positive photoresist, the areas that are exposed to ultra violet light will be removed when the wafer is developed, while the opposite is true for a negative photoresist [11]. We select which areas we want to keep by putting a mask between the wafer and the exposure source. The exposure time is set based on the thickness and type of photoresist being used.

4.1.4 Etching

There are two types of etching that we used in our process. The first is wet etching, where we place the wafer in a liquid that will attack the material we want to remove faster than it attacks other materials on our wafer. In this manner, the material protected by photoresist will remain, while the rest of it is removed. This wet etching process will normally occur equally in all directions. In addition to etching away the material we want to remove, it will also undercut our protective layer and remove some of the material we want to keep [11]. Consequently, we must make sure not to etch for longer than necessary, or else we will lose our pattern.

The second etching process we used is reactive-ion etching (RIE). As described in [11], RIE only etches in one direction, which removes the undercutting problem found with wet etching. The process uses reactive gases ionized by plasma to bombard the surface of the wafer. In our lab, wet etching is much faster to do than RIE, and, in most cases, the undercutting issue is not significant enough to worry about. There are also some cases where etching equally in all directions is desired. For the reasons mentioned, we use wet etching most of the time.

4.1.5 Soft bake

Soft baking was used to evaporate solvent from the photoresist [11], and in the case of SU-8, make the film denser [10]. A convection oven or a hot plate can be used for this process. We used a convection oven for our metal patterning photoresist, and a hot plate for our SU-8 layers.

4.1.6 Process

The process begins with a clean Pyrex wafer that was sputtered with a 10 nm layer of chromium and a 100 nm layer of gold. The chromium was used because the gold will not bond to the Pyrex on its own. Next, we spun photoresist onto the metal layer and expose the wafer using the first mask. Then we developed it to remove the unwanted photoresist. A gold etchant and then chromium etchant are used to remove the excess metal, and finally the rest of the photoresist is removed. The following figure shows a representation of the wafer after these first steps:

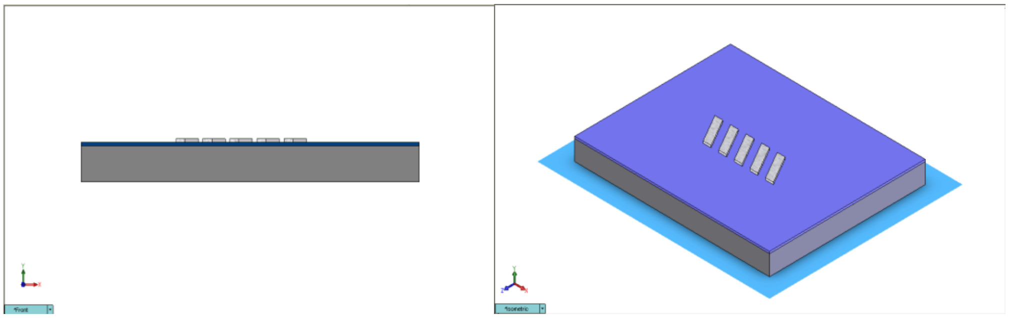

Figure 57: Cross-sectional view (left) and isometric view (right) of wafer after patterning the bottom metal layer.

Next, we spun a thin layer of SU-8 onto the wafer, and then we exposed it with the second mask. This mask patterns holes to make contact with the metal layer. We developed the SU-8, and then did a brief RIE to improve adhesion with the next layer of SU-8. After the RIE, a thicker layer of SU-8 was spun on and then the channel, reservoirs, and support structures are patterned using the third mask.

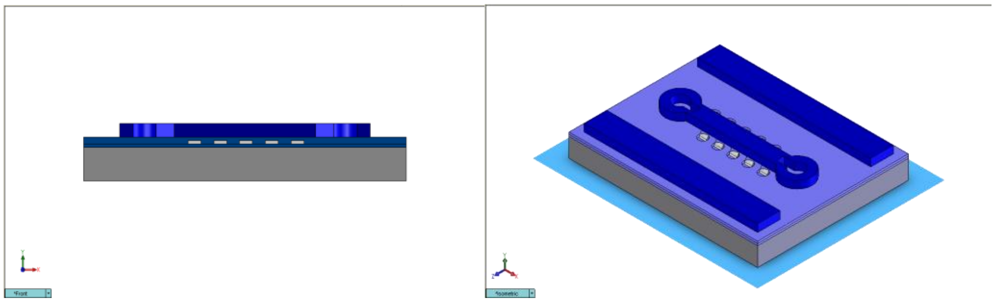

Figure 58: Cross-sectional view (left) and isometric view (right) of wafer after patterning the second layer of SU-8.

In order to make the channel go through the coil, but keep the metal insulated, a thin strip down the centre of the channel was lightly exposed with the fourth mask. By doing this light exposure, only a thin layer of the SU-8 becomes cross linked, and the rest was washed away in developer, resulting in an enclosed channel running directly through the coil.

Again, chromium and gold were sputtered and photoresist was spun on. The top half of the coil was patterned using the fifth mask, and then the photoresist was developed and the gold and chromium were etched away. At this point, the coil structure was complete, as can be seen in the following figure:

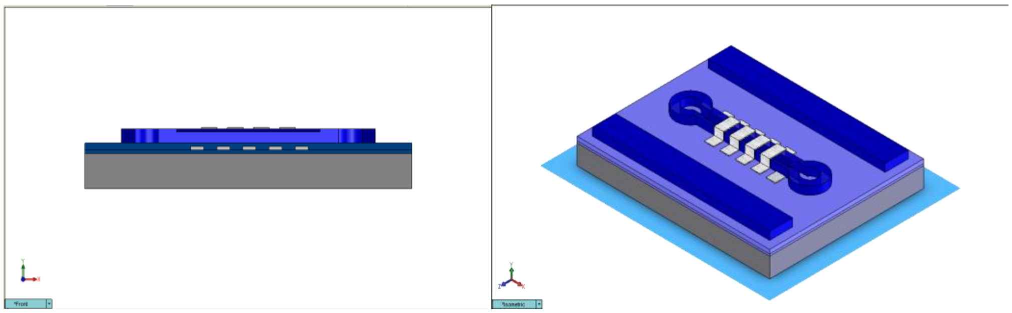

Figure 59: Cross-sectional view (left) and isometric view (right) of wafer after patterning the second metal layer.

Finally, a plastic wafer was used to cap the rest of the channel, and provide access to the reservoirs and electrical connections to the coil. The holes were put into the plastic wafer and then aligned by eye when it is bonded.

Devices with three different channel widths were fabricated: 60 um, 100 um, and 150 um. The next section deals with the testing of these devices and comparisons to simulated results.

4.2 Fabrication results

When creating the masks for the above process, we decided to make a slight alteration to the coil design. Instead of having the bottom part of the coil run diagonally from one side to the other, we changed it to run in parallel to the top of the coil, and stagger the lines so that there would be minimal capacitance between the two layers. We were hoping to see a smaller capacitive change when passing a fluid through the coil than what we saw in our earlier experiment. To see if this new design would still be feasible, we simulated a coil of this design.

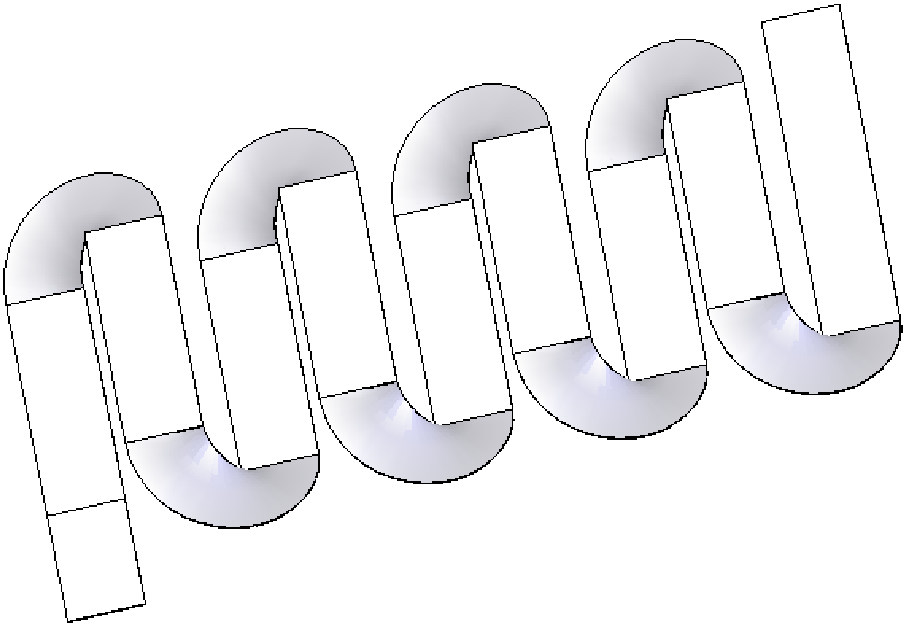

Figure 60: 3D model used to represent the coil from the fabrication design. Half-helixes are used for the sides to eliminate sharp edges in the simulation, and reduce the time needed to calculate a solution.

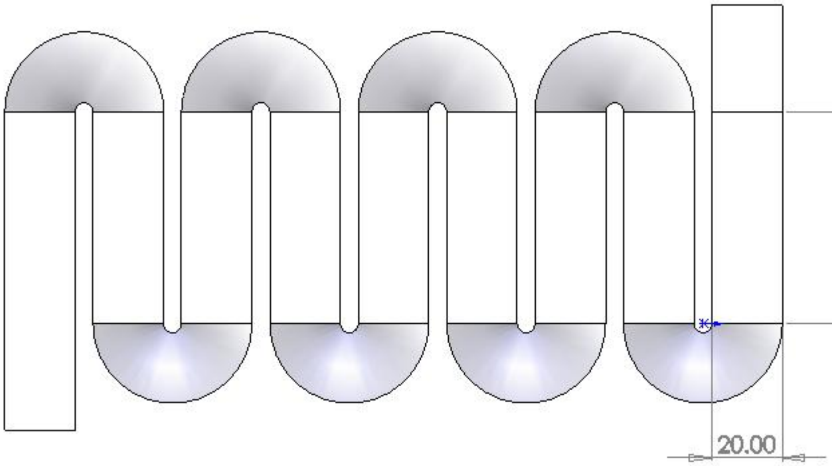

Figure 61: Top view of coil, showing dimensions. Dimensions are in μm. The height of the coil is 30 μm.

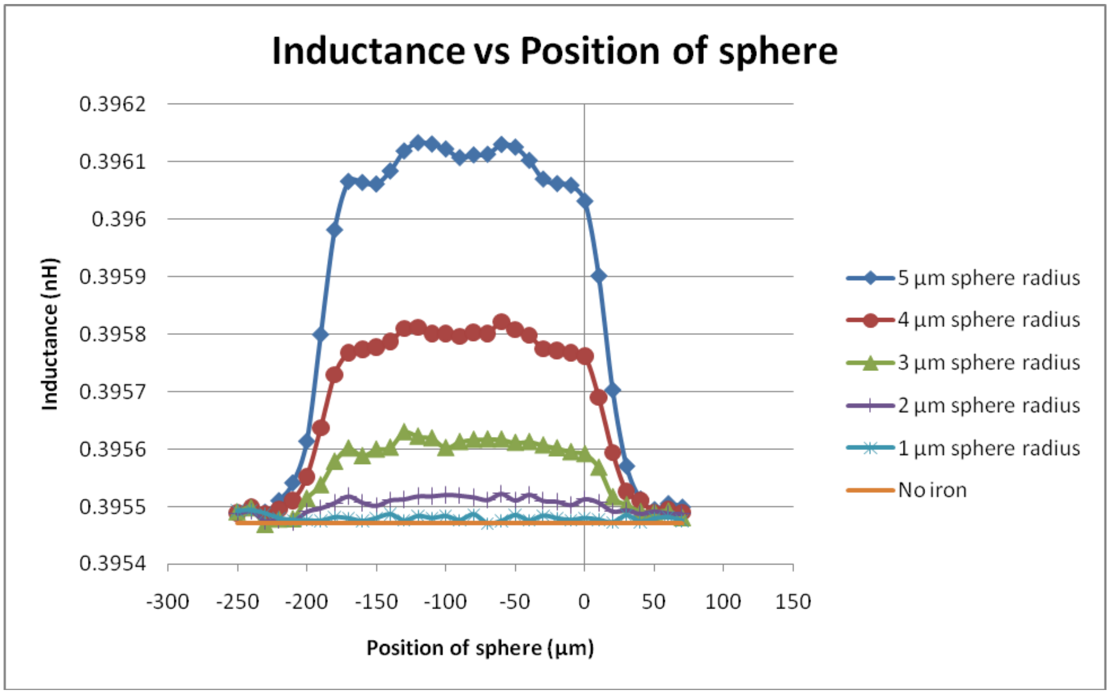

Figure 62: Simulation results for coil representing our fabrication design.

While fabricating the coils, we encountered several problems along the way. In the first attempt, we noticed that the second layer of SU-8 was pulling away from the first layer around the edge of the wafer, resulting in a bulge that could negatively impact the patterning of the SU-8. To rectify this problem, we did a brief RIE on the first layer of SU-8 to roughen up the surface and improve adhesion from the second layer. While this step did alleviate the first problem, it ended up causing a new one. Originally, we developed both layers of SU-8 in one-step. However, when we developed the SU-8 after completing the RIE, we noticed that the contact holes had not fully developed. We suspect that the energy from the RIE was causing some of the SU-8 to crosslink, and, therefore, not develop. This second problem was solved by adding a second SU-8 development step before the RIE.

When developing the second layer of SU-8, we had to be very careful not to cause too much stress on the SU-8 bridges that formed the top of the channel. Too much agitation, pouring liquids directly onto the wafer, or drying the wafer with the nitrogen gun from too close could all cause the SU-8 bridges to break, rendering that coil unusable.

The final, and most significant problem that we encountered was while spinning the photoresist onto the second metal layer. Because the surface of the wafer was covered in topology from the second SU-8 layer, we could not spin a uniform coating of photoresist. The sides of the channel facing the centre of the wafer collected a thicker coating of photoresist than the sides facing the outer edge. The photoresist also did not form a continuous line around the corner between the top and side of the channel. We experimented with different thicknesses of photoresist to try and solve this problem, but when the photoresist was thick enough to fully cover the corner, there was too thick of a layer over the contacts that would create a short along the side of the coil if it was not removed. A technique of using multiple thin layers of photoresist and patterning them each time to build up the top corners without leaving extra photoresist on the bottoms showed promise, but more refinement is need to fabricate a working coil.

We did not continue the fabrication process past this point, but are confident that with more refinement, this process will lead to working coils.

5: CONCLUSION AND FUTURE WORK

5.1 Future work

There is still a lot of work that needs to be undertaken on this project before we will have a device that can detect ferromagnetically tagged bio-molecules by way of a change in inductance. The fabrication process still needs some refinement in order to produce working coils, and then tests need to be performed on both the coil and the channel. An oscillator circuit needs to be built using one of these coils, and experiments need to be performed with iron particles to determine how sensitive the design is, and how well it performs in the presence of noise. A better technique for introducing the iron particles into the coil also needs to be developed, possibly using a dispersant to keep the particles in suspension. Another circuit needs to be built that can detect the shift in frequency so that the device can function without needing an oscilloscope. Improvements need to be made to improve the sensitivity, and everything needs to be condensed into one conveniently sized package.

5.2 Contribution

This project reports, to the best of our knowledge, the first time a systematic simulation of a micro-coil has been performed to observe the effect of inductance due to a traversing micro-particle. The inductance profile has been studied for both axial and radial movement of particles, as well as particle distribution. A fabrication process has been proposed that explains how to construct a micro-coil around a microfluidic channel. This thesis can serve as an introductory platform for launching a more detailed analysis and eventual fabrication process that can build a ferromagnetically tagged bio-molecule detector.

5.3 Conclusion

This thesis shows the viability of using a coil to detect iron nano-particles for the purpose of detecting bio-molecules. We performed an experiment using a coil wrapped around a tube to examine the possibility of using the change in frequency of an oscillator to signify the presence of iron particles inside of the coil. The results of this experiment showed that the idea was plausible, and we set out to design a more effective coil to act as the sensor.

In order to find out what kind of coil design yields the best sensitivity for the detection of ferromagnetic nano particles, we used Comsol and SolidWorks to build and simulate a collection of different coil designs. We observed the effect that frequency had on the inductance of the coils, and then examined the behaviour of the coils with iron spheres located at different positions inside the coils.

The most effective coil design we simulated was a 25 μm diameter coil with a length of 0.02 mm and made of 10 turns. Optimistically, this coil could detect as few as $3\text{x}10^5$ particles. The drawbacks to such a coil design are that the inductance is very low and it will be a challenge to build a circuit that can differentiate such small inductance changes from noise in the circuit.

We came up with a process to build a coil on the scale of the ones we simulated, that also had a micro channel running through it so that we could push through samples of fluid with iron suspended in them. We simulated a coil of this design, and found that it should be able to detect 1.89×10^{7} particles. While the process still needs some refinement before working coils can be produced, the work presented in this thesis shows that the idea has merit. With more time spent overcoming the problems we encountered, we are confident that this process will yield working coils.

APPENDICES

Appendix A – Calculations

Dimensions for equivalent volume cube

$$V_{Sphere} = \frac{4\pi r^3}{3} = \frac{4\pi(5\mu m)^3}{3} = 524\mu m^3$$

To find the side length, *l*, of the equivalent volume cube, we let the cube volume equal the sphere volume and take the cube root:

$$l = \sqrt[3]{523.6\mu m^3} = 8.06\mu m$$

Minimum number of particles

For the 0.5 µm radius sphere, the volume is:

$$V_{Sphere} = \frac{4\pi r^3}{3} = \frac{4\pi(500nm)^3}{3} = 5.24x10^8 nm^3$$

For the 2 µm radius sphere, the volume is:

$$V_{Sphere} = \frac{4\pi r^3}{3} = \frac{4\pi(2000nm)^3}{3} = 3.35x10^{10} nm^3$$

For the 15 nm diameter particles, the volume is:

$$V_{Sphere} = \frac{4\pi r^3}{3} = \frac{4\pi(7.5nm)^3}{3} = 1.77x10^3 nm^3$$

Dividing the sphere volume by the nano particle volume gives the number of nano particles as 2.96×10^5 for the 0.5 µm radius sphere and 1.89×10^7 µm for the 2 radius sphere.

Appendix B – Fabrication recipe

1. Start with a clean Pyrex wafer
2. Sputter 10nm Cr and 100nm Au
3. Spin on Shipley 1813 at 3000rpm for 30 seconds
4. Softbake at 100°C for 15 minutes
5. Expose with METAL1 (light field) mask for 45 seconds
6. Develop in MF-319 for 4 minutes
7. Etch Au in Au etchant for 40 seconds
8. Etch Cr in Cr etchant for 35 seconds
9. Remove photoresist in acetone
10. Spin on SU-8 2005 at 3000rpm for 30 seconds
11. Softbake on a hotplate at 95°C for 15 minutes with ramping at 300°C/hr and then naturally cool down
12. Expose with EPAD (light field) mask for 30 seconds
13. Post-exposure-bake on a hotplate at 95°C for 15 minutes with ramping at 300°C/hr and then naturally cool down
14. Develop in SU-8 developer for 3 minutes and rinse with IPA
15. Activate in RIE for 1 minute
16. Spin on SU-8 2010 at 1000rpm for 30 seconds
17. Softbake on a hotplate at 95°C for 15 minutes with ramping at 300°C/hr and then naturally cool down
18. Expose with CHANNEL (dark field) mask for 70 seconds
19. Expose with COILTOP (dark field) mask for 9 seconds
20. Post-exposure-bake on a hotplate at 95°C for 15 minutes with ramping at 300°C/hr and then naturally cool down
21. Develop in SU-8 developer for 10 minutes and rinse with IPA
22. Sputter with 10nm Cr and 100nm Au
23. Spin on Shipley 1813 at 3000rpm for 30 seconds
24. Softbake at 100°C for 15 minutes
25. Expose with METAL2 (light field) mask for 20 seconds
26. Develop in MF-319 for 1 minute
27. Etch Au and Cr in Au etchant and then Cr etchant
28. Blanket expose photoresist for 20 seconds
29. Develop in MF-319 for 1 minute
30. Prepare a plastic wafer with holes for chamber accesses and electrical pads
31. Make sure one side is covered with tape
32. Spin on 2μm PMMA on the plastic wafer
33. Peel the tape off
34. Align and place the plastic wafer on top of the wafer with microchannels.
35. Bake it at low temperature

Appendix C – Full size images of coil simulation results

For the following figures, the left column is the magnetic flux density in T, and the second is the electric potential in V.

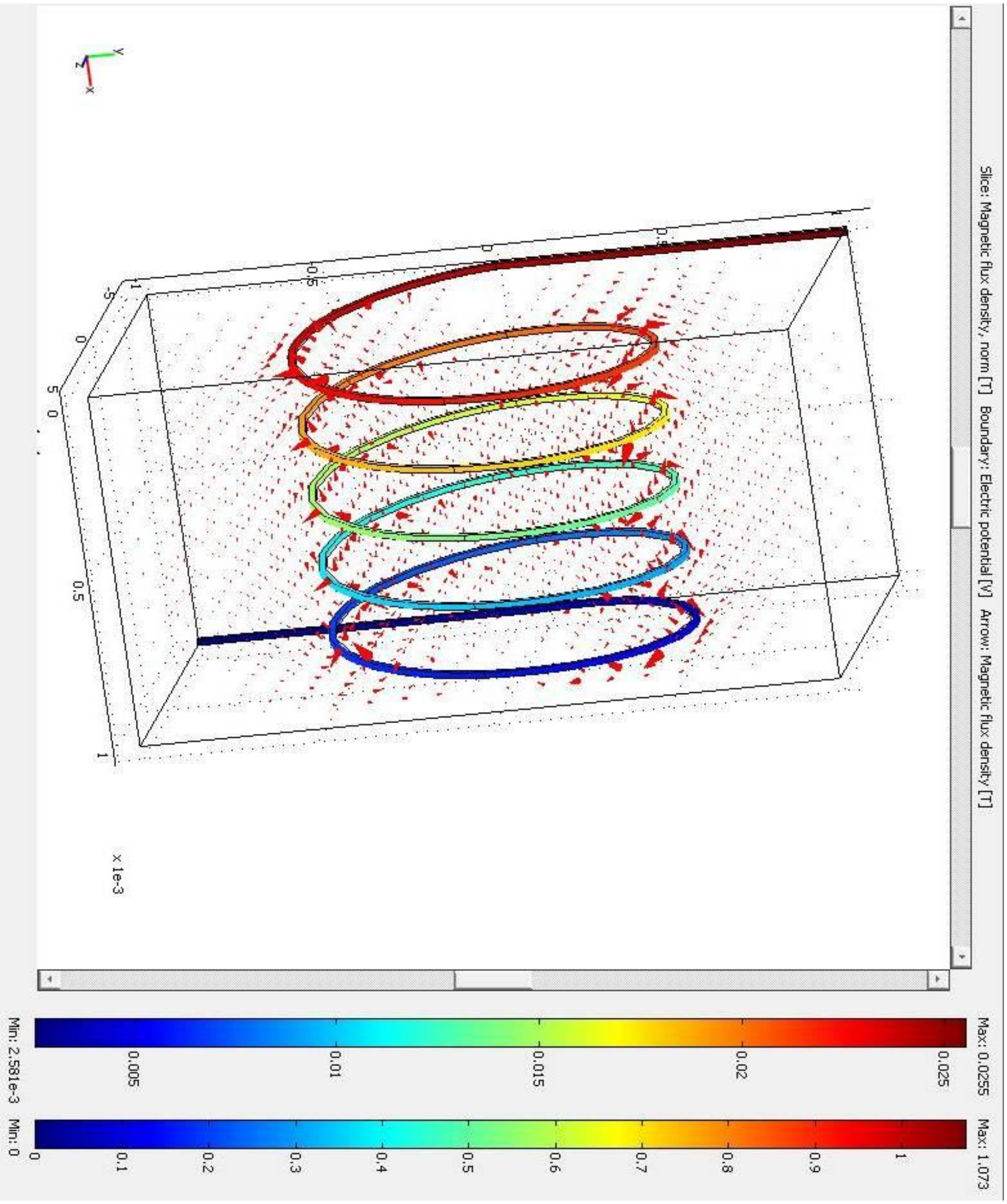

Figure C-1: Magnetic flux density and electric potential for Coil 1

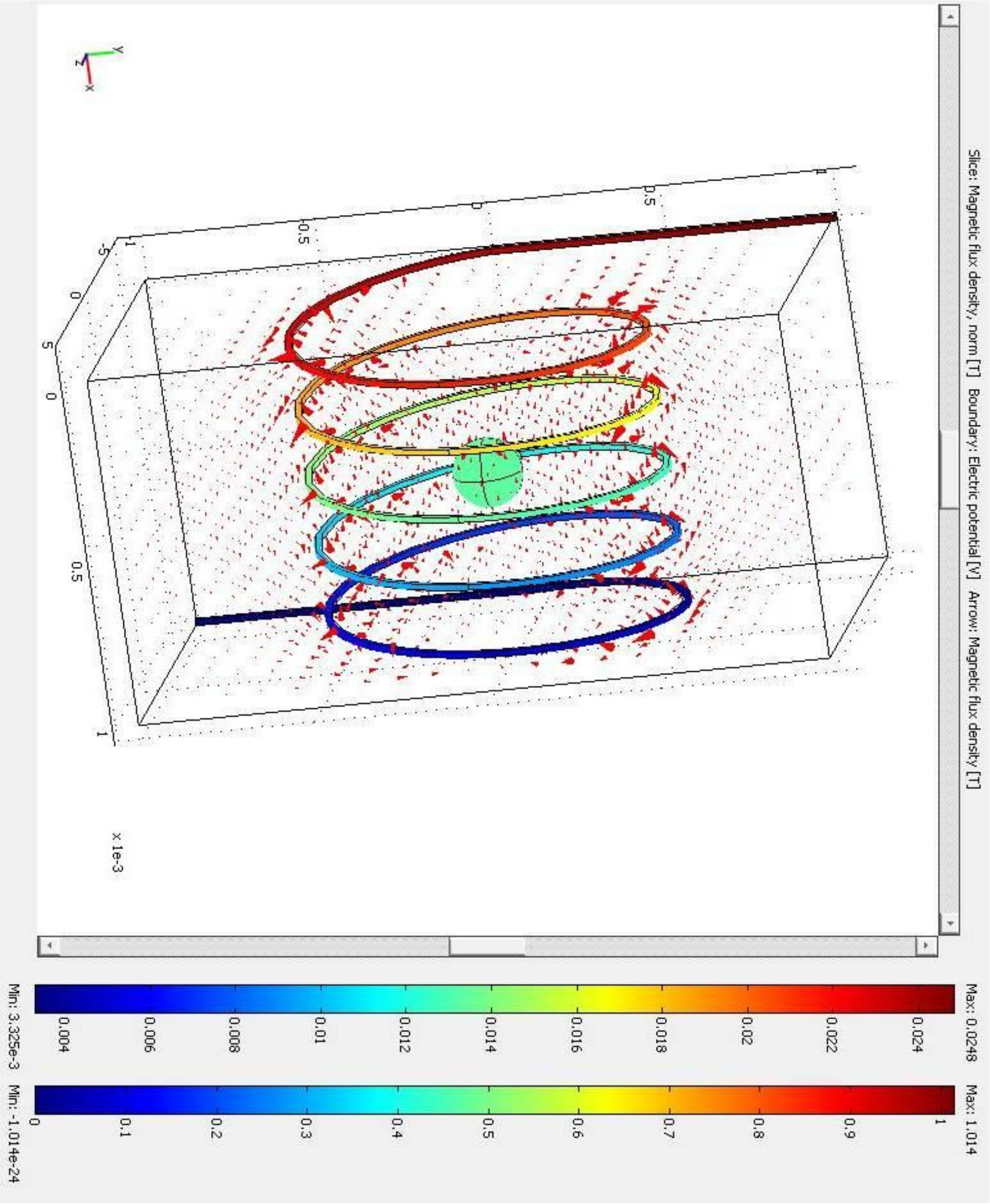

Figure C-2: Magnetic flux density and electric potential for Coil 1 with iron

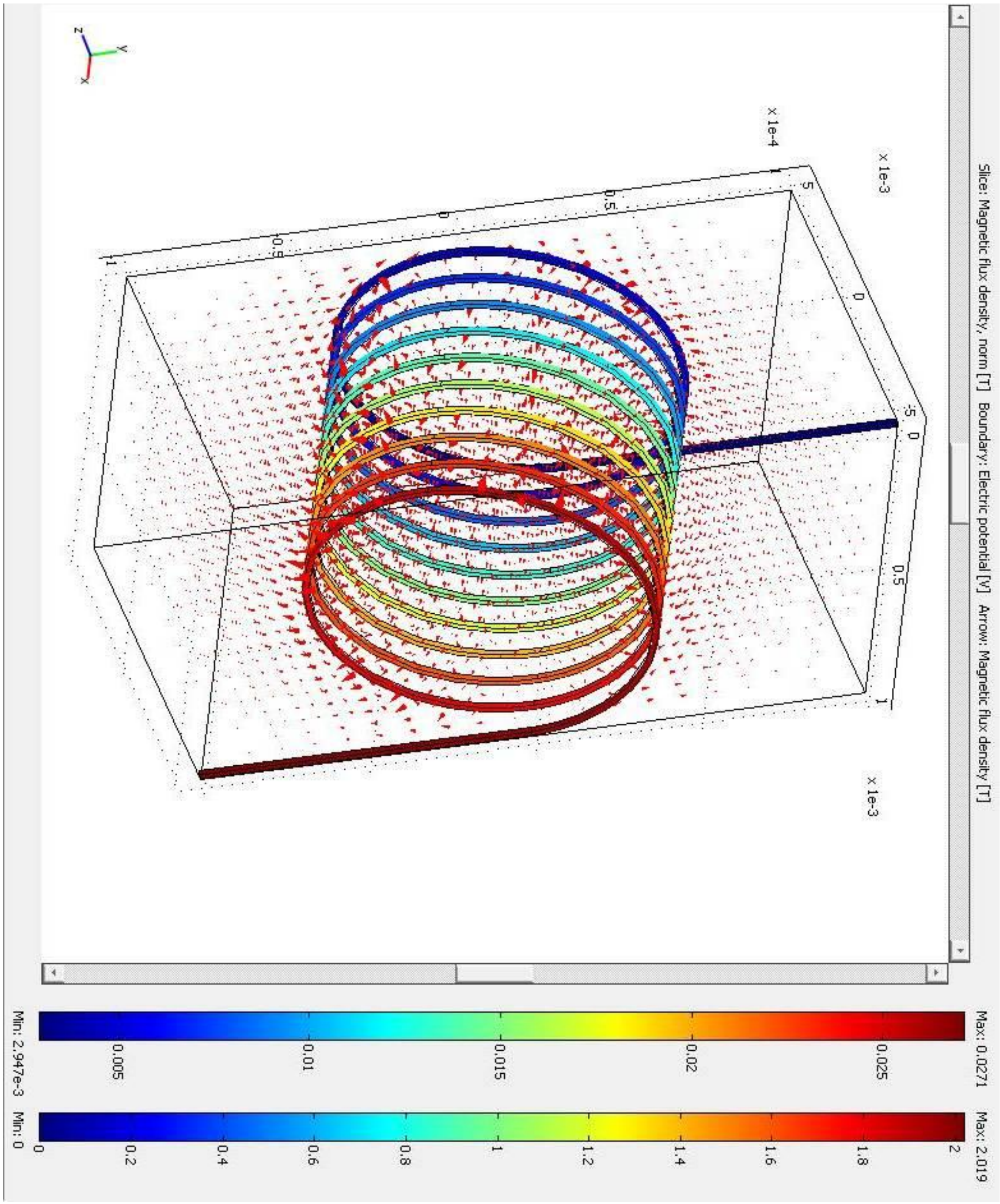

Figure C-3: Magnetic flux density and electric potential for Coil 2

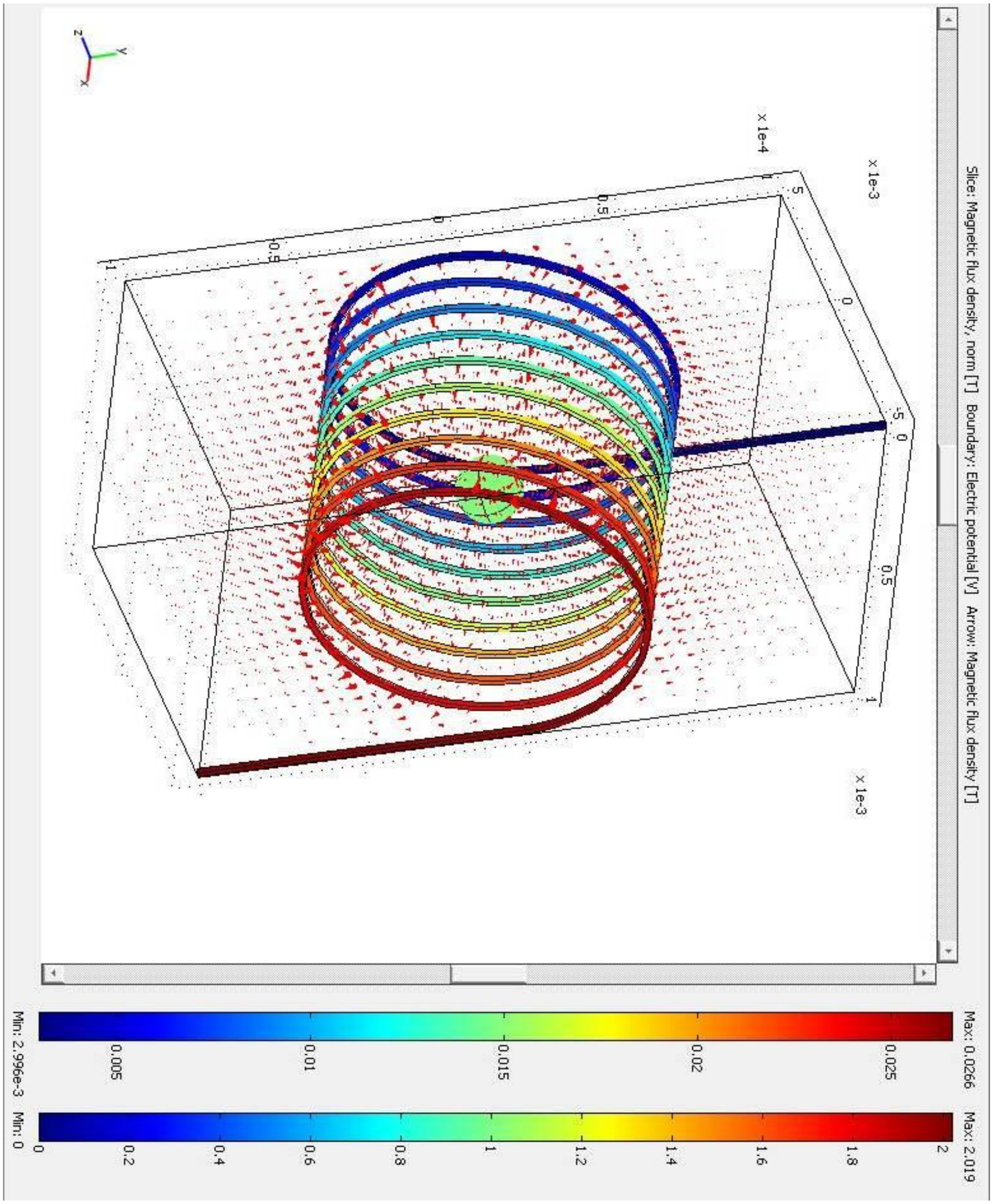

Figure C-4: Magnetic flux density and electric potential for Coil 2 with iron

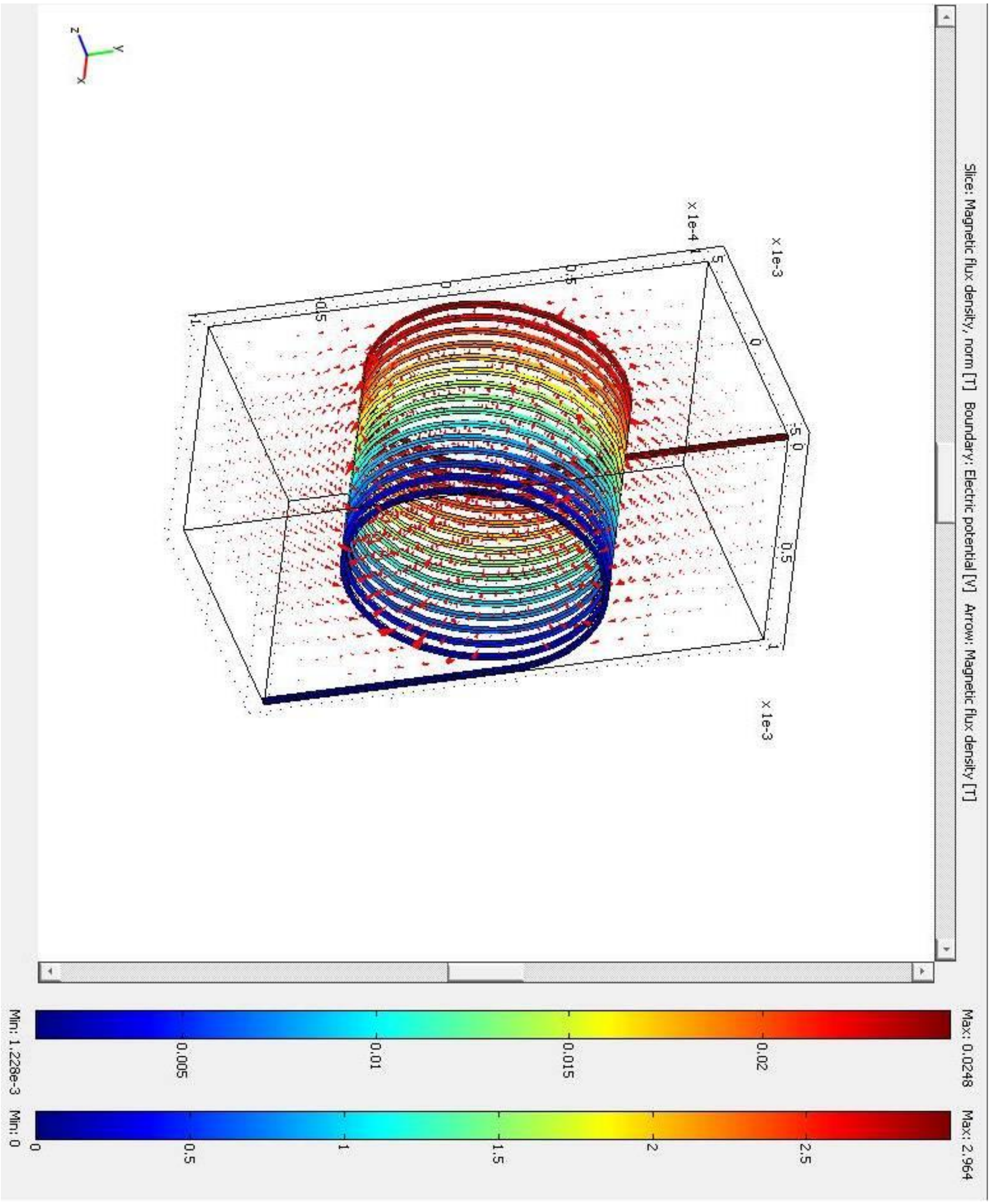

Figure C-5: Magnetic flux density and electric potential for Coil 3

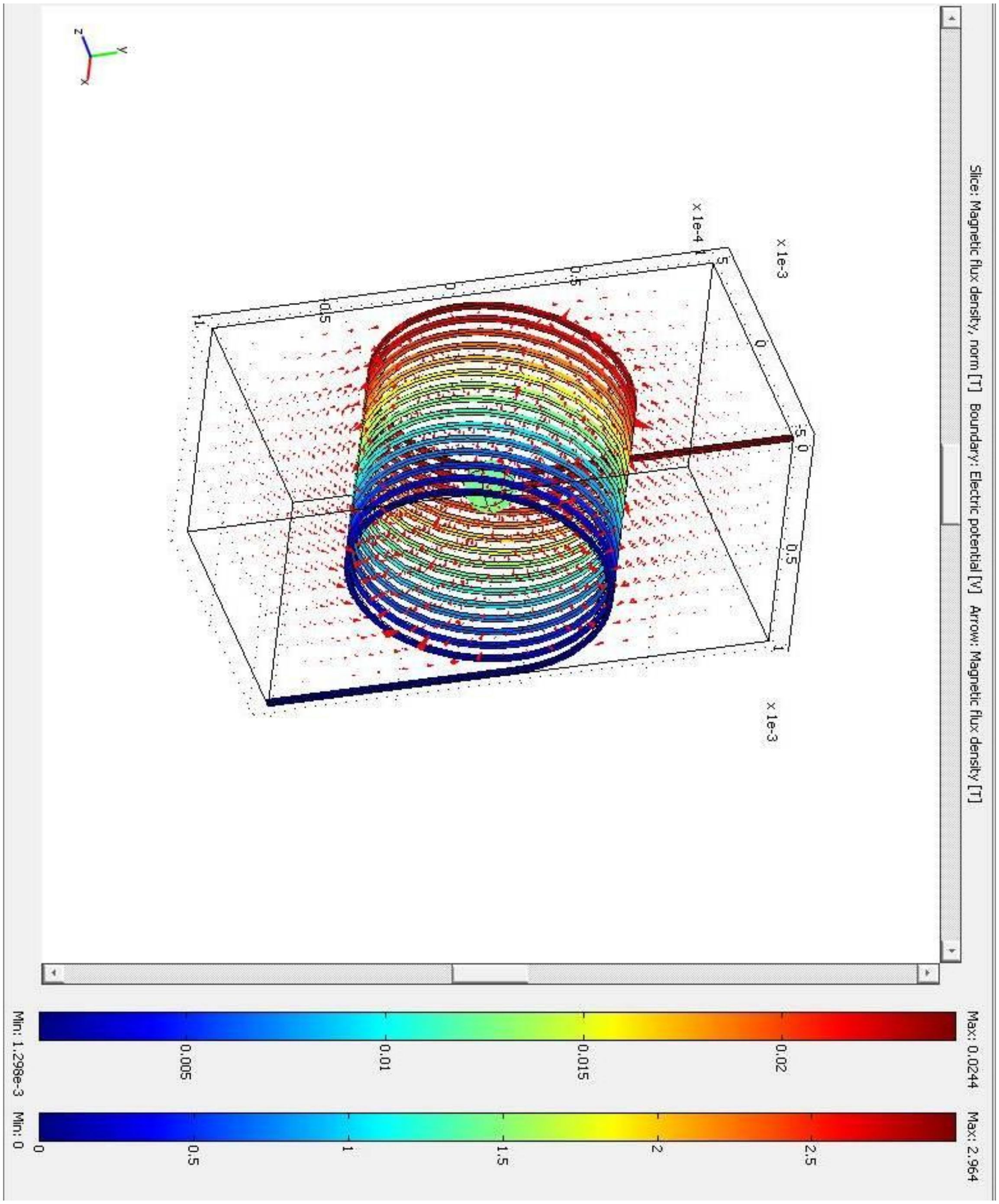

Figure C-6: Magnetic flux density and electric potential for Coil 3 with iron

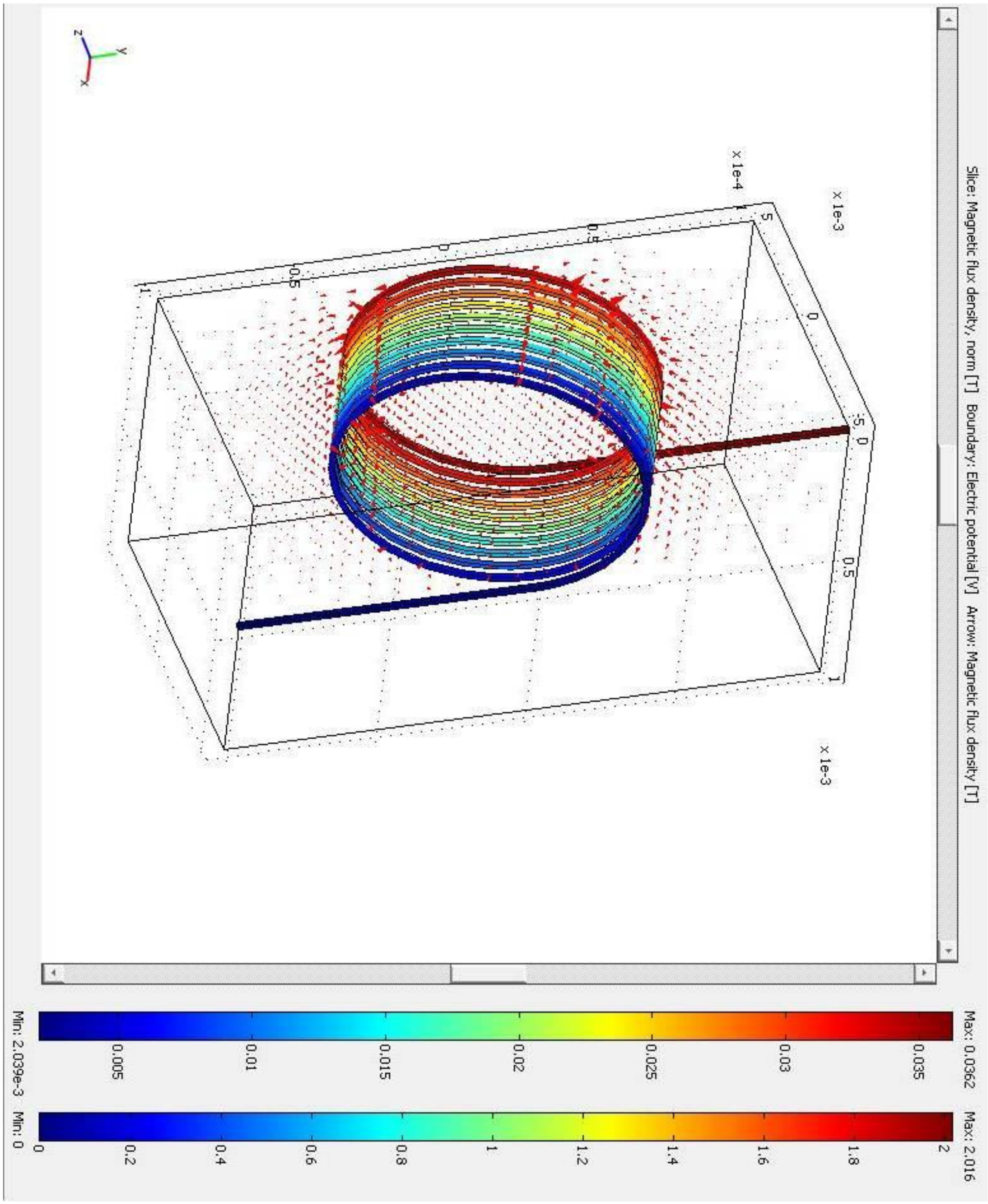

Figure C-7: Magnetic flux density and electric potential for Coil 4

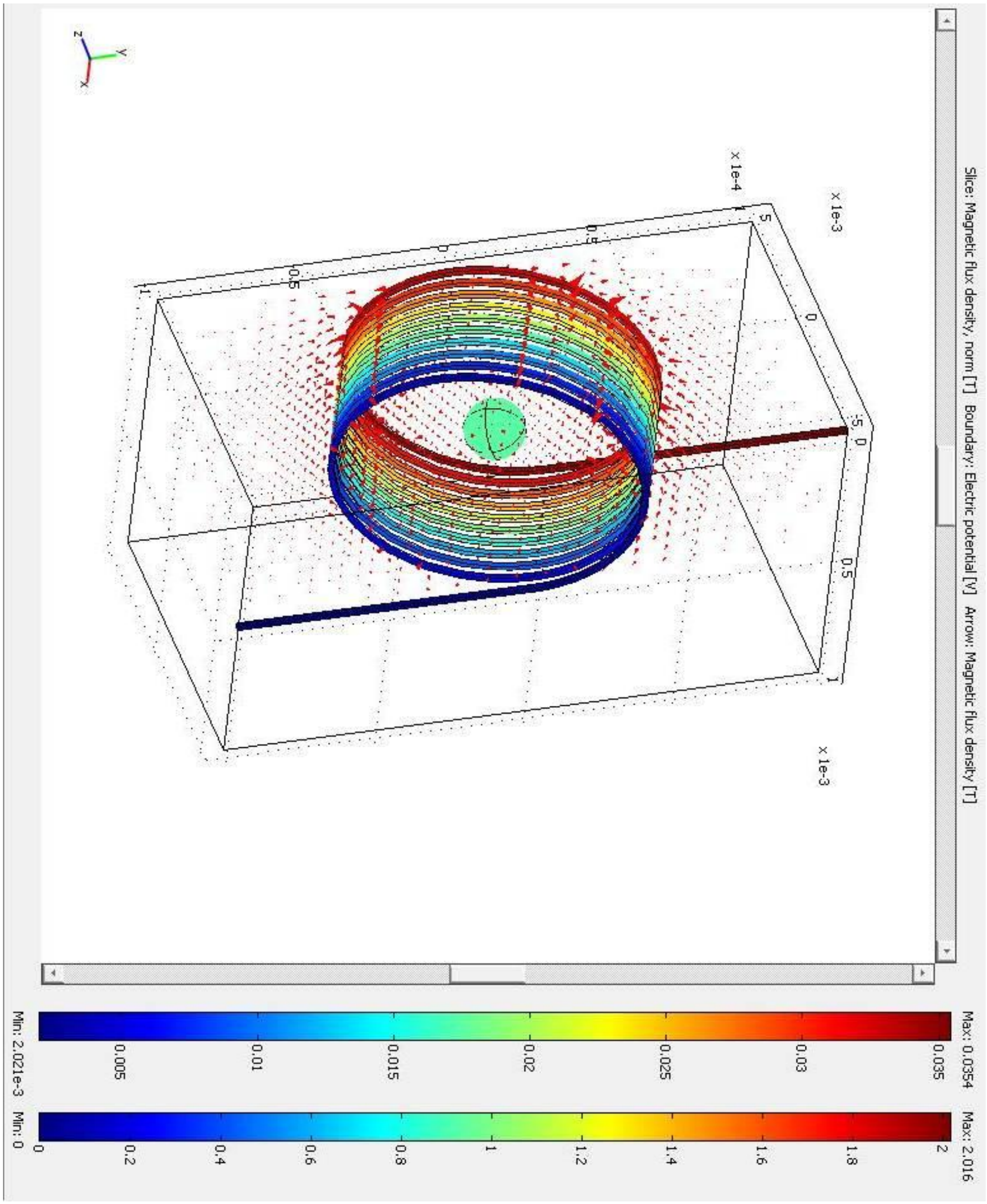

Figure C-8: Magnetic flux density and electric potential for Coil 4 with iron

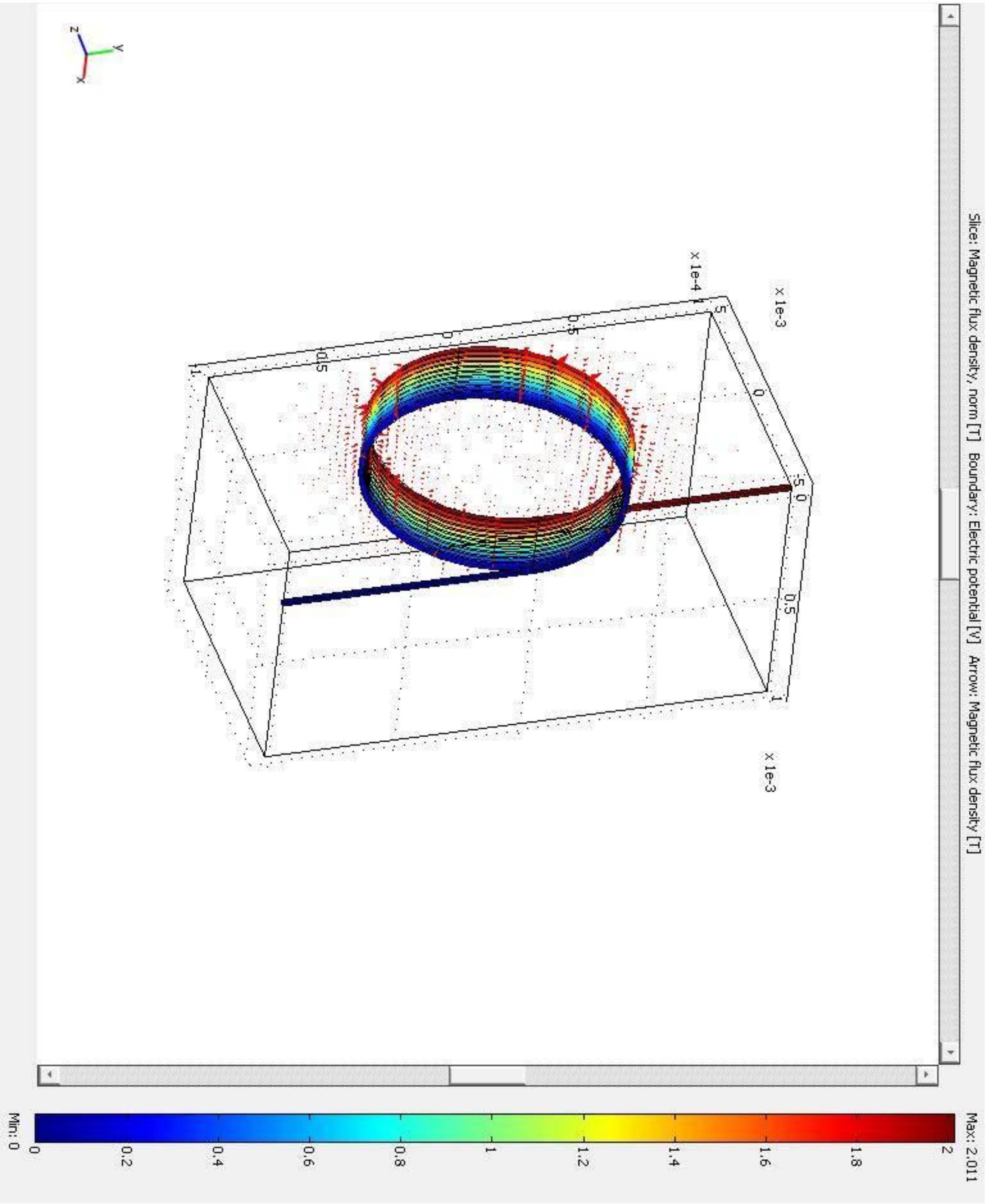

Figure C-9: Magnetic flux density and electric potential for Coil 5

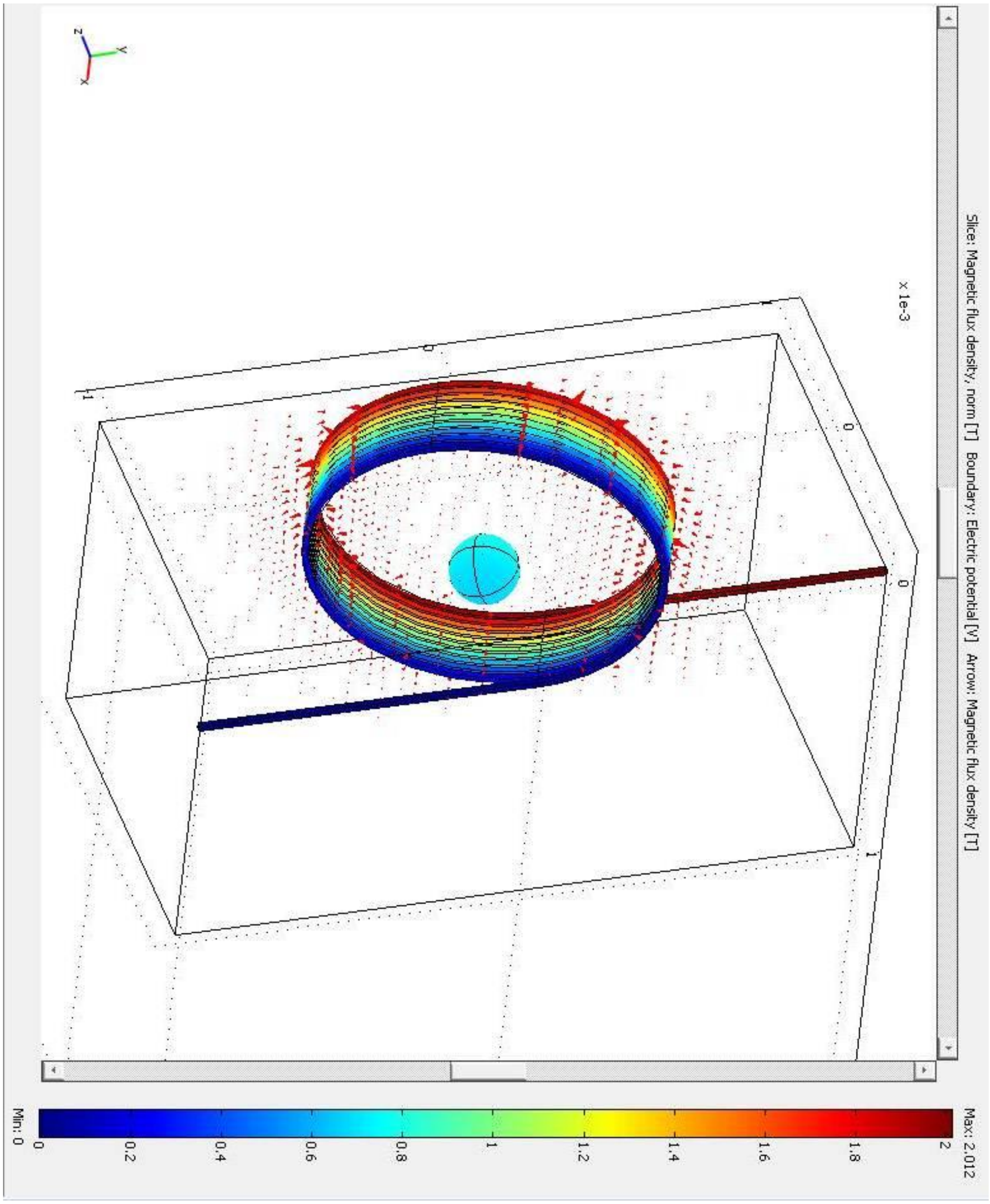

Figure C-10: Magnetic flux density and electric potential for Coil 5 with iron

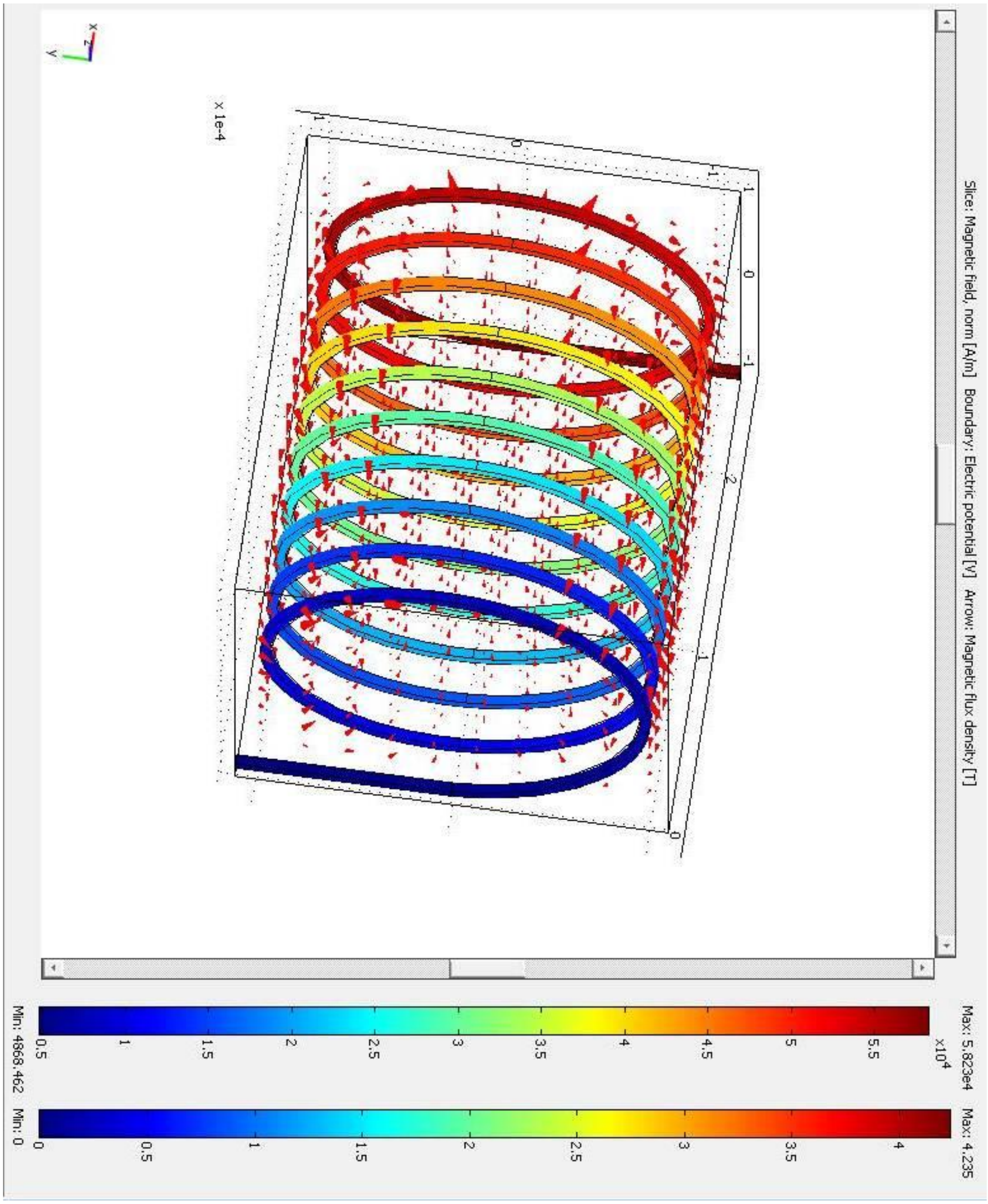

Figure C-11: Magnetic flux density and electric potential for Coil 6

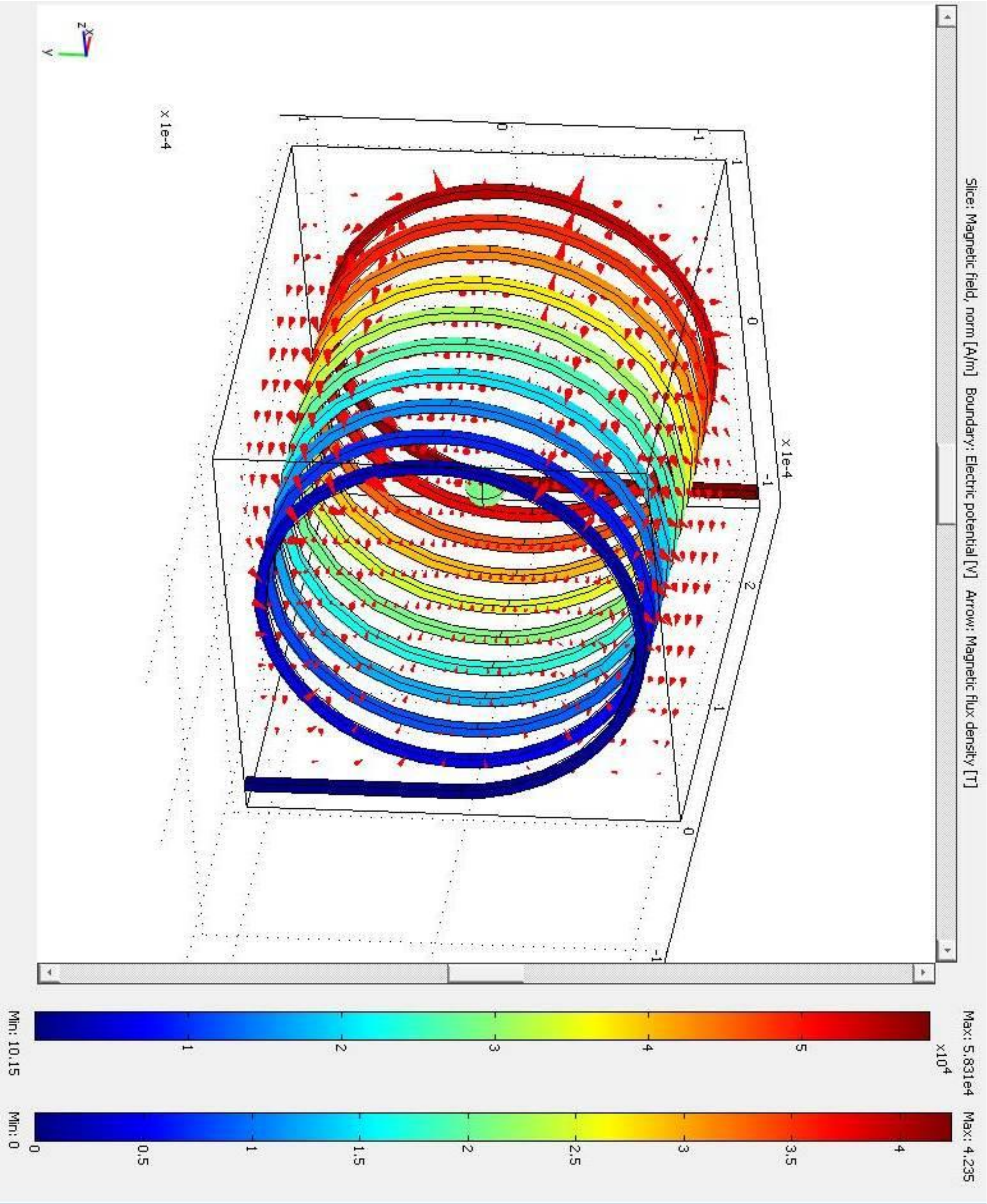

Figure C-12: Magnetic flux density and electric potential for Coil 6 with iron

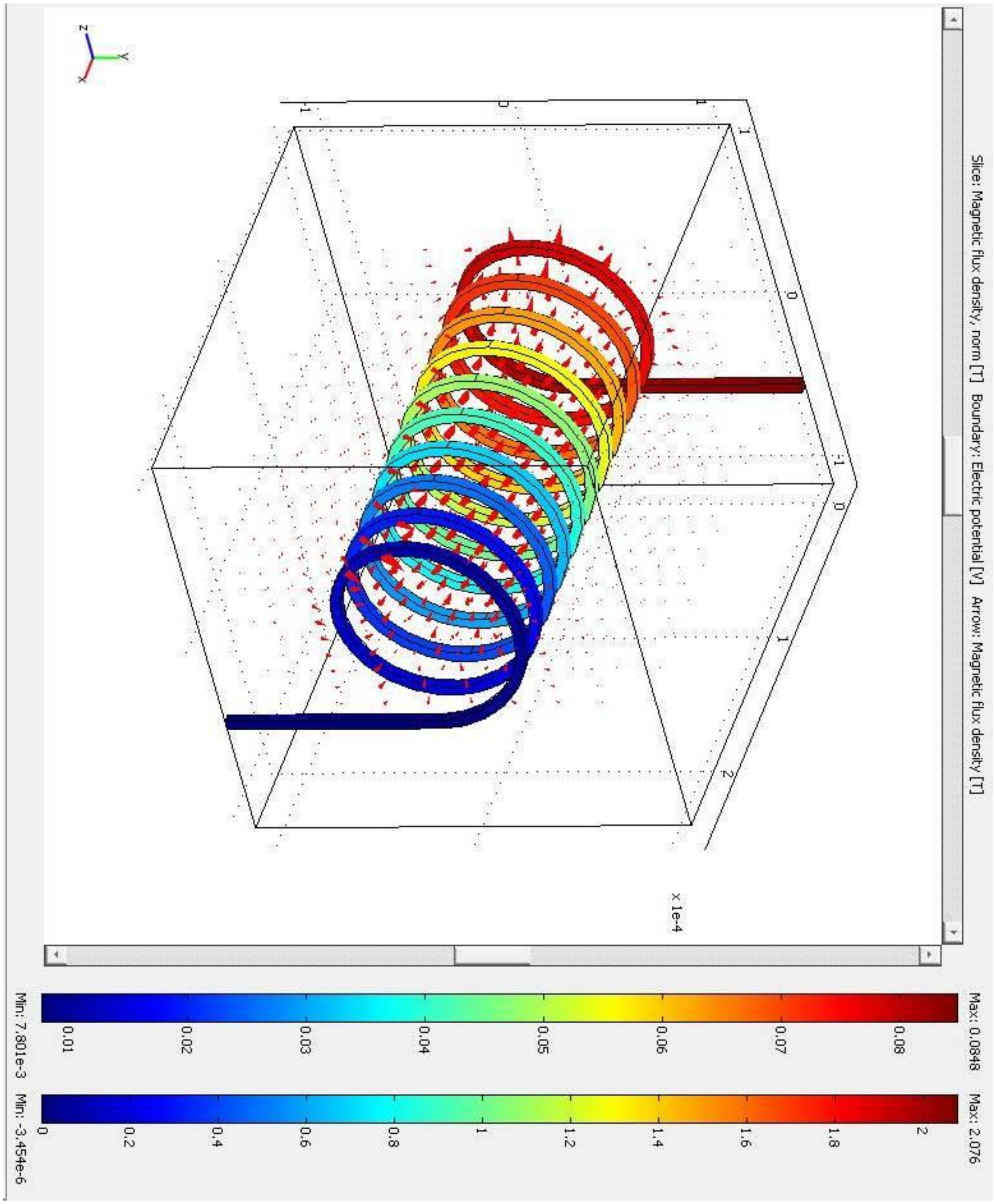

Figure C-13: Magnetic flux density and electric potential for Coil 7

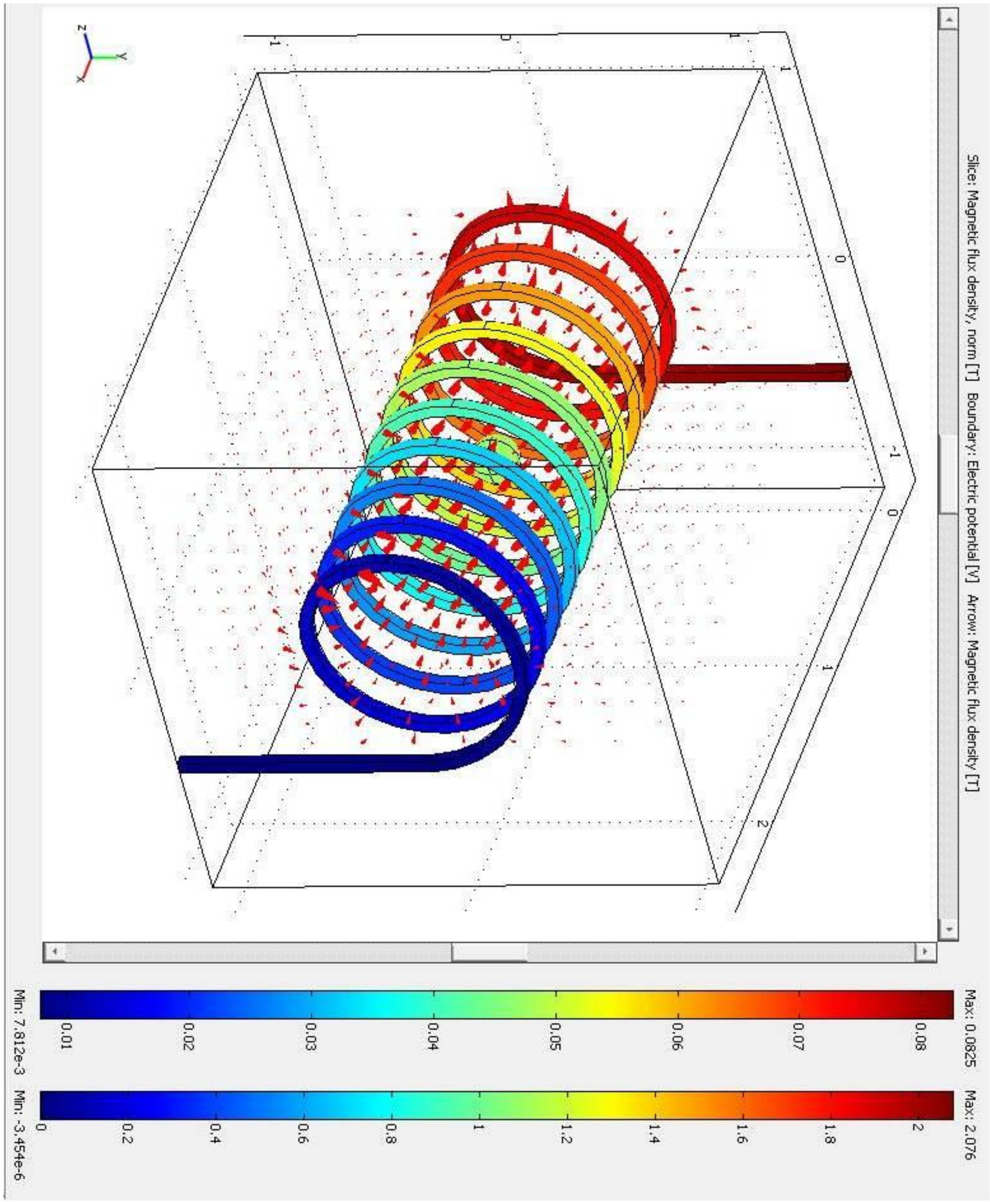

Figure C-14: Magnetic flux density and electric potential for Coil 7 with iron

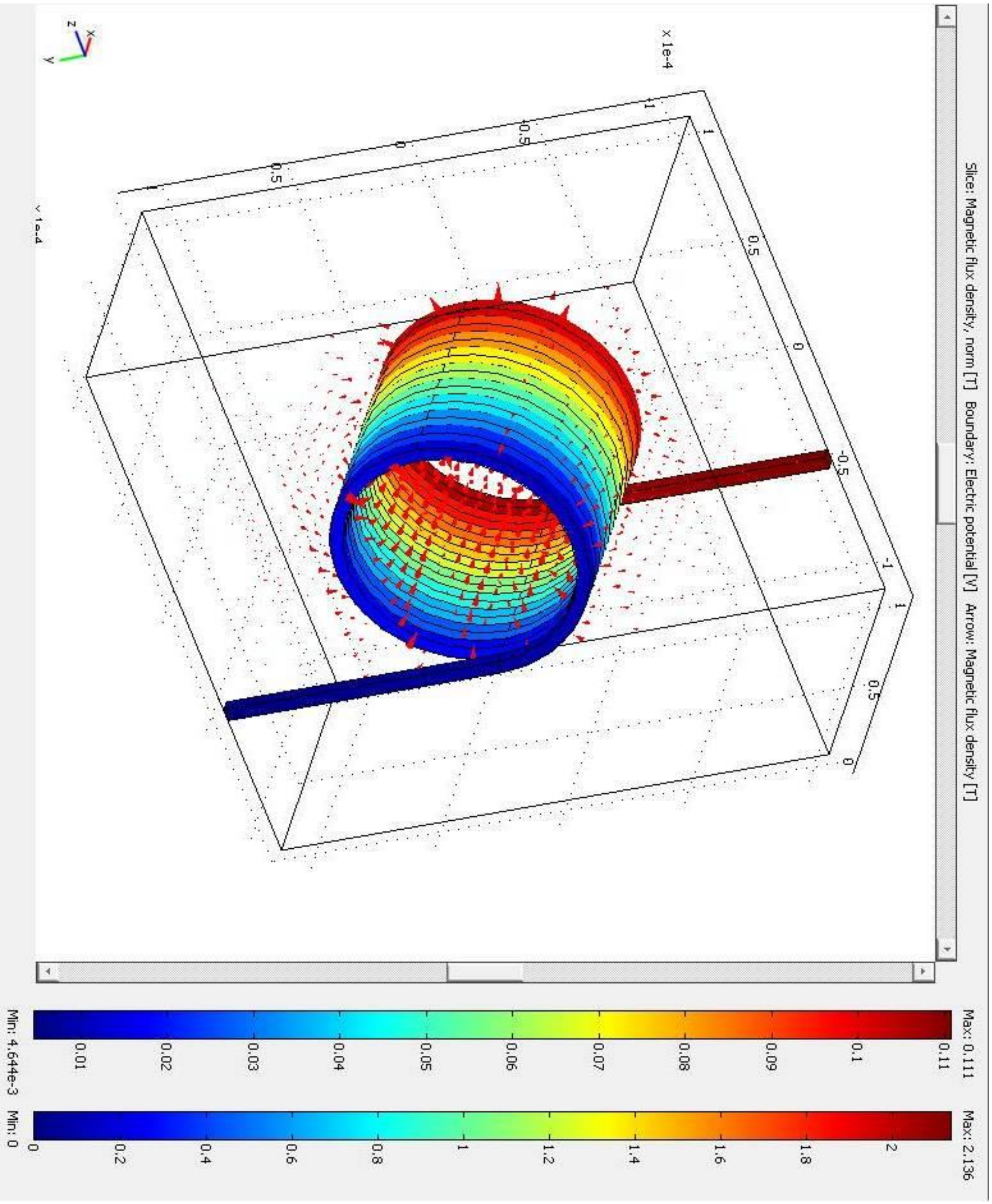

Figure C-15: Magnetic flux density and electric potential for Coil 8

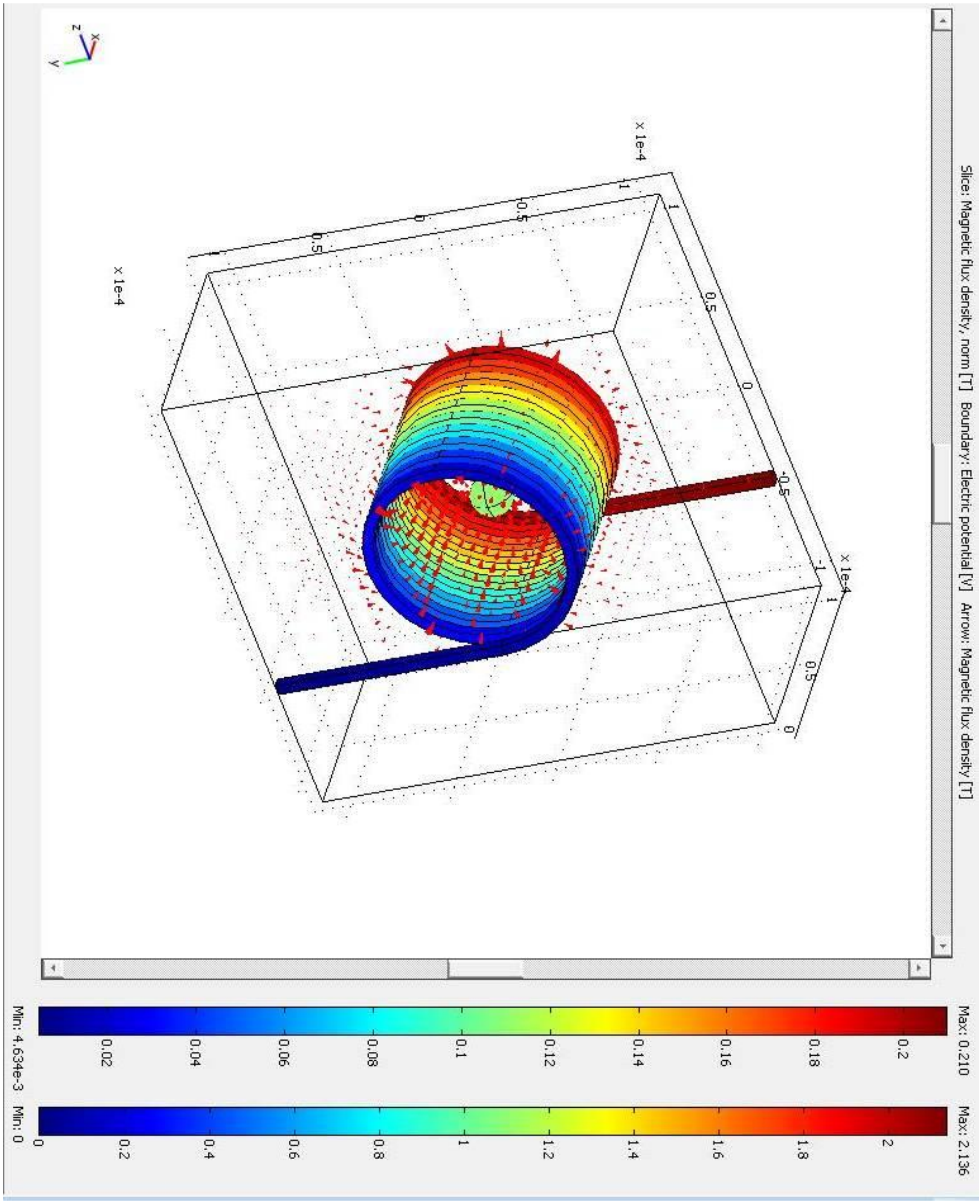

Figure C-16: Magnetic flux density and electric potential for Coil 8 with iron

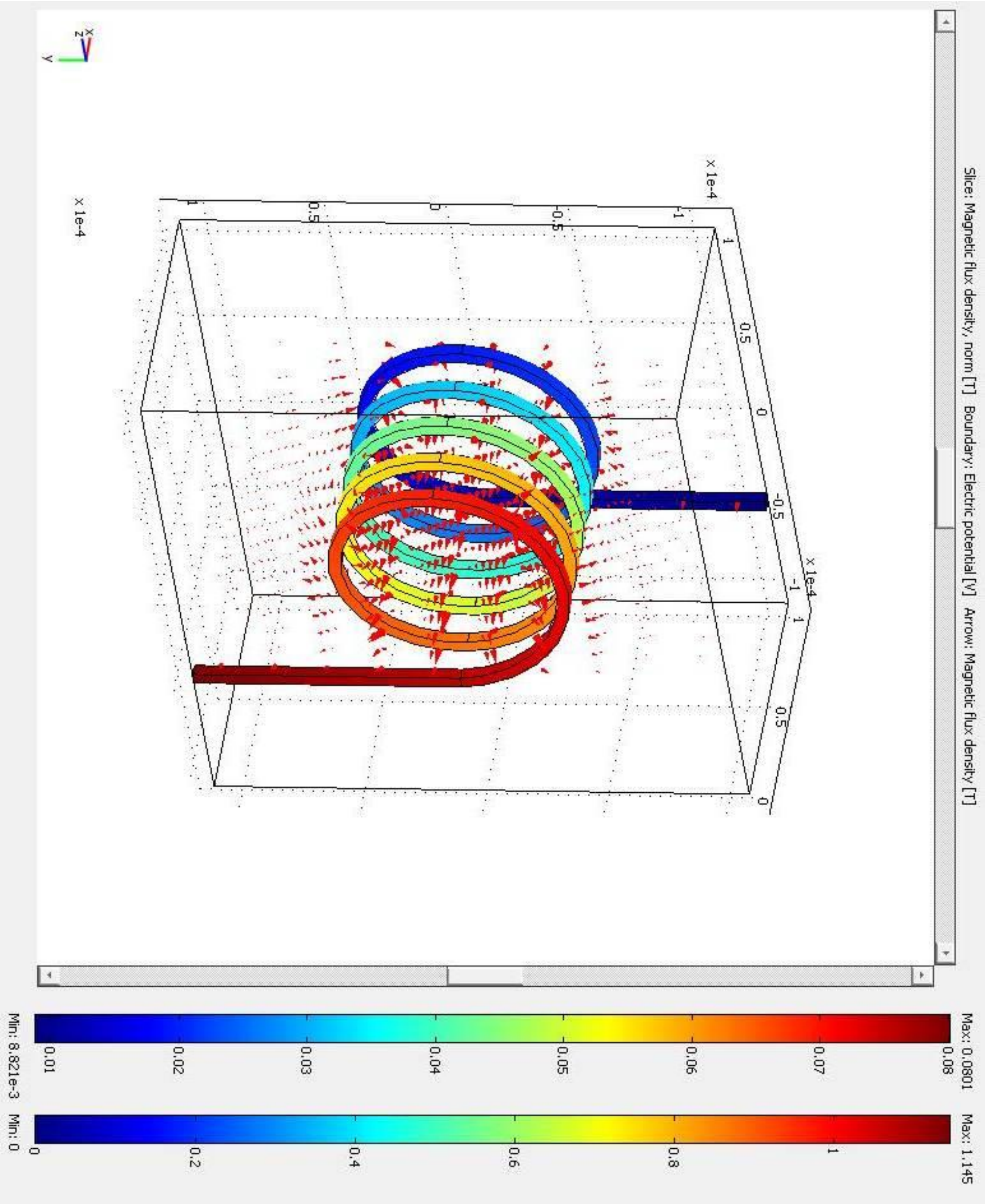

Figure C-17: Magnetic flux density and electric potential for Coil 9

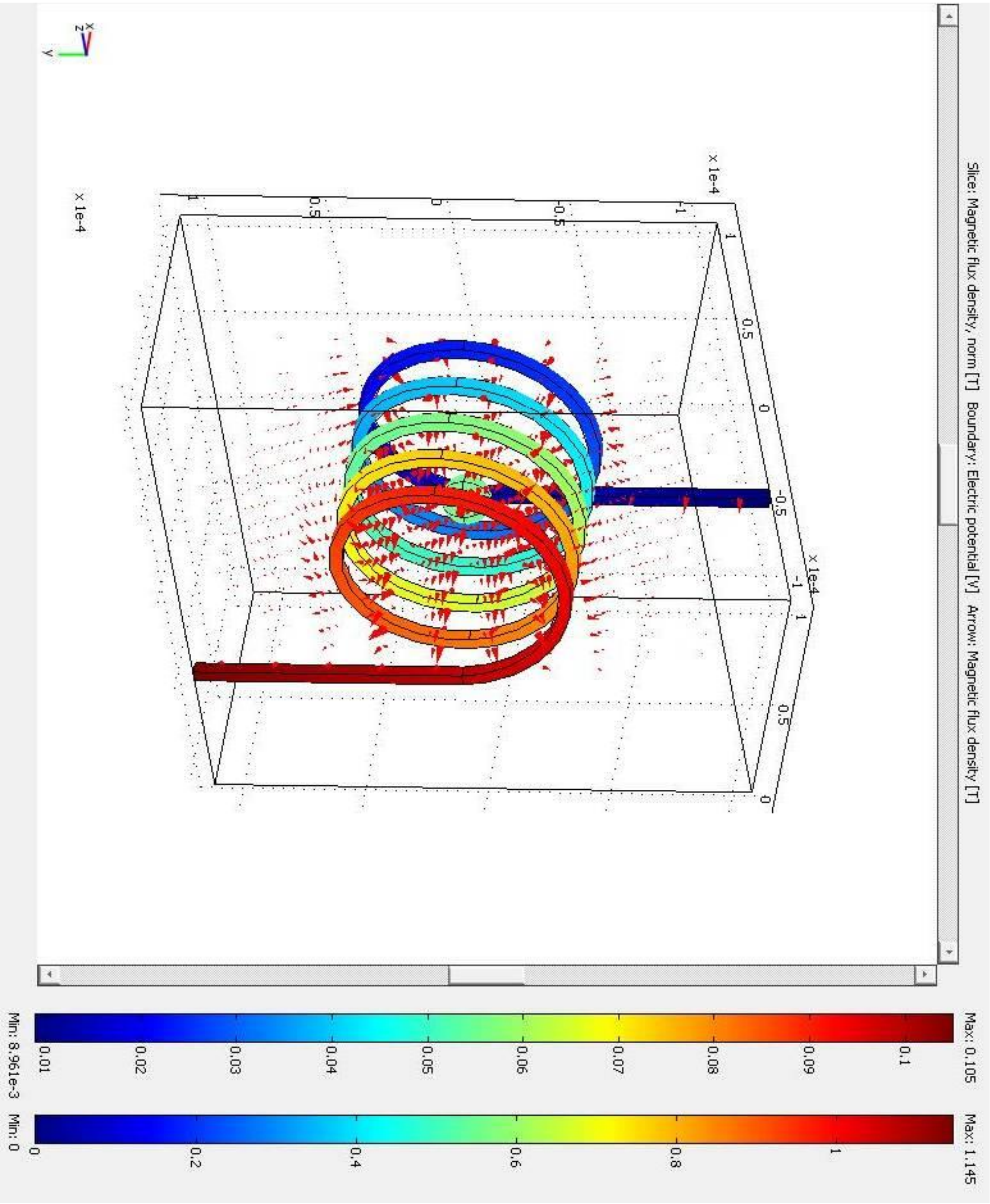

Figure C-18: Magnetic flux density and electric potential for Coil 9 with iron

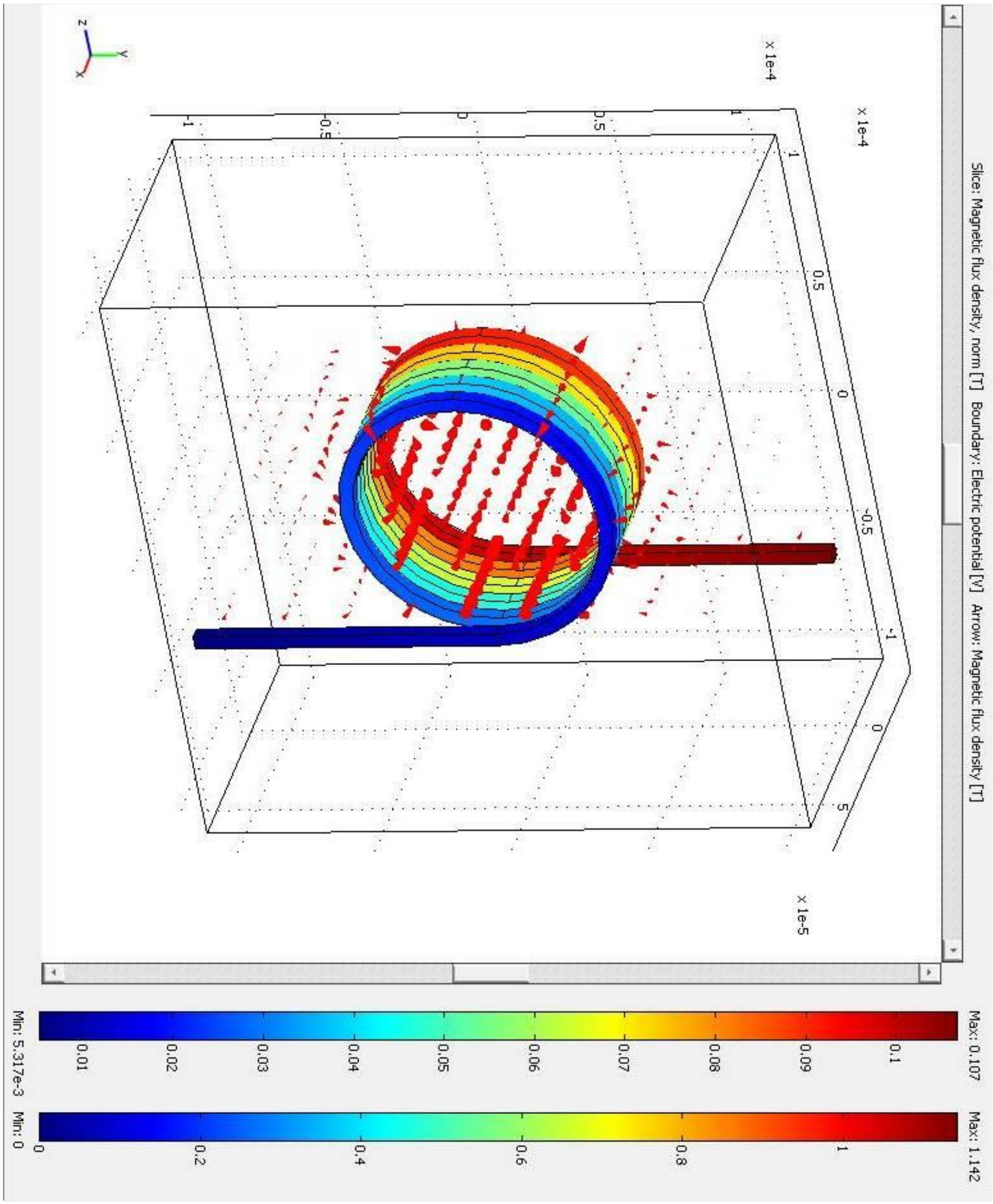

Figure C-19: Magnetic flux density and electric potential for Coil 10

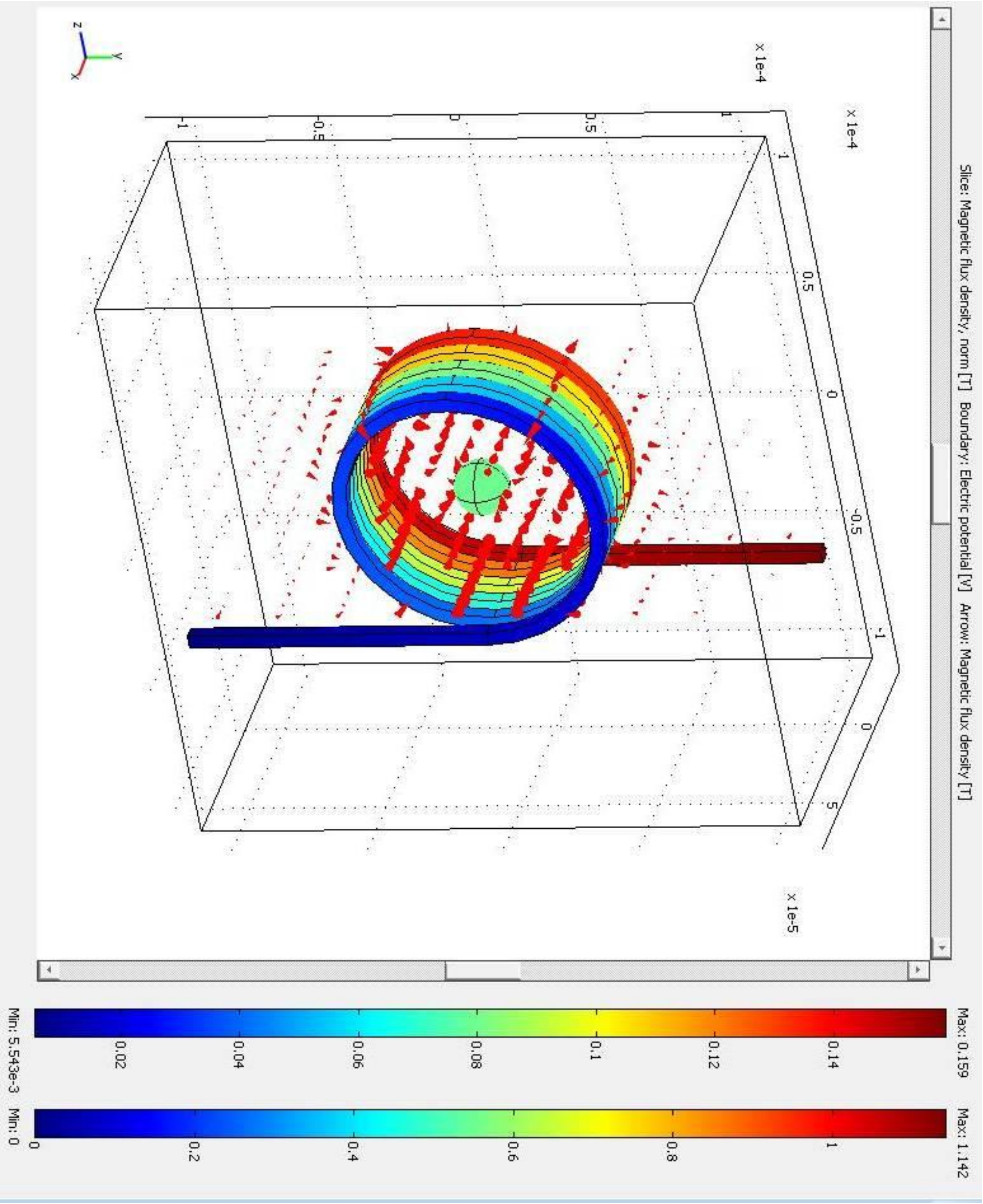

Figure C-20: Magnetic flux density and electric potential for Coil 10 with iron

REFERENCE LIST

[1] M. Lany, G. Boero and R.S. Popovic. July 2005. Superparamagnetic microbead inductive detector. Review of Scientific Instruments 76, 084301.

[2] F. Fixe, D.M.F. Prazeres, V. Chu, and J.P. Conde. Spring 2004. Optoelectronic detection of DNA molecules using an amorphous silicon photodetector. Mat. Res. Soc. Symp. Proc. Vol. 820.

[3] K. Giroux, “A pulsed resonance based measurement scheme for the detection of ferromagnetically tagged samples,” B.A.Sc. thesis, Simon Fraser University, Burnaby, BC, Canada, 2008.

[4] William Houghton, “Using LC oscillator circuits with Philips microcontrollers”, NXP, 1995 May 05. [Online]. Available : http://www.diakom.com.ru/el/elfirms/appnotes/Philips/an456.pdf [Accessed: November 23rd 2010]

[5] “Data Sheet 74HCU04 Hex Inverter,” Data Sheet Catalog, Philips Semiconductors, September 1993. [Online]. Available: http://www.datasheetcatalog.com/datasheets_pdf/7/4/H/C/74HCU04.shtml [Accessed: Mar. 19, 2009]

[6] N. Asuni, “Inductance Calculations: Circular Loop,” Technick, March 1998. [Online]. Available: http://www.technick.net/public/code/cp_dpage.php?aiocp_dp=util_inductance_circle [Accessed: Mar. 18, 2009]

[7] “Dielectric Constants Chart,” K-Tek Technical Information, K-Tek. [Online]. Available: http://www.asiinstr.com/technical.aspx [Accessed: Mar. 19, 2009]

[8] L. Matuszewski, A. Wall, T. Persigehl, B. Tombach, M. Fobker, C. Poremba, W. Heindel, and C. Bremer, “Cell labeling using superparamagnetic iron oxide particles: Impact of particle size, surface-coating and lipofection on labeling efficiency” [Online] 2004, Available: http://cds.ismrm.org/ismrm-2004/Files/001730.pdf [Accessed: November 23rd 2010]

[9] Q. A. Pankhurst, J. Connolly, S. K. Jones, and J. Dobson, “Applications of magnetic nano particles in biomedicine,” J. Phys. D: Appl. Phys. 36 (2003), R167–R181, Available: http://www.physics.gla.ac.uk/~dtngo/Article/JPD_36_2003_R167.pdf [Accessed: November 23rd 2010]

[10] Micro Chem, “Nano SU-8 2000, Negative Tone Photoresist Formulations 2002-2025," [Online], Avalable: http://www.microchem.com/products/pdf/SU8_2002-2025.pdf [Accessed: November 23rd 2010]

[11] R. C. Jaeger, *Introduction to Microelectronic Fabrication* (Volume V), 2nd ed. Upper Saddle River, NJ: Prentice Hall, 2002.